Search for the Decay $K_L^0 \to \pi^0 \nu \bar{\nu}$

A DISSERTATION

Department of Physics, Graduate School of Science
Kyoto University

BY

Toshi SUMIDA

June, 2008

Abstract

This thesis describes the results of a search for the decay $K_L^0 \to \pi^0 \nu \bar{\nu}$ performed by the E391a experiment at KEK 12 GeV Proton Synchrotron. We analyzed full data taken in the second run period in 2005. A blind analysis technique was employed, and we established the background level estimation before examining the candidate events in the signal region. No events were observed with the expected background of 0.42 ± 0.14, and we set an upper limit of 6.7×10^{-8} at the 90% confidence level, which represents the improvement by a factor of 3.1 over the past limit.

Acknowledgments

Contents

List of Figures

List of Tables

Chapter 1

Introduction

1.1 Symmetries

Symmetries and conservation laws are closely related in physics. For example, the conservation laws of the momentum and angular momentum are derived from the translational and rotational symmetries, respectively, in the Noether's theorem. In addition to these continuous symmetries, there are discrete symmetries that have played an important role in physics.

1.1.1 Parity (P)

The parity transformation changes the sign of all spatial coordinates with respect to a given origin at once. The laws of classical physics remain invariant under this operation. In quantum mechanics, the parity operator P is defined as hermitian and unitary, and its eigenvalues are ± 1. The fundamental particles have their own intrinsic parity. The intrinsic parity of a boson pair is $+1$, while the intrinsic parity of a fermion-antifermion pair is -1.

A collision or decay process conserves parity if the differential cross section of that process is equal to that of the space-inverted process. It was generally assumed that parity is a good symmetry of nature until 1956, when Lee and Yang suggested that parity might not be conserved in weak interactions [1]. Parity violation in the angular distribution of emitted electrons in the nuclear β decay of polarized Co^{60} was observed in the following year by C. S. Wu *et al.* [2].

1.1.2 Charge Conjugation (C)

The Charge Conjugation operation C changes particles to their antiparticles. The particles whose antiparticles are themselves are eigenstates of the C operator. The eigenvalues of C are ± 1 because after performing C twice, any state must come back to the original state. The photon has the C eigenvalue of -1 because the electromagnetic field A_μ changes sign when the sign of the charges is changed. The states with n photons have the C eigenvalue $(-1)^n$. The neutral pion, since it decays into two photons, has a C eigenvalue of $+1$.

C violation in pion decay was observed in the experiments by Garwin *et al.* [3] and Friedman, Telegdi [4] soon after the observation of parity violation in β decay.

1.1.3 CP Symmetry

In these experiments establishing P violation and C violation, the combined operation of C and P (CP) was conserved. Thus it was believed that CP should be a good symmetry in weak interactions until 1964, when Christenson, Cronin, Fitch, and Turlay [5] observed unambiguous CP violation in the decay of long-lived neutral kaons (K_L^0).

CP violation is very important in couple of reasons. One of these stems from the invariance of CPT: the combination of CP and time reversal conjugation(T). Under the minimal assumptions that nature is described by local quantum field theories that exhibit Lorentz invariance and obey the spin-statistics theorem, CPT must be a good symmetry for all interactions constructed in such theories. Thus, CP violation implies the T violation: there is an arrow of time governing the most microscopic physical reactions. CP violation also hinted at the existence of the third generation of quarks and leptons in the Standard Model [6]. CP violation is a key to the question of why there is more matter in the universe than antimatter. In the assumption that matter and antimatter were present in equal amounts in the early universe, one of the requirements for the observed matter dominance is that there should be CP violation [7].

1.2 Kaon Phenomenology

In order to understand the theoretical interests in the $K_L^0 \rightarrow \pi^0 \nu \bar{\nu}$ decay, it is necessary to know of the CP violation in neutral kaon system. Kaons are the mesons formed by the combination of a strange quark and a quark in the first generation. The neutral kaons, K^0 and $\overline{K^0}$ are the eigenstates of strangeness (S):

$$K^0 = \begin{pmatrix} d \\ \bar{s} \end{pmatrix} \quad (S = +1) \,,$$

$$\overline{K^0} = \begin{pmatrix} \bar{d} \\ s \end{pmatrix} \quad (S = -1) \,, \tag{1.1}$$

where S denotes the strangeness. They are produced through strong interactions, such as:

$$\pi^- + p \rightarrow K^0 + \Lambda \tag{1.2}$$

with conserving the strangeness.

However, they are not eigenstates of CP but are CP conjugate states to each other, as shown in Equation 1.1:

$$\text{CP} | K^0 \rangle = | \overline{K^0} \rangle \,,$$

$$\text{CP} | \overline{K^0} \rangle = | K^0 \rangle \,. \tag{1.3}$$

Although there is an ambiguity in the phase between these two states, we may choose the phase as above because the phase is physically unobservable. Since our interest is CP violation, it is necessary

for us to introduce CP eigenstates instead of K^0 and $\overline{K^0}$. Let us define the new states K_1 and K_2 as linear combinations of K^0 and $\overline{K^0}$.

$$
\begin{aligned}
|\,K_1\,\rangle &= \frac{1}{\sqrt{2}}(|\,K^0\,\rangle + |\,\overline{K^0}\,\rangle) \,, \\[2mm]
|\,K_2\,\rangle &= \frac{1}{\sqrt{2}}(|\,K^0\,\rangle - |\,\overline{K^0}\,\rangle) \,.
\end{aligned}
\tag{1.4}
$$

As shown in the equations below, K_1 and K_2 are the CP eigenstates,

$$
\begin{aligned}
\mathrm{CP}|\,K_1\,\rangle &= \frac{1}{\sqrt{2}}(|\,\overline{K^0}\,\rangle + |\,K^0\,\rangle) = |\,K_1\,\rangle \quad (CP = +1 : \text{even}) \,, \\[2mm]
\mathrm{CP}|\,K_2\,\rangle &= \frac{1}{\sqrt{2}}(|\,\overline{K^0}\,\rangle - |\,K^0\,\rangle) = -|\,K_2\,\rangle \quad (CP = -1 : \text{odd}) \,,
\end{aligned}
\tag{1.5}
$$

Since $\pi^+\pi^-$ and $\pi^0\pi^0$ are CP even states, and $\pi^0\pi^0\pi^0$ and $\pi^+\pi^-\pi^0$ are CP odd states, K_1 can decay to $\pi^+\pi^-$ and $\pi^0\pi^0$, and K_2 can decay to $\pi^0\pi^0\pi^0$ or $\pi^+\pi^-\pi^0$, assuming that the contribution from S-wave component is dominant, through CP-conserving weak interactions.

By considering the phase space of these decays,

$$
\begin{aligned}
K_1 \to \pi\pi \qquad & Q = m_K - 2m_\pi \sim 220 \text{ MeV} \,, \\[2mm]
K_2 \to \pi\pi\pi \qquad & Q = m_K - 3m_\pi \sim 80 \text{ MeV} \,.
\end{aligned}
\tag{1.6}
$$

It had been believed that the short-lived kaon should correspond to K_1 and the long-lived kaon to K_2, in which the difference in their lifetime arose from this difference in the amount of phase space to the final states, until when CP violation was observed in 1964.

In our current knowledge, there are two kinds of CP violations in the neutral kaon system: one is "indirect CP violation" and another is "direct CP violation". The next two subsections briefly describe these two phenomena. We will assume that the CPT symmetry is conserved in the following discussions.

1.2.1   Indirect CP Violation

In 1964, CP violation was first observed in the decay of long lived neutral kaons into the final states of $\pi^+\pi^-$ and $\pi^0\pi^0$. The long-lived neutral kaon K_L^0 and short-lived kaon K_S^0 were interpreted as
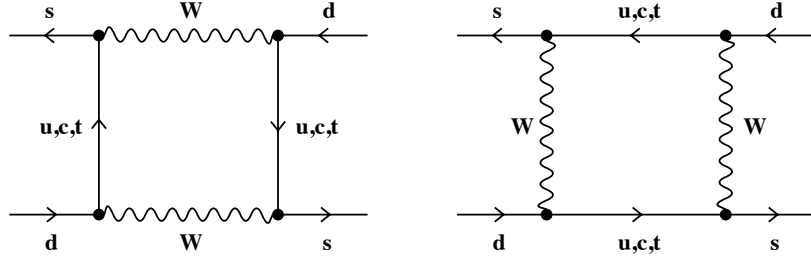
Figure 1.1: Box diagrams of the $K^0 - \overline{K^0}$ mixing.

superpositions of the K_1 and K_2,

$$
|K_L^0\rangle = \frac{1}{\sqrt{1 + |\epsilon|^2}}(|K_2\rangle + \epsilon|K_1\rangle)
$$

$$
= \frac{1}{\sqrt{2(1 + |\epsilon|^2)}}((1 + \epsilon)|K^0\rangle - (1 - \epsilon)|\overline{K^0}\rangle) , \tag{1.7}
$$

$$
|K_S^0\rangle = \frac{1}{\sqrt{1 + |\epsilon|^2}}(|K_1\rangle + \epsilon|K_2\rangle)
$$

$$
= \frac{1}{\sqrt{2(1 + |\epsilon|^2)}}((1 + \epsilon)|K^0\rangle + (1 - \epsilon)|\overline{K^0}\rangle) , \tag{1.8}
$$

where ϵ is the parameter to determine the size of $K_1(K_2)$ contamination to $K_L^0(K_S^0)$. They imply that the $K^0 - \overline{K^0}$ mixing (Figure 1.1) is asymmetric by $|\epsilon|$; the K_1 component in the K_L^0 decays into the two-pion final state. Thus, the small contamination of K_1 causes the CP violation and decay amplitude does not contribute to the CP violation.

We now evaluate the magnitude of the mixing parameter $|\epsilon|$ by using the semi-leptonic decays $K^0 \to \pi^- l^+ \nu_l$ and $\overline{K^0} \to \pi^+ l^- \bar{\nu}_l$ $(l = e, \mu)$. Based on Equation 1.7, the amplitude $K_L^0 \to \pi^\mp l^\pm \nu$ is proportional to $|1 \pm \epsilon|^2$. Thus, the ϵ is obtained from the decay asymmetry δ in semi-leptonic decays of K_L^0 defined as

$$
\delta = \frac{\Gamma(K_L^0 \to \pi^- l^+ \nu_l) - \Gamma(K_L^0 \to \pi^+ l^- \bar{\nu}_l)}{\Gamma(K_L^0 \to \pi^- l^+ \nu_l) + \Gamma(K_L^0 \to \pi^+ l^- \bar{\nu}_l)} . \tag{1.9}
$$

Substituting Equation 1.7 into Equation 1.9 yields

$$
\delta \approx 2\mathrm{Re}(\epsilon) . \tag{1.10}
$$

The world average of the measurements for the charge asymmetry is [8],

$$
\delta = 0.332 \pm 0.006\% . \tag{1.11}
$$
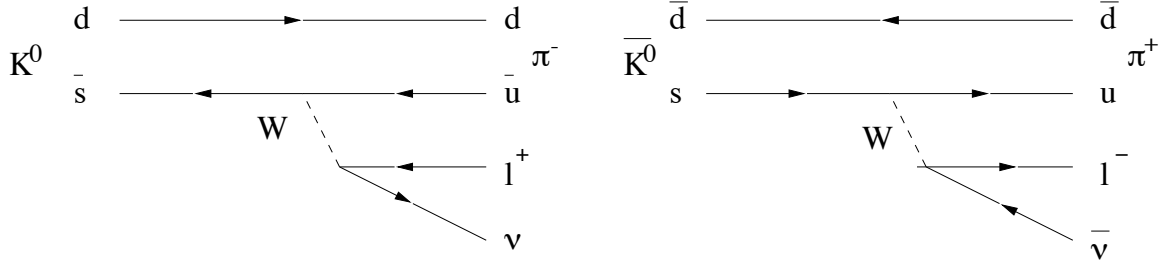
Figure 1.2: Feynman diagrams of semi-leptonic decays in neutral kaons, where $l = (e, \mu)$.

1.2.2 The Origin of the ϵ

We write the time evolution of $K^0 - \overline{K^0}$ mixing as:

$$i\frac{d\psi(t)}{dt} = \mathcal{H}\psi(t), \quad \psi(t) = \begin{pmatrix} |\,K^0(t)\,\rangle \\ |\,\overline{K^0}(t)\,\rangle \end{pmatrix}. \tag{1.12}$$

We can write $\mathcal{H}$ as the combination of two Hermitian matrices, M and Γ,

$$\mathcal{H} = M - i\frac{\Gamma}{2} = \begin{pmatrix} M_{11} - \frac{i}{2}\Gamma_{11} & M_{12} - \frac{i}{2}\Gamma_{12} \\ M_{21} - \frac{i}{2}\Gamma_{21} & M_{22} - \frac{i}{2}\Gamma_{22} \end{pmatrix}, \tag{1.13}$$

Invoking the hermiticity ($M_{21} = M_{12}^*$) and the CPT invariance ($M_{11} = M_{22} = M$, $\Gamma_{11} = \Gamma_{22} = \Gamma$), Equation 1.13 is simplified as

$$\mathcal{H} = \begin{pmatrix} M - \frac{i}{2}\Gamma & M_{12} - \frac{i}{2}\Gamma_{12} \\ M_{12}^* - \frac{i}{2}\Gamma_{12}^* & M - \frac{i}{2}\Gamma \end{pmatrix}. \tag{1.14}$$

In order to see the origin of non-zero value of ϵ, and thus the asymmetric $K^0 - \overline{K^0}$ mixing, we consider the mass eigenstates K_L^0 and K_S^0. Diagonalizing Equation 1.12 with definite masses $m_{L,S}$ and lifetimes $\tau_{L,S}$ (L and S represent the long- and short-lived neutral kaons, respectively), we obtain

$$\mathcal{H}|\,K_{L,S}\,\rangle = (m_{L,S} - \frac{i}{2}\Gamma_{L,S})\,|\,K_{L,S}\,\rangle . \tag{1.15}$$

Substituting Equation 1.7, 1.8 and 1.14 into 1.15, ϵ is obtained as

$$\epsilon = \frac{\text{Im}(M_{12}) - \frac{i}{2}\text{Im}(\Gamma)}{i\Delta m - \frac{1}{2}(\Gamma_S - \Gamma_L)} , \tag{1.16}$$

where Δm is the mass difference between the long and short lived kaons:

$$\Delta m = m_L - m_S . \tag{1.17}$$

Equation 1.16 implies that both the mass matrix and the decay matrix contribute to the mixing of K^0 and $\overline{K^0}$, leading to the indirect CP violation. Then, the phase of ϵ is given as

$$\phi_\epsilon = \tan^{-1}\left(\frac{2\Delta m}{\Gamma_S - \Gamma_L}\right) , \tag{1.18}$$

neglecting $\text{Im}(\Gamma_{12})$ by using an experimental fact that $\text{Im}(M_{12}) \gg \text{Im}(\Gamma_{12})$.

With the world averages of $\Delta m (= 0.5292 \pm 0.0009 \times 10^{10} \hbar s^{-1})$ and the lifetimes ($\tau_S = (0.8958 \pm 0.0006) \times 10^{-10}$sec, $\tau_L = (5.114 \pm 0.021) \times 10^{-8}$sec) [8], we obtain

$$\phi_\epsilon = 43.51^\circ \pm 0.05^\circ \ , \tag{1.19}$$

The current world average [8] is

$$|\epsilon| \ = \ (2.232 \pm 0.007) \times 10^{-3} \ . \tag{1.20}$$

1.2.3   Direct CP Violation

It is interesting to consider the ratio of the decay amplitude $K_L^0 \to f$ to that of $K_S^0 \to f$, where f is a CP even eigenstate:

$$r_f = \frac{\langle f |\mathcal{H}| K_L^0 \rangle}{\langle f |\mathcal{H}| K_S^0 \rangle} \ . \tag{1.21}$$

r_f is a measure of CP violating effects because it shows the ratio of CP violating to CP conserving amplitudes. With the amplitudes

$$a_f = \langle f |\mathcal{H}| K^0 \rangle \ ,$$

$$\bar{a}_f = \langle f |\mathcal{H}| \overline{K^0} \rangle \ , \tag{1.22}$$

including final state interactions. Substituting Equations 1.7 and 1.8, Equation 1.21 yields

$$r_f = \frac{(a_f - \bar{a}_f) + \epsilon(a_f + \bar{a}_f)}{\epsilon(a_f - \bar{a}_f) + (a_f + \bar{a}_f)} \ . \tag{1.23}$$

If a_f and $\bar{a}_f$ are not equal, Equation 1.23 shows that the decay matrix does not only affect $K^0 - \overline{K^0}$ mixing through ϵ but also directly contributes to a CP violation through the term of $a_f - \bar{a}_f$. If we define the decay asymmetry

$$\chi_{\pi^+\pi^-} \equiv \frac{a_{\pi^+\pi^-} - \bar{a}_{\pi^+\pi^-}}{a_{\pi^+\pi^-} + \bar{a}_{\pi^+\pi^-}} \tag{1.24}$$

in the CP violating decay $K_L^0 \to \pi^+\pi^-$, we obtain

$$r_{\pi^+\pi^-} = \frac{\epsilon + \chi_{\pi^+\pi^-}}{1 + \epsilon\chi_{\pi^+\pi^-}} \approx \epsilon + \chi_{\pi^+\pi^-} \tag{1.25}$$

by using the fact that the ϵ is of order 10^{-3}. The term $\chi_{\pi^+\pi^-}$ represents an additional contribution to CP violation besides mixing due to ϵ. This is called "direct CP violation".

In order to discuss CP violation in $\pi\pi$ decays, we redefine $r_{\pi^+\pi^-}$ in a traditional notation as

$$\eta_{+-} \equiv \frac{\langle \pi^+\pi^- |\mathcal{H}| K_L^0 \rangle}{\langle \pi^+\pi^- |\mathcal{H}| K_S^0 \rangle} = r_{\pi^+\pi^-} \ , \tag{1.26}$$

and define a similar quantity for the neutral decay mode as

$$\eta_{00} \equiv \frac{\langle \pi^0\pi^0 |\mathcal{H}| K_L^0 \rangle}{\langle \pi^0\pi^0 |\mathcal{H}| K_S^0 \rangle} = r_{\pi^0\pi^0} \ . \tag{1.27}$$

Since there are strong final state interactions in $\pi\pi$ decays, we formulate the final state in terms of the strong eigenstate, i.e. the isospin eigenstate:

$$\langle\, I\, |\mathcal{H}|\, K^0\,\rangle = a_I \equiv A_I e^{i\delta_I}\ , \tag{1.28}$$

where the isospin of $\pi\pi$ is either 0 or 2 due to the Bose symmetry of π's and δ_I is the phase shift induced by final state strong interactions. The assumption of CPT invariance leads to

$$\langle\, I\, |\mathcal{H}|\, \overline{K^0}\,\rangle = \bar{a}_I \equiv A_I^* e^{i\delta_I}\ . \tag{1.29}$$

The $\pi^+\pi^-$ eigenstate is a superposition of the $I = 0$ and $I = 2$ components as

$$|\,\pi^+\pi^-\,\rangle = \sqrt{\frac{2}{3}}|\, I = 0\,\rangle + \sqrt{\frac{1}{3}}|\, I = 2\,\rangle\ , \tag{1.30}$$

using Clebsh-Gordan coefficients. Substituting this expression and Equation 1.28 into 1.24, we obtain

$$\chi_{\pi^+\pi^-} = \frac{i\mathrm{Im}(A_2)e^{i(\delta_2-\delta_0)}}{\sqrt{2}A_0 + \mathrm{Re}(A_2)e^{i(\delta_2-\delta_0)}}$$

$$= \frac{\epsilon'}{1 + \omega/\sqrt{2}} \tag{1.31}$$

where we define the parameters ϵ' and ω as

$$\epsilon' \equiv \frac{i}{\sqrt{2}}e^{i(\delta_2-\delta_0)}\frac{\mathrm{Im}(A_2)}{A_0}\ , \tag{1.32}$$

$$\omega \equiv \frac{\mathrm{Re}(A_2)}{A_0}e^{i(\delta_2-\delta_0)}\ , \tag{1.33}$$

with the Wu-Yang phase convention [9] taking A_0 to be real with an appropriate phase.

The parameter ω represents the ratio of the CP conserving $\Delta I = 3/2$ amplitude to CP conserving $\Delta I = 1/2$ amplitude in $K_S^0 \to \pi\pi$ decay. $\Delta I = 3/2$ transitions are suppressed [10] as $\omega \sim 1/22$ in the experiments. Since ω is small, we see that ϵ' is the scale of direct CP violation in Equation 1.31. Substituting Equation 1.31 into 1.25, we obtain

$$\eta_{+-} \approx \epsilon + \epsilon'\ . \tag{1.34}$$

A similar calculation for neutral mode gives

$$\eta_{00} \approx \epsilon - 2\epsilon'\ . \tag{1.35}$$

In order to measure these quantities, it is necessary to measure a double ratio of four decay rates. The signature of direct CP violation is expressed as

$$\frac{\Gamma(K_L^0 \to \pi^+\pi^-)/\Gamma(K_S^0 \to \pi^+\pi^-)}{\Gamma(K_L^0 \to \pi^0\pi^0)/\Gamma(K_S^0 \to \pi^0\pi^0)} \approx \left|\frac{\eta_{+-}}{\eta_{00}}\right|^2 \approx \left|\frac{\epsilon+\epsilon'}{\epsilon-2\epsilon'}\right|^2 \approx 1 + 6\mathrm{Re}(\epsilon'/\epsilon)\ . \tag{1.36}$$

Non-zero value of $\mathrm{Re}(\epsilon'/\epsilon)$ indicates the existence of direct CP violation. The world average listed in the PDG [8] is

$$\mathrm{Re}(\epsilon'/\epsilon) = (1.66 \pm 0.26) \times 10^{-3}\ . \tag{1.37}$$

1.3   The Standard Model and CP Violation

The Standard Model (SM) of particle physics is defined by three generations of quarks and leptons with interactions defined by the gauge group $SU(3)_C \otimes SU(2)_L \otimes U(1)$. The Left-handed quarks and leptons are put into $SU(2)_L$ doublets in the electroweak interaction:

$$\begin{pmatrix} u \\ d \end{pmatrix} \quad \begin{pmatrix} c \\ s \end{pmatrix} \quad \begin{pmatrix} t \\ b \end{pmatrix}$$

$$\begin{pmatrix} \nu_e \\ e^- \end{pmatrix} \quad \begin{pmatrix} \nu_\mu \\ \mu^- \end{pmatrix} \quad \begin{pmatrix} \nu_\tau \\ \tau^- \end{pmatrix} \tag{1.38}$$

The Lagrangian of the charged current in the weak interaction is given by:

$$\mathcal{L}_{CC} = \frac{g}{\sqrt{2}} \left[\bar{u}_i V_{ij} d_j W^- + \bar{d}_j V_{ij}^* u_i W^+ \right] \tag{1.39}$$

where $u_i = (u, c, t)$ are left-handed up-type quarks and $d_i = (d, s, b)$ are left-handed down-type quarks, and $W^\pm$ denote the weak bosons. V_{ij} is the 3×3 unitary Cabibbo-Kobayashi-Maskawa (CKM) matrix which connects the up-type quarks with the down-type quarks:

$$V = \begin{pmatrix} V_{ud} & V_{us} & V_{ub} \\ V_{cd} & V_{cs} & V_{cb} \\ V_{td} & V_{ts} & V_{tb} \end{pmatrix} . \tag{1.40}$$

The Lagrangian transforms under CP as

$$\mathcal{L}_{CC} \xrightarrow[\text{CP}]{} \frac{g}{\sqrt{2}} \left[\bar{d}_j V_{ij} u_i W^+ + \bar{u}_i V_{ij}^* d_j W^- \right] \tag{1.41}$$

Thus, if $V_{ij} = V_{ij}^*$, CP is conserved. Complex components in the matrix would necessarily violate CP invariance.

1.3.1   The CKM Matrix

An $n \times n$ complex matrix has $2n^2$ free real parameters. When the matrix is unitary, there are n^2 constraints. Relative phases of $(2n - 1)$ quarks can be included to a wave function of the quarks. Thus, we have

$$2n^2 - n^2 - (2n - 1) = (n - 1)^2 \tag{1.42}$$

free parameters in the mixing matrix. Since the number of independent planes of rotation in n dimensional phase space is $_n C_2 = \frac{n(n-1)}{2}$, the remaining

$$(n - 1)^2 - \frac{n(n - 1)}{2} = \frac{(n - 1)(n - 2)}{2} \tag{1.43}$$

is the number of complex phases. To summarize:

$$\text{number of rotation: } n_\theta = \frac{1}{2} n(n - 1) \ ,$$

$$\text{number of phase } \ : n_\delta = \frac{1}{2}(n - 1)(n - 2) \ . \tag{1.44}$$

When $n = 2$, we have only one rotation angle ($n_\theta = 1, n_\delta = 0$). In the case of $n = 3$, we have three rotation angles and one phase ($n_\theta = 3, n_\delta = 1$).

The CKM matrix was introduced by Kobayashi and Maskawa [6] in 1973, extending the concept of flavor mixing originally introduced by Cabibbo [11] to the three generations of quarks. As the discussion above, the CKM matrix V has three angles $\theta_{12}, \theta_{23}, \theta_{13}$ and one phase δ. One way of parameterization is

$$
V = \begin{pmatrix}
c_{12}c_{13} & s_{12}c_{13} & s_{13}e^{i\delta} \\
-s_{12}c_{23} - c_{12}s_{23}s_{13}e^{i\delta} & c_{12}c_{23} - s_{12}s_{23}s_{13}e^{i\delta} & s_{23}c_{13} \\
s_{12}c_{23} - c_{12}s_{23}s_{13}e^{i\delta} & -c_{12}c_{23} - s_{12}s_{23}s_{13}e^{i\delta} & c_{23}c_{13}
\end{pmatrix} . \tag{1.45}
$$

where $c_{ij} = \cos\theta_{ij}$ and $s_{ij} = \sin\theta_{ij}$.

Wolfenstein [12] parameterized the CKM matrix through an expansion in powers of $\lambda = |V_{us}| \sim 0.22$:

$$
V = \begin{pmatrix}
1 - \frac{\lambda^2}{2} & \lambda & A\lambda^3(\rho - i\eta) \\
-\lambda & 1 - \frac{\lambda^2}{2} & A\lambda^2 \\
A\lambda^3(1 - \rho - i\eta) & -A\lambda^2 & 1
\end{pmatrix} + \mathcal{O}(\lambda^4) , \tag{1.46}
$$

where η is the CP violation parameter. In this parameterization, V is CP invariant to the order of λ^2, and CP violation shows up first in the order of λ^3. Numerical values of each parameter is determined by experiments as discussed in the later subsection.

1.3.2 The Unitary Triangle

All the CP violating observables are proportional to a quantity called Jarlskog invariant J [13], which is independent of the choice of parameterization in the CKM matrix:

$$
J = \text{Im}[V_{ij}V_{lk}V_{ik}^*V_{lj}^*] \quad (i \neq l,\ j \neq k) \tag{1.47}
$$

where l and k denote up-type and down-type quarks, respectively. In terms of the explicit parameterizations given above, J becomes

$$
J = c_{12}c_{23}c_{13}^2 s_{12}s_{23}s_{13}\sin\delta \simeq \lambda^6 A^2 \eta . \tag{1.48}
$$

Imposing the unitarity condition to the first and third columns in the CKM matrix, we obtain

$$
V_{ub}^*V_{ud} + V_{cb}^*V_{cd} + V_{tb}^*V_{td} = 0 . \tag{1.49}
$$

This relation can be expressed as a triangle in the complex plane, which is called the unitarity triangle (Figure 1.3). We can take $V_{ud} \approx 1$ to the first order in λ, and the unitarity condition becomes

$$
V_{ub}^* + V_{td} = A\lambda^3 . \tag{1.50}
$$

The area of the triangle is proportional to the measure of CP violation, J.

An amplitude of the imaginary parameter η, is the essence of CP violation in the Standard Model. In Equations 1.45, 1.46, such amplitudes are introduced with the $|V_{td}|$ or $|V_{ub}|$ component in the diagrams of CP violating processes.
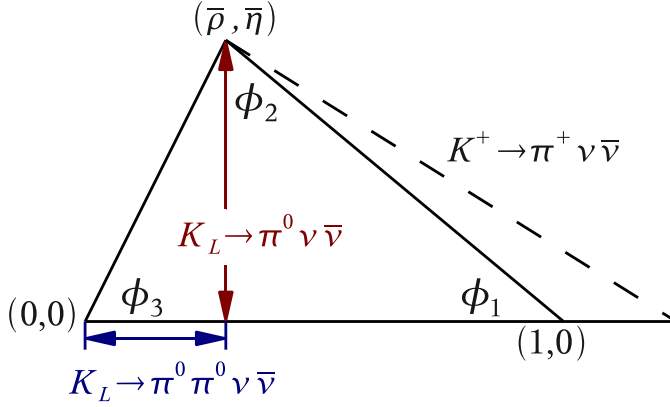
Figure 1.3: Unitarity triangle with the impacts of $K \to \pi(\pi)\nu\bar{\nu}$ on the parameters visualized.

1.3.3 Current Status of CKM Parameters

As shown in Equation 1.48, A, λ and η determine the size of CP violation in the Standard Model. They are also used in theoretical calculations to predict the branching ratio of $K_L^0 \to \pi^0\nu\bar{\nu}$ decay, as will be discussed in the next section. In this subsection, we briefly summarize the current status of constraints on the CKM parameters, which are from a combination of various experiments.

The parameter $\lambda = |V_{us}|$ is determined by the decay rates of strange particles. The current average value is reported to be $|V_{us}| = 0.2257 \pm 0.0021$ [8]. The parameter A can be determined with λ and the measurement of $|V_{cb}|$ as shown in Equation 1.40 and 1.46. $|V_{cb}|$ is obtained from the semi-leptonic decays in B mesons to be $|V_{cb}| = (41.6 \pm 0.6) \times 10^{-3}$ [8].

The constraints on the $(\bar{\rho}, \bar{\eta})$ plane, where $\bar{\rho} = \rho(1 - \lambda^2/2)$ and $\bar{\eta} = \eta(1 - \lambda^2/2)$, respectively, are imposed from several measurements. A detailed description can be found in the reference [8]. $|\epsilon|$ and $\sin 2\phi_1$ are typical parameters in the K and B meson systems, respectively.

$|\epsilon|$ is connected to $(\bar{\rho}, \bar{\eta})$ through the relation [14]:

$$\epsilon = \bar{\eta}A^2 B_K \left[1.248(1 - \bar{\rho})A^2 \left(\frac{m_t}{170(\text{GeV})} \right)^{1.52} + 0.31 \right] , \qquad (1.51)$$

where B_K is the kaon bag parameter estimated to be 0.85 ± 0.15 [15], and m_t is the mass of the top quark.

The decay process of $b \to c\bar{c}s$ gives, in the time-dependent CP violation, an important parameter $\sin 2\phi_1$, where ϕ_1 is an angle of the unitary triangle in the $(\bar{\rho}, \bar{\eta})$ plane as shown in Figure 1.3. An average of the present experimental results from the BELLE and the BaBar experiments is to be [8]:

$$\sin 2\phi_1 = 0.687 \pm 0.032 . \qquad (1.52)$$

All the constraints on $(\bar{\rho}, \bar{\eta})$ are well consistent with one region as shown in Figure 1.4. The measurement in the K meson system, $|\epsilon|$, and the measurement in the B meson system, $\sin 2\phi_1$, well agree to each other. The Wolfenstein parameters [8] due to the fitting of these measurements are:

$$\lambda = 0.2272 \pm 0.0010 , \quad A = 0.818^{+0.007}_{-0.017} , \qquad (1.53)$$

$$\bar{\rho} = 0.221^{+0.064}_{-0.028} , \quad \bar{\eta} = 0.340^{+0.017}_{-0.045} . \qquad (1.54)$$
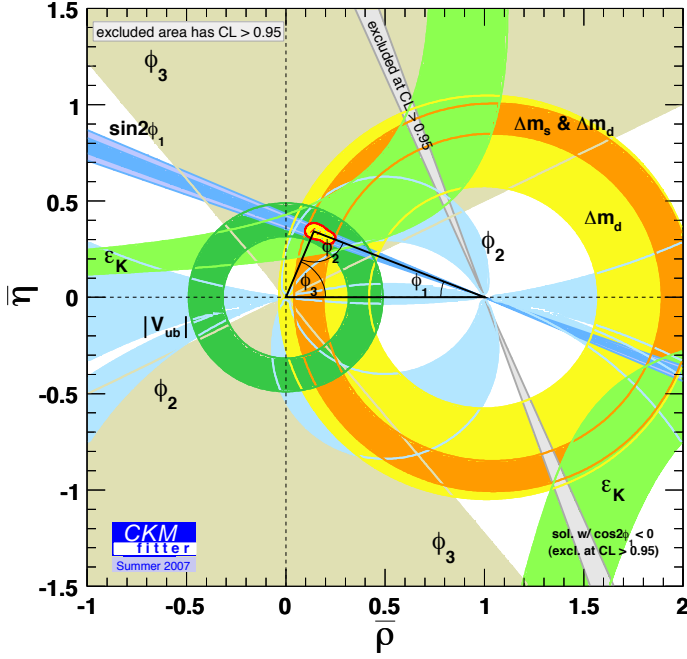
Figure 1.4: Constraints on the $(\bar{\rho}, \bar{\eta})$ plane with recent experimental measurements [16]. $|\epsilon|$ is denoted as ε_K in this figure.

1.4 $K_L^0 \to \pi^0 \nu \bar{\nu}$ Decay in the Standard Model

The role of the $K_L^0 \to \pi^0 \nu \bar{\nu}$ decay in the Standard Model is that it can determine the parameter η precisely. In this section, we describe theoretical importance of the $K_L^0 \to \pi^0 \nu \bar{\nu}$ decay and interpretation of the $K_L^0 \to \pi^0 \nu \bar{\nu}$ decay as a probe to study the CP violation in the Standard Model.

Since the magnitude of ϵ, which implies the indirect CP violation, is small, the amplitude of the $K_L^0 \to \pi^0 \nu \bar{\nu}$ decay is

$$A(K_L^0 \to \pi^0 \nu \bar{\nu}) \simeq A(K_2 \to \pi^0 \nu \bar{\nu}) . \tag{1.55}$$

The $K_L^0 \to \pi^0 \nu \bar{\nu}$ decay is dominated by the short-distance process and are mediated by the second-order diagrams of the electroweak interactions as shown in Figure 1.5. Since K_2 is a superposition of K^0 and $\overline{K^0}$, and a top quark dominates in the intermediate state, the amplitude of K_2 is expressed as:

$$A(K_2 \to \pi^0 \nu \bar{\nu}) = \frac{1}{\sqrt{2}} \left(A(K^0 \to \pi^0 \nu \bar{\nu}) - A(\overline{K^0} \to \pi^0 \nu \bar{\nu}) \right)$$

$$\propto V_{td}^* V_{ts} - V_{ts}^* V_{td} \propto 2i\eta . \tag{1.56}$$

Thus, the branching ratio of the $K_L^0 \to \pi^0 \nu \bar{\nu}$ decay, $Br(K_L^0 \to \pi^0 \nu \bar{\nu})$, is proportional to η^2. CP is not conserved before and after the interaction because of the CP violation phase in the amplitude.
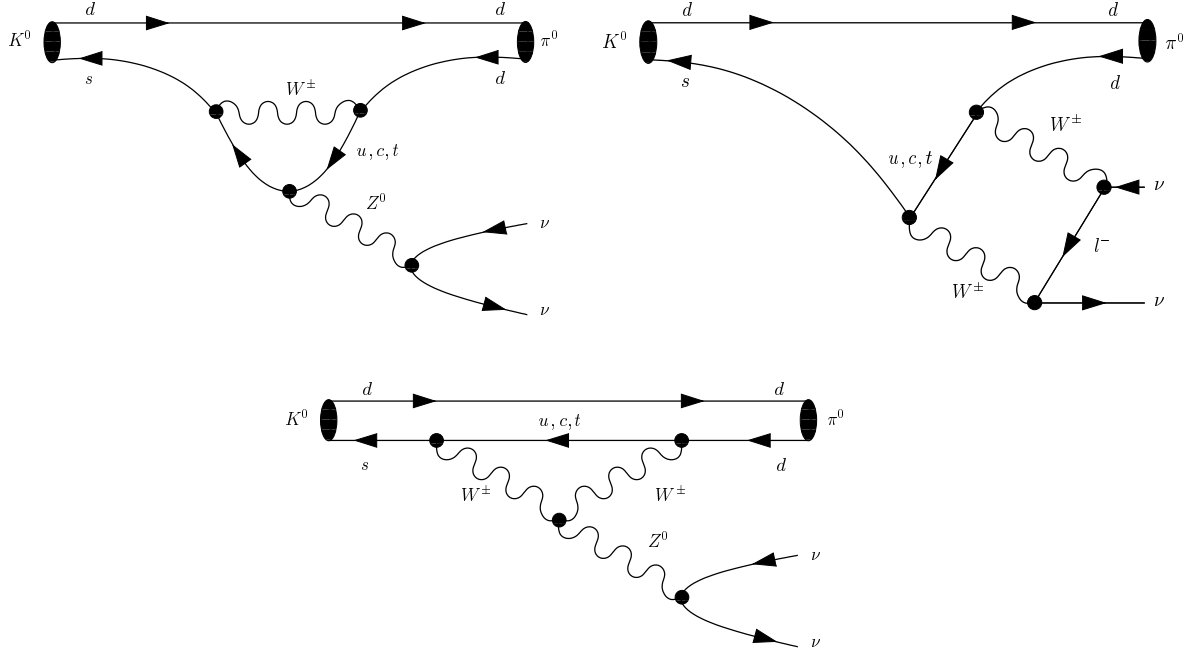
Figure 1.5: Penguin and box Feynman diagrams for the $K_L^0 \to \pi^0 \nu \bar{\nu}$ decay. The decay is dominated by the top quark contribution. Figure quoted from [17]

$Br(K_L^0 \to \pi^0 \nu \bar{\nu})$ is represented in the Standard Model as [17]:

$$Br(K_L^0 \to \pi^0 \nu \bar{\nu}) = \kappa_L \cdot \left(\frac{\text{Im}(\lambda_t)}{\lambda^5} X(x_t) \right)^2 , \tag{1.57}$$

$$\kappa_L = (2.231 \pm 0.013) \cdot 10^{-10} \left[\frac{\lambda}{0.225} \right]^8 ,$$

where x_t is the square of the ratio of the top to the W masses, $x_t = m_t^2 / m_W^2$, and $X(x_t)$ is the Inami-Lim loop function [18] with QCD higher order corrections, respectively. Given η, $Br(K_L^0 \to \pi^0 \nu \bar{\nu})$ can be computed to an exceptionally high degree of precision that is not matched by any other decays of mesons. The reasons are: (1) long-distance contributions are negligible and (2) the hadronic matrix elements are extracted directly from measured $Br(K^+ \to \pi^0 e^+ \nu)$. The theoretical uncertainty in $Br(K_L^0 \to \pi^0 \nu \bar{\nu})$ is only $1 - 2$ % [17].

Using the inputs of the CKM parameters, the $Br(K_L^0 \to \pi^0 \nu \bar{\nu})$ is predicted in the Standard Model [19] to be

$$Br(K_L^0 \to \pi^0 \nu \bar{\nu}) = (2.49 \pm 0.39) \times 10^{-11}, \tag{1.58}$$

where the error is dominated by the uncertainties in the CKM parameters.

Because of the theoretical cleanness, measurement of the $K_L^0 \to \pi^0 \nu \bar{\nu}$ branching ratio can be directly translated into the information on the magnitude of the CP violation in the Standard Model.

Assuming that the branching ratio is measured within ± 5 %, we can determine the CP violation phase η within ± 3 %. On the other hand, one of the CP asymmetry measurement in the B meson system, $B \to J/\psi K_S^0$, determines the CP violation phase in the Standard Model with a small theoretical uncertainty. The magnitude of the CP violation determined by both measurements should be identical in the Standard Model.

$$\text{(size of CPV)}_{\pi\nu\nu} = \text{(size of CPV)}_{J/\psi K_S^0} \tag{1.59}$$

This relation is not only a very powerful tool to check the Standard Model, but also useful to discriminate among different new physics models, which will be described in the next.

1.5 Beyond the Standard Model

In this section, we describe the role of the $K_L^0 \to \pi^0 \nu\bar{\nu}$ decay beyond the Standard Model (BSM), in particular, concerning possible new sources of CP violation. We describe a model-independent limit on $Br(K_L^0 \to \pi^0 \nu\bar{\nu})$, so-called the Grossman-Nir limit, and an overview of the $K_L^0 \to \pi^0 \nu\bar{\nu}$ decay in the physics beyond the Standard Model.

1.5.1 Grossman-Nir limit

Y. Grossman and Y. Nir pointed out a model-independent relation between $K^+ \to \pi^+ \nu\bar{\nu}$ and $K_L^0 \to \pi^0 \nu\bar{\nu}$ [20] in 1997:

$$r_{is} \times \frac{\Gamma(K_L^0 \to \pi^0 \nu\bar{\nu})}{\Gamma(K^+ \to \pi^+ \nu\bar{\nu})} = \sin^2\theta , \tag{1.60}$$

where r_{is} is an isospin-breaking factor to

$$\frac{A(K^0 \to \pi^0 \nu\bar{\nu})}{A(K^+ \to \pi^+ \nu\bar{\nu})} = \frac{1}{\sqrt{2}} , \tag{1.61}$$

used in deriving the relation, and θ is the the relative CP-violating phase between the $K^0 - \overline{K^0}$ mixing amplitude and the $s \to d\nu\bar{\nu}$ decay amplitude. Using $r_{is} = 0.954$ [21], the lifetime ratio $\tau_{K_L^0}/\tau_{K^+} = 4.17$, and $\sin^2\theta \leq 1$, we have an upper limit to the ratio of two branching fractions as:

$$\frac{Br(K_L^0 \to \pi^0 \nu\bar{\nu})}{Br(K^+ \to \pi^+ \nu\bar{\nu})} < \frac{\tau_{K_L^0}}{\tau_{K^+}} \times \frac{1}{r_{is}} \simeq 4.4 . \tag{1.62}$$

A recent update [19], including the isospin-breaking factor at higher order in the chiral expansion and QED radiative corrections, improved the limit of 4.4 in Equation 1.62 to 4.3.

The AGS E787 and E949 collaboration at Brookhaven National Laboratory observed 3 $K^+ \to \pi^+ \nu\bar{\nu}$ candidates so far [22]. The measured branching ratio of $K^+ \to \pi^+ \nu\bar{\nu}$ is

$$Br(K^+ \to \pi^+ \nu\bar{\nu}) = \left[1.47^{+1.30}_{-0.89}\right] \times 10^{-10} , \tag{1.63}$$

and $Br(K^+ \to \pi^+ \nu\bar{\nu}) < 3.2 \times 10^{-10}$ at the 90 % confidence level. Thus,

$$Br(K_L^0 \to \pi^0 \nu\bar{\nu}) < 1.4 \times 10^{-9} \quad (90 \text{ % C.L.}) . \tag{1.64}$$

This upper bound is valid in any extensions of the Standard Model.
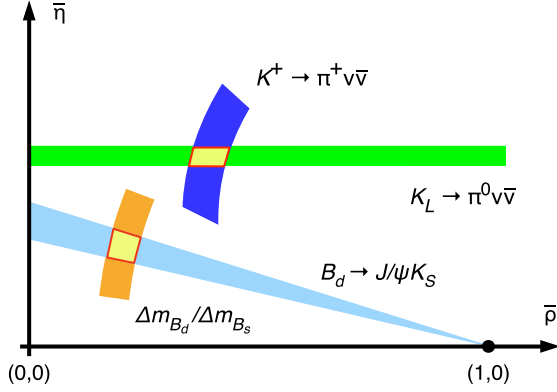
Figure 1.6: Schematic determination of (ρ, η) from the B system ($B_d \rightarrow J/\psi K_S^0$ and $\Delta m_{B_d}/\Delta m_{B_s}$) and from $K \rightarrow \pi\nu\bar{\nu}$ [26].

1.5.2 $K_L^0 \rightarrow \pi^0\nu\bar{\nu}$ in BSM

The $K_L^0 \rightarrow \pi^0\nu\bar{\nu}$ decay plays a special role in the investigation of new physics beyond the Standard Model. The theoretical cleanness of $K_L^0 \rightarrow \pi^0\nu\bar{\nu}$ remains valid in essentially all extensions of the Standard Model. Also the $K_L^0 \rightarrow \pi^0\nu\bar{\nu}$ decay can determine the new origin of CP violation with small theoretical uncertainties. In contrast to the $K_L^0 \rightarrow \pi^0\nu\bar{\nu}$ decay, the measurement of CP violation in the B meson system, such as non-leptonic two-body decay ($B \rightarrow \pi\pi$, $B \rightarrow K\pi$, etc.) are vulnerable to the hadronic uncertainties in the relevant observables. Moreover, the $K_L^0 \rightarrow \pi^0\nu\bar{\nu}$ decay is sensitive to new flavor interactions and/or CP violation phases in the intermediate state.

An explicit example was pointed out in references [23, 24]. Buras *et al.* predicted a large phase of the new origin of CP violation, which leads to an enhancement of the electroweak penguin process shown in Figure 1.5 ("Enhanced EW penguin"). This effect can be implemented in both K and B meson system universally. It would provide a much better fit of recent $B \rightarrow \pi K$ data from B factories [25].

Table 1.1 lists the models beyond the Standard Model and the predicted branching ratio of the $K_L^0 \rightarrow \pi^0\nu\bar{\nu}$ decay. In the Minimal Flavor Violation (MFV) hypothesis, there are no additional CP violation phases and the flavor mixing other than the contribution governed by the CKM matrix in the Standard Model. Thus, deviations from the Standard Model amplitudes rarely exceed 20% level. Moreover, since there are no additional CP violation phases, the relation between the magnitude of the CP violation in the $K_L^0 \rightarrow \pi^0\nu\bar{\nu}$ decay and the CP asymmetry measured in $B \rightarrow J/\psi K_S^0$ (Equation 1.59) must be satisfied. On the other hand, in general Minimal Supersymmetric Standard Model (MSSM), it is possible to implement new CP violation phases. In the general MSSM, the branching ratio of the $K_L^0 \rightarrow \pi^0\nu\bar{\nu}$ decay can be as large as a few times 10^{-10}. The effect of new CP violation phase to $K_L^0 \rightarrow \pi^0\nu\bar{\nu}$ is different from that of $\Delta F = 2$ processes, e.g. $K^0 - \overline{K^0}$ and $B^0 - \overline{B^0}$ mixing. This implies that the relationship in Equation 1.59 is broken, hence some differences would appear between the magnitude of the CP violation in the $K_L^0 \rightarrow \pi^0\nu\bar{\nu}$ decay and the CP asymmetry measurement from the $B \rightarrow J/\psi K_S^0$ decay as shown in Figure 1.6.

Table 1.1: List of the models beyond the Standard Model and the predicted branching ratio of the $K_L^0 \to \pi^0 \nu \bar{\nu}$ decay.

Reference	$Br(K_L^0 \to \pi^0 \nu \bar{\nu})/10^{-11}$	model
[27]	$<$ a few $\times 10$	General MSSM
[23, 24]	31 ± 10	Enhanced EW penguin
[28]	< 4.6	MFV
[29]	< 4.0	MFV w/ universal extra dimension
[30, 31]	$3.1 - 6$	MFV w/ littlest-Higgs model

1.6   History of the $K_L^0 \to \pi^0 \nu \bar{\nu}$ Search

There were five experiments on the $K_L^0 \to \pi^0 \nu \bar{\nu}$ decay before we started the E391a experiment, as shown in Figure 1.7.

The first study was performed by Littenberg [32]. He extracted a limit from the data of Cronin *et. al.* [5] for the $K_L^0 \to \pi^0 \pi^0$ decay. The limit was

$$Br(K_L^0 \to \pi^0 \nu \bar{\nu}) \ < \ 7.6 \times 10^{-3} \quad (90 \% \text{ C.L.}) . \tag{1.65}$$

The following studies were carried out in two different approaches.

The first approach used the $\pi^0 \to e^+ e^- \gamma$ decay to identify the $K_L^0 \to \pi^0 \nu \bar{\nu}$ decay. The advantage of using $\pi^0 \to e^+ e^- \gamma$ is that the decay vertex can be reconstructed with $e^+ e^-$ tracks. Thus, one can reconstruct the invariant mass of $e^+ e^- \gamma$ and require it to be m_{π^0}. On the other hand, a disadvantage is that the branching ratio of the $\pi^0 \to e^+ e^- \gamma$ decay is so small ($\sim 1\%$) that one needs a larger number of K_L^0's.
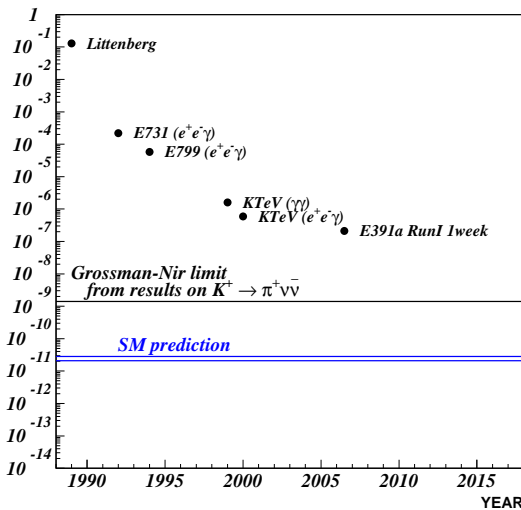
Figure 1.7: History plot of the search for the $K_L^0 \to \pi^0 \nu \bar{\nu}$ decay. In this figure, $(\gamma \gamma)$ and $(e^+ e^- \gamma)$ denote the experimental approaches using the $\pi^0 \to \gamma \gamma$ decay and $\pi^0 \to e^+ e^- \gamma$ decay, respectively.

Another approach used the $\pi^0 \to \gamma\gamma$ decay. The advantage of using the $\pi^0 \to \gamma\gamma$ decay is that the branching ratio of the $\pi^0 \to \gamma\gamma$ is $\sim$99 %. KTeV experiment set a limit on the branching ratio [33]:

$$Br(K_L^0 \to \pi^0 \nu\bar{\nu}) \;<\; 1.6 \times 10^{-6} \quad (90\,\%\ \text{C.L.})\;, \tag{1.66}$$

based on a special run taken in one day. As shown in Figure 1.8, one event was observed in the signal region while 3.5 ± 0.9 background events were expected. The main backgrounds sources were

- Other K_L^0 decays such as $K_L^0 \to \pi^0\pi^0$ where two out of four photons were missed,

- Beam-associated backgrounds such as the $\Lambda \to n\pi^0$ decay and π^0 production by the neutron interaction with detector materials.

The latter dominated in the experiment.

If one wants to search for $K_L^0 \to \pi^0\nu\bar{\nu}$ with the $\pi^0 \to \gamma\gamma$ decay, it is necessary to improve the detector system in order to catch all the extra photons, and improve the neutral beam in order to reduce the number of Λ's and neutrons. In addition, it is important to reduce the amount of detector materials in the beam in order to avoid neutron interactions.

In KTeV experiment, they also analyzed using the data of $\pi^0 \to e^+e^-\gamma$ taken for 46 days and have obtained the best upper limit [34] until we started the E391a experiment. The final plot is shown in Figure 1.8.

$$Br(K_L^0 \to \pi^0\nu\bar{\nu}) \;<\; 5.9 \times 10^{-7} \quad (90\,\%\ \text{C.L.}) \tag{1.67}$$

However, this is still a few orders of magnitude higher than the SM prediction.
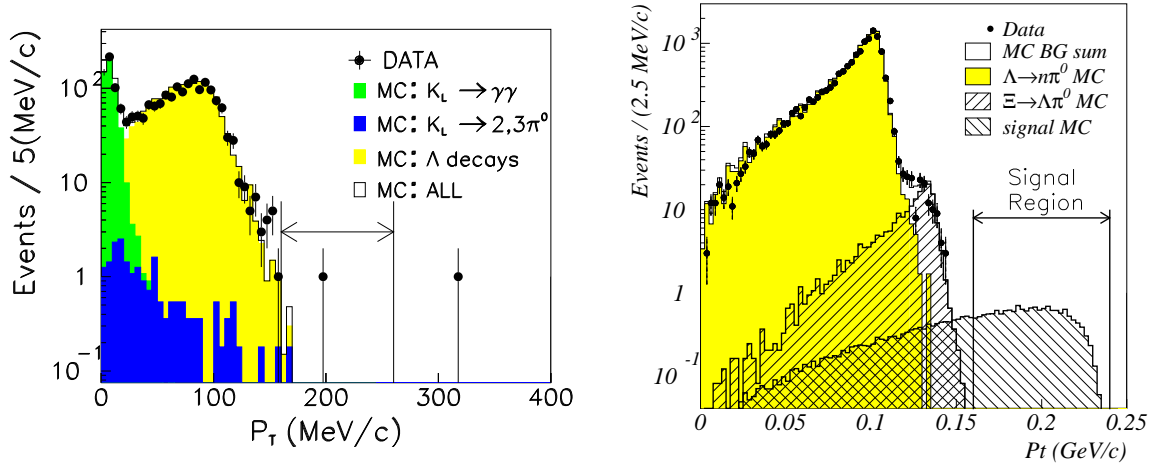
Figure 1.8: Distribution of the transverse momentum for the final remaining events in the search for $K_L^0 \to \pi^0\nu\bar{\nu}$ decay with $\pi^0 \to \gamma\gamma$ and $\pi^0 \to e^+e^-\gamma$ decay by the KTeV collaboration [33, 34]. The arrow shows the signal region: $160 \leq P_T(\text{MeV/c}) \leq 260$.

1.7 KEK-PS E391a Experiment

In order to reach the sensitivity of the SM prediction, we adopted a step-by-step approach. First, we started the first dedicated experiment for the $K_L^0 \to \pi^0 \nu\bar{\nu}$ decay, the E391a experiment, at the 12 GeV proton synchrotron (PS) in High Energy Accelerator Research Organization (KEK). The purpose of E391a is to establish a new experimental method. In E391a experiment, we identified the $K_L^0 \to \pi^0 \nu\bar{\nu}$ decay using $\pi^0 \to \gamma\gamma$ and introduced several new approaches to suppress the number of background events. Based on the experience in E391a, we will proceed to the next step experiment at a high intensity 50(30) GeV PS in J-PARC in 2009-2010.

E391a had three data taking times. The first run, Run-I, started in February 2004. In Run-I data analysis, the basic methods to identify the signal were established [35]. However, we had a few problems in Run-I. One of them was that the membrane happened to droop in the beam at CV, and became the huge background source, as shown in Figure 1.9. As a consequence of the problem, we had much more acceptance loss than we expected, and we obtained a upper limit:

$$Br(K_L^0 \to \pi^0 \nu\bar{\nu}) < 2.1 \times 10^{-7} \quad (90 \text{ \% C.L.}) \tag{1.68}$$

in Run-I [36].

After solving the problems and adding several upgrades for the experimental apparatus, we started the second run period, Run-II, in February 2005. In this thesis, new results of the search for $K_L^0 \to \pi^0 \nu\bar{\nu}$ using the full data taken in Run-II are described. In this analysis, we developed the method to estimate backgrounds due to the neutrons around the core region of the neutral beam using the Monte Carlo simulation. In addition, we developed the methods to reduce the backgrounds and achieved the estimation of the backgrounds consistent with data, while the acceptance loss was improved with the upgrades in the detector and the new analysis methods.

1.8 Outline of This Dissertation

In this chapter we have discussed the basic issues concerning the phenomenology of the neutral kaon, CP violation, and $K_L^0 \to \pi^0 \nu\bar{\nu}$ decay, and briefly summarized the searches for $K_L^0 \to \pi^0 \nu\bar{\nu}$ in the past. The next chapter explains the techniques and concepts of the experiment. We describe the experimental apparatus in Chapter 3. The run summary including periods and species is described in Chapter 4.

In order to measure the kaon flux, it is necessary to understand the detector acceptance. This is obtained from the Monte Calro simulation, which is summarized in Chapter 5. Also in Chapter 5, we describe the method of neutron MC for the background estimation. Chapter 6 explains the event reconstruction method. Chapter 7 describes the event selection to suppress the number of background events. Chapter 8 describes the number of collected K_L^0 decays. Its systematic uncertainties to the sensitivity of $K_L^0 \to \pi^0 \nu\bar{\nu}$ are also discussed therein. The background estimation is provided in Chapter 9. Finally, in Chapter 10 we present the results of this search, and Chapter 11 concludes this dissertation.
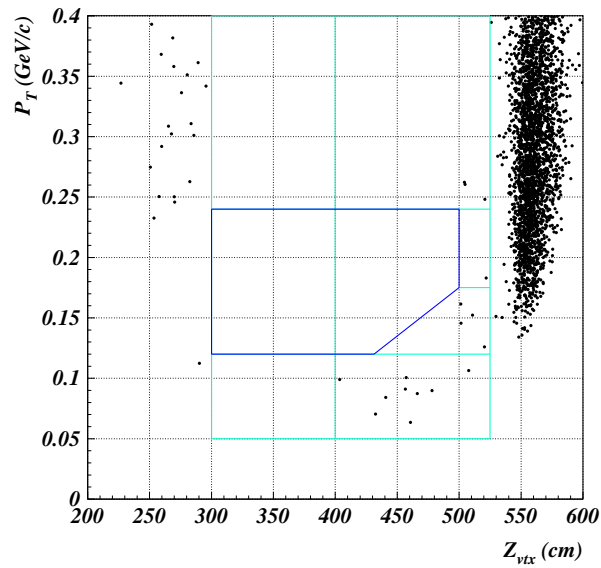
Figure 1.9: Final plot of the E391a RunI 1week result. There are many events around $Z_{vtx} = 570cm$ due to the material in the beam-hole.

Chapter 2

Design of the $K_L^0 \rightarrow \pi^0 \nu \bar{\nu}$ experiment

2.1 Overview

The first dedicated experiment to $K_L^0 \rightarrow \pi^0 \nu \bar{\nu}$ was proposed in 1996 [37] at KEK. With some modifications to the original design, the experiment was approved in 2001 as KEK-PS E391a. The past experimental achievement by the time was only $Br(K_L^0 \rightarrow \pi^0 \nu \bar{\nu}) < 5.9 \times 10^{-7}$ at the 90 % C.L., which is still several orders of magnitude higher than the SM prediction. Thus, the purpose of the E391a experiment was to establish a new experimental method to the measurement of the $K_L^0 \rightarrow \pi^0 \nu \bar{\nu}$ decays in higher sensitivity.

In order to improve the sensitivity to the $K_L^0 \rightarrow \pi^0 \nu \bar{\nu}$ decay, it is necessary to increase both the number of K_L^0 decays and the signal acceptance. At the same time, we should keep the number of background events small enough.

In this chapter, a general description of the sensitivity in Kaon rare decay experiments appears first. Then detection methods of $K_L^0 \rightarrow \pi^0 \nu \bar{\nu}$ and possible background sources are discussed. Finally, our design concept of the E391a experiment is explained.

2.2 Experimental Sensitivity

In general, the branching ratio to be measured is represented as:

$$Br(signal) = \frac{N_{signal}}{N_{decay} \times A_{signal}} \quad (2.1)$$

where N_{signal} is the observed number of signal events, N_{decay} is the total number of the decays in the signal region, and A_{signal} is the signal acceptance for the events that decayed in the signal region. A_{signal} includes the geometrical acceptance and the detection efficiency of the detector for daughter particles, the survival probability of the signal through the requirements in data analysis, and so on.

To measure N_{decay}, we simultaneously collected data of signal candidate events and the decay modes whose branching ratio are already known well. Such decay channels are called the "normalization" modes. N_{decay} is calculated as

$$N_{decay} = \frac{N_{norm}}{A_{norm} \times Br(norm)} \;, \quad (2.2)$$

19

where N_{norm}, A_{norm} and $Br(norm)$ are the observed number of events, the acceptance and the branching ratio of the normalization mode, respectively.

The "Single Event Sensitivity(SES)" is expressed as

$$\text{SES} = \frac{1}{N_{decay} \times A_{signal}} \ . \tag{2.3}$$

In other words, the experiment is expected to observe $Br(signal)$/SES events on average.

2.3 Experimental Method

The signature of the $K_L^0 \to \pi^0 \nu \bar{\nu}$ decay is two photons from π^0 decay and no other particles in the final state. The K_L^0 decay modes that have exclusively two photons in the final state are $K_L^0 \to \pi^0 \nu \bar{\nu}$ and $K_L^0 \to \gamma\gamma$ decays. All the other decay modes have at least two charged particles or at least four photons, and these decays can be distinguished from the signal by detecting extra particles other than two photons. We can discriminate the $K_L^0 \to \pi^0 \nu \bar{\nu}$ decay from the $K_L^0 \to \gamma\gamma$ decay by requiring a finite transverse momentum (P_T) of the detected two photon system.

The positions and energies of the two photons in the electromagnetic calorimeter are the only measurable quantities. Once we assume these two photons come from a π^0 decay, the decay position along the K_L^0's flight direction can be calculated, assuming the invariant mass of the two photons equals to the π^0 mass. The event whose vertex position is in the proper decay volume is regarded as a π^0 decay. In addition, if there is no other activities in any veto detector, the event is a candidate of $K_L^0 \to \pi^0 \nu \bar{\nu}$.

As mentioned in the previous chapter, better experimental sensitivity can be expected by detecting $\pi^0 \to \gamma\gamma$, instead of the $\pi^0 \to e^+ e^- \gamma$ decay used in the past searches [34], because the $Br(\pi^0 \to \gamma\gamma)$ is ~ 80 times larger than the $Br(\pi^0 \to e^+ e^- \gamma)$. In other words, π^0 detection by tagging two photons yields large A_{signal} in Equation 2.3 and this results in better SES. In order to obtain a large geometrical acceptance for the signal mode, the electromagnetic calorimeter is set at the downstream end of the decay region because two photons from π^0 decay are boosted in the K_L^0 direction. From the experience of the past experiment, the background rejection is the key issue of this method. For the purpose, the decay region should be surrounded by veto detectors with high efficiencies. More detailed discussions follow in the next section.

2.4 Backgrounds

Since the signature of the $K_L^0 \to \pi^0 \nu \bar{\nu}$ decay is a single π^0 reconstructed from two photons, there are various background sources.

2.4.1 K_L^0 Decay

Table 2.1 shows the branching fractions of the decay modes of K_L^0. 3 of 4 major decay modes of K_L^0, $K_L^0 \to \pi^\pm e^\mp \nu$, $K_L^0 \to \pi^\pm \mu^\mp \nu$, and $K_L^0 \to \pi^+ \pi^- \pi^0$, contain charged particles in the final states. Primary rejection method is to detect charged particles and discriminate them from the signal. Thus, charged particle detection with high efficiency is necessary.

Table 2.1: Branching fractions of the main decay modes of K_L^0 [8]. For $K_L^0 \to \pi^0 \nu \bar{\nu}$, the predicted branching fraction by the Standard Model is shown. For the decay modes that include one or more π^0, the kinematic limits of the momentum for the π^0's are indicated.

K_L^0 Decay Modes	Branching Fraction	p_{max} (MeV/c)
$\pi^0 \nu \bar{\nu}$	$[(2.49 \pm 0.39) \times 10^{-11}]$	231
$\pi^\pm e^\mp \nu$	$(40.53 \pm 0.15)\%$	–
$\pi^\pm \mu^\mp \nu$	$(27.02 \pm 0.07)\%$	–
$\pi^0 \pi^0 \pi^0$	$(19.56 \pm 0.14)\%$	139
$\pi^+ \pi^- \pi^0$	$(12.56 \pm 0.05)\%$	133
$\pi^0 \pi^0$	$(8.69 \pm 0.04) \times 10^{-4}$	209
$\pi^+ \pi^-$	$(1.976 \pm 0.008) \times 10^{-3}$	–
$\gamma\gamma$	$(5.48 \pm 0.05) \times 10^{-4}$	–
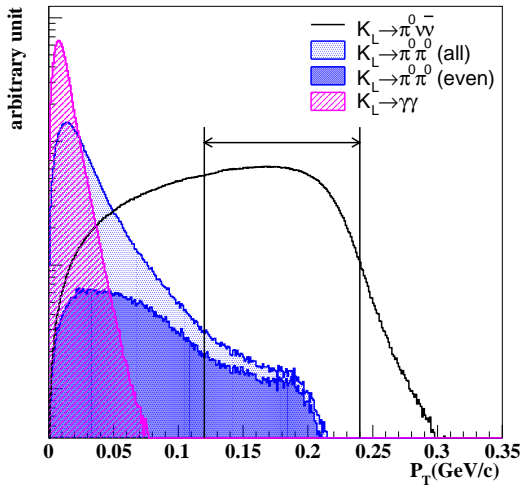
Figure 2.1: Histograms shows the distribution of the transverse momentum (P_T) of two photon system for $K_L^0 \to \pi^0 \nu \bar{\nu}$, $K_L^0 \to \pi^0 \pi^0$, and $K_L^0 \to \gamma\gamma$ decays obtained by a Monte Carlo simulation. The category labeled "even" in $K_L^0 \to \pi^0 \pi^0$ means that both of the photons come from the same π^0. The signal region can be set for instance, as indicated with the lines and the left-right arrow.

If some photons from a K_L^0 decay or other reactions are undetected, it could become a background event. One example is the $K_L^0 \to \pi^0 \pi^0$ decay in which two out of four photons are missed. Figure 2.1 shows the distribution of the transverse momentum (P_T) of two photons. The signal and the background events can be discriminated by requiring a large transverse momentum. However, the "even" background in the $K_L^0 \to \pi^0 \pi^0$ decay, in which both of the two photons from the same π^0 are lost, could have large P_T. We should reduce such background events as much as possible.

One of the sources to miss photons is a detection inefficiency. There are two major mechanisms that cause the detection inefficiency.

1. Electro-magnetic interaction:

    (a) Punch-through effect, in which a photon passes through the detector without interaction

with the material. The inefficiency for this effect is described as

$$\text{Inefficiency} = e^{-\sigma \cdot \rho \cdot l} \tag{2.4}$$

where l is the length of the detector, σ is the normalized cross section(cm^2/g) and ρ is the density(g/cm^3).

(b) Sampling effect. For a sampling calorimeter such as lead / scintillator sandwich type, the visible energy deposit in the scintillator could be below the detection threshold due to shower fluctuations.

2. Photo-nuclear interaction:
   The photo-nuclear interaction is the reactions in which the incident photon is absorbed by a nucleus. The excited nuclei emit protons, neutrons or photons. If only neutrons are emitted, the incident photon would not be detected.

The photon inefficiency depends on the incident photon energy and the the detector. The photon inefficiency including the photo-nuclear effects was measured with both a lead / scintillator sandwich detector and a CsI crystal for photons with the energies below 1 GeV [38] and above 1 GeV [39] by ourselves.

Another mechanism to miss photons is so-called "fusion", in which two nearby photons in the electromagnetic calorimeter are reconstructed as one photon. It mainly depends on the size of segmentation of the electromagnetic calorimeter because most portion of the electromagnetic shower lies within one Moliére radius. Also it depends on a algorithm for finding showers.

2.4.2   Beam Interaction

The K_L^0 beam in this experiment was produced by hitting a target with 12 GeV primary protons (described in Section 3.1). Huge amount of neutrons were produced by the hadronic interaction in the target. If a neutron in the beam interacts with a detector material or with residual gas, it produces particles that can be a source of background.

1. π^0 production
   If one π^0 is produced by the beam particles, it fakes the signal. Usually, interactions with detector materials can be separated fro with the signal since the reconstructed vertex points the detector position properly. However, mismeasurement of the energies of photons due to leakage of electromagnetic shower, photo nuclear effect, and additional energy deposition by other particles, shifts the reconstructed vertex position into the signal region.

2. η production
   η mesons are also produced in the material, and they decay into two photons with $Br(\eta \to \gamma\gamma)$ of about 40%. Since the vertex is reconstructed with the assumption that the invariant mass of two photons equals to the π^0 mass, the distance between the reconstructed vertex and the location of the calorimeter is miscalculated.

The key issues to reject these types of backgrounds are to obtain good energy resolution and to detect associated particles from the interaction. And in order to reduce the interaction itself, it is necessary to achieve a narrow beam profile.

2.5 Concepts of the E391a Experiment

The E391a experiment is designed to search for the $K_L^0 \to \pi^0 \nu \bar{\nu}$ decay with high sensitivity while suppressing the backgrounds described above. Here, the ideas for our detector system and K_L^0 beam are described. These ideas are also meant to be applied to high sensitivity experiments in the future. Detailed description of each detector component follows in the next chapter.

2.5.1 Narrow Beam Line

Since we identified the $K_L^0 \to \pi^0 \nu \bar{\nu}$ signal by requiring a large P_T on the reconstructed π^0's, the resolution of P_T was crucial. In order to reduce the uncertainty of the decay position of π^0's in the transverse direction, we built a very narrow neutral beam line with the cone angle of 2 mrad. This was called "pencil" beam.

2.5.2 Photon Detection

We built a hermetic calorimeter system to detect all the particles from K_L^0 decays and other reactions. Figure 2.2 shows a conceptual view of the hermetic detector. We used CsI crystals as the electromagnetic calorimeter and several sandwich type detectors to detect extra particles. In order to suppress events that decayed upstream of the detector surrounding the K_L^0 decay regions, we built an additional detector also at the upstream of the hermetic detector system.

Even through the hermeticity of the detector system is required, a beam hole is necessary in order to avoid interactions of the neutral beam with the detector materials. This allows some decay particles to escape into the beam hole. A detector is placed at the end of the beam to catch such particles, but its detection efficiency is degraded due to the high counting rates in the detector. This increases the overall photon inefficiency of the detector system. Thus, the pencil beam was also effective to reduce such inefficiency.

2.5.3 Reduction of Neutron Interactions

In order to reduce π^0's produced by neutron interactions, we take two approaches. First, we evacuate the air in the decay region down to 10^{-4} Pa to avoid interactions between neutrons in the beam and the residual gas. With this pressure, the number of background events is negligible (≤ 0.1 events) for an experiment searching for $K_L^0 \to \pi^0 \nu \bar{\nu}$ with the sensitivity of $O(10^{-10})$ [40]. However, such high vacuum is hard to be achieved with the detector components due to a large amount of out-gassing from detector materials. In order to avoid this problem, we divided the vacuum region into two by a thin film,
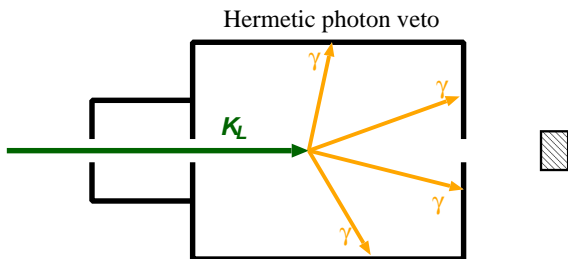
Figure 2.2: Conceptual view of the hermetic detector. The K_L^0 decay region including the beam hole is surrounded by the detector material in order to detect all photons from K_L^0 decay.

and the detectors were put in a low vacuum region ($\sim$0.1 Pa). We will describe details of the vacuum system in Section 3.3.

Second, we reduced the beam halo component as low as possible to minimize their interactions with the detector materials. By optimizing the beam line, especially the configuration of the collimators, the rate of the beam halo is 4 orders of magnitude lower than the rate of the beam core in the E391a experiment. The beam line is described in detail in Section 3.1.

2.6 Summary

By the time the E391a experiment started, the best limit on the branching ratio of $K_L^0 \to \pi^0 \nu \bar{\nu}$ was achieved by using π^0 Dalitz mode. However, we adopted the detection method to $\pi^0 \to \gamma\gamma$ in order to obtain much higher sensitivity. The backgrounds are suppressed by the hermetic veto system and the "pencil" beam for rejecting the extra particles in the final state, and reducing the neutron interactions to produce the single π^0's, respectively.

In the next chapter, the details of the experimental apparatus, which were constructed to satisfy these purposes, will be explained.

Chapter 3

Experimental Apparatus

This chapter describes the K_L^0 beam, detector components, vacuum system, trigger and data acquisition system (DAQ).

3.1 Beam Line

E391a was performed in the East Counter Hall (ECH) of KEK 12 GeV Proton Synchrotron (KEK-PS). Neutral long-lived kaons produced in a target enter the experimental area through the neutral beam line.

3.1.1 K_L^0 Production

Figure 3.1 shows the layout of the ECH. Primary protons, accelerated up to the kinetic energy of 12 GeV in 2 seconds, were extracted continuously to ECH through the EP2-C beam line. The extraction took 2 seconds in the Slow Extraction Mode. This extraction period is called a "spill". Typical beam intensity at production the target was 2.6×10^{12} protons per spill. The profile of the primary proton beam was an ellipse with $\sigma = 1.1$ mm and $\sigma = 3.3$ mm in the vertical and horizontal axes, respectively [41].

The production target was made of platinum(Pt) with 60 mm in length ($0.68\lambda_I$, $20X_0$, where λ_I and X_0 were the interaction and radiation lengths, respectively) and 8 mm in diameter. The secondary neutral beam line was located in the direction of $4°$ in horizontal with respect to the primary beam. This production angle was chosen in order to reduce the number of neutrons compared to the number of K_L^0's because the beam neutron interaction with the residual gas could be a background source in the neutral beam. The neutron-to-K_L^0 ratio was ~ 60 at the target.

The target rod was aligned to the direction of the neutral beam line to minimize projected image viewed from the detector system.

3.1.2 Neutral Beam Line

The "K0" neutral beam line for the E391a experiment was constructed to satisfy the following conditions.

The beam size was set to be small ("pencil" beam). Such a beam reduced the uncertainty in the transverse momentum of the π^0 from the $K_L^0 \rightarrow \pi^0 \nu \bar{\nu}$ decay. Since the transverse momentum of π^0 was reconstructed by assuming that the π^0 decay vertex was on the beam axis, a large beam would
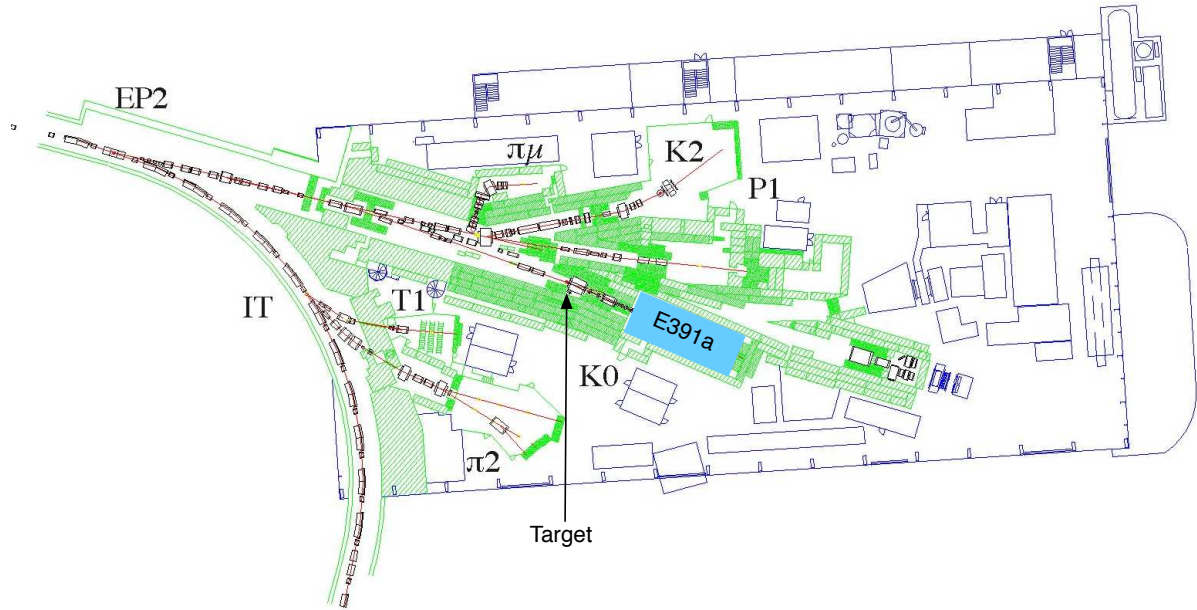
Figure 3.1: Layout of the East Counter Hall at KEK. K_L^0' are produced at the target and extracted to the K0 beam line. The arc in the left-hand side is a part of the PS. The E391a experimental area is the blue shaded region.

make the transverse momentum resolution worse. The beam hole in the downstream of the detector was small and thereby reduced the probability that photons went through the beam hole without being detected. If a neutron in the halo component interacted with the detector materials, it could become a background event; the halo should be reduced as much as possible.

The neutral beam line consisted of a pair of sweeping magnets, two stages of collimation using six sets of collimators (C1 – C6), lead(Pb) and beryllium(Be) absorbers and a vacuum pipe as shown in Figure 3.2. The total length from the target to the exit of the last collimator (C6) was 11 m and the total length of the collimators corresponded to $47\lambda_I$. The total length of the beam line was long enough to reduce hyperon decays, such as $\Lambda \to n\pi^0$.

The Pb and Be absorbers were set to reduce photons and neutrons in the beam, respectively. The first three collimators, C1, C2 and C3, were used to define the beam in the aperture of 2 mrad. The last two collimators, C5 and C6, were used to trim the beam halo. A part of halo neutrons were produced at the C6 by secondary neutrons and by charged pions from K_L^0 decays. In order to remove the background events due to the neutrons produced at C6, plastic scintillator rings with a thickness of 1 cm were installed between the tungsten disks in the downstream half of the C6. Scintillation light was read out through wavelength-shifting fibers arranged at the outer periphery of the scintillator disks.

The fourth collimator, C4, was used to reduce thermal neutrons, which caused accidental hits in the detectors. C4 consisted of thin gadolinium-oxide(Gd_2O_3) sheets. It was confirmed that C4 reduced the thermal neutron flux by an order of magnitude [41].

Figure 3.3 shows the beam profiles for photons, neutrons, and charged particles at the exit of C6, obtained by Monte Carlo simulation and the measurement in beam survey. The neutral beam was
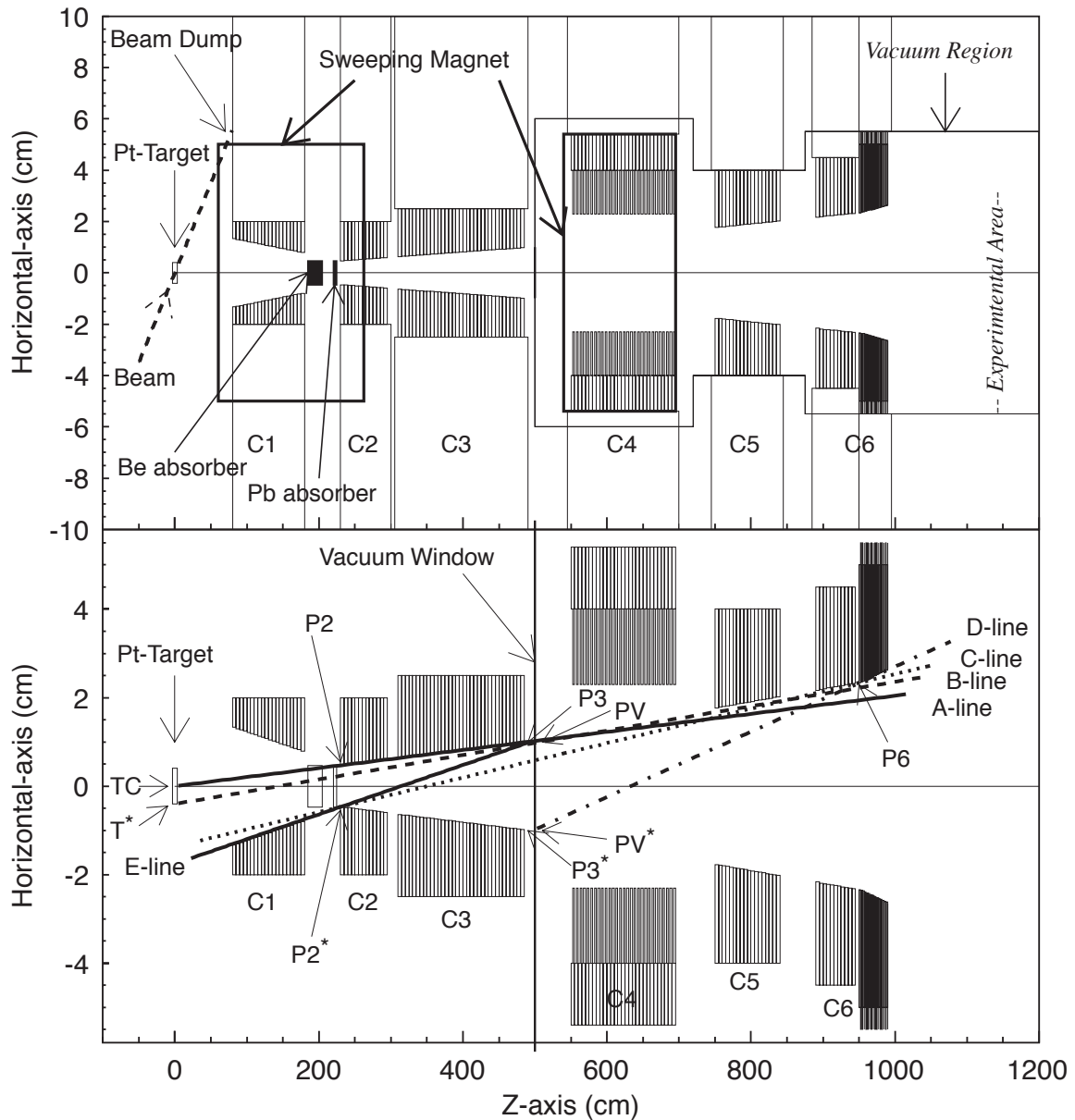
Figure 3.2: Neutral beam line for E391a. The top figure is the cutaway view of the collimation system which indicates the geometrical sizes and positions of the components (note the difference in the vertical and horizontal scales). All the collimators consisted of cylindrical disks of 5cm-thick tungsten. The bottom figure shows details of the collimation scheme. The explanations of the lines connecting parts of the collimator system are given in the reference [41].
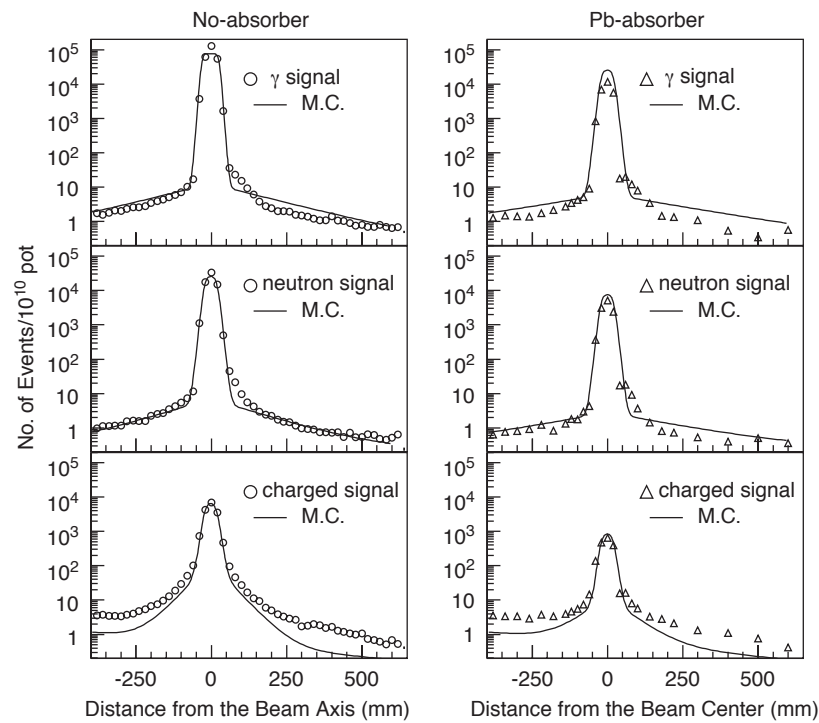
Figure 3.3: Beam profiles of the neutral beam line for photons, neutrons, and charged particles [41].

sharply collimated, and the flux ratio of the halo to the core was found to be lower than 10^{-4}. Figure 3.4 shows the K_L^0 momentum spectrum at exit of the C6 by the Monte Carlo simulation described in Chapter 5. The average momentum of K_L^0 was 2.6 GeV/c at C6.
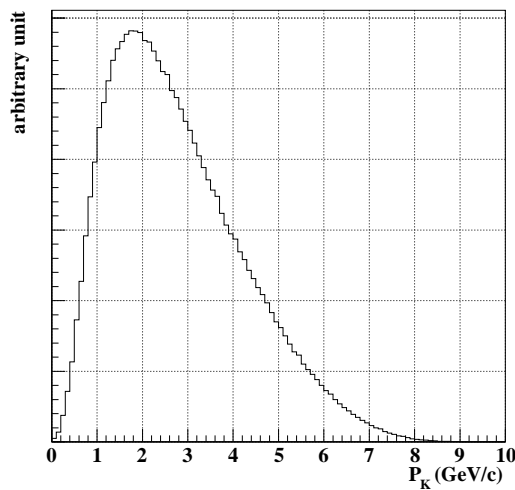
Figure 3.4: K_L^0 momentum distribution at the exit of the beam line (C6) obtained by the Monte Carlo simulation

3.2 Detector Components

Figure 3.5 shows a side view of the E391a detector. The locations and dimensions of the detector components are listed in Table 3.1.

K_L^0's decayed in the decay region of 10^{-5} Pa. Most of the detector components were located inside the vacuum vessel to avoid the absorption of photons and charged particles before reaching the detector.

The electromagnetic calorimeter was placed at the downstream end of the decay region to detect the energies and positions of the two photons from π^0. Other detector components were used to detect particles that did not hit the calorimeter. The decay region was covered by Main Barrel (MB). The upstream of the decay region was covered by Front Barrel (FB) and Collar-Counter-02 (CC02) to suppress background events from K_L^0's decaying in the upstream of the decay region. To detect photons going parallel to the beam and through the beam hole, we placed CC03, CC04, CC05, CC06 and CC07 perpendicularly to the beam axis; these detectors surrounded the beam holes. Back Anti (BA) was placed at the end in the beam in order to detect photons going through the beam hole and undetected by other detectors. To detect charged particles, three charged veto detectors CV, BCV and BHCV were placed.

The total length of the detector system was 11 m. Table 3.1 lists the positions, dimensions, detector configurations and the number of readout channels of each detector component.

The coordinate system was defined to describe the positions and orientations of the detector elements. The z-axis was to the beam direction. The reference point in the z-axis was the front surface of FB. The y-axis was the vertically upward direction of the system. The x-axis satisfied the right-handed system.

3.2.1 Electromagnetic Calorimeter

The main electromagnetic calorimeter was made of an array of undoped CsI crystals. As shown in Figure 3.6, the electromagnetic calorimeter was in a circular shape with 1.9 m in diameter. A collar counter 03 (CC03) was installed inside of the calorimeter with 12 cm × 12 cm hole, which is described later. The electromagnetic calorimeter was located at $z = 614.8$ cm. It consisted of 576 CsI crystals located within a cylindrical support structure. Most of them were square shape. In order to fit the
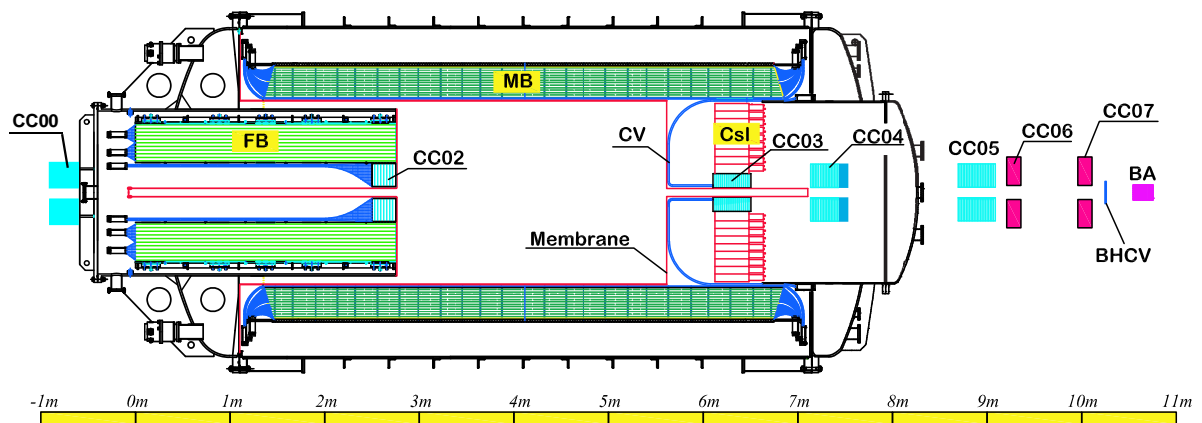
Figure 3.5: Side view of the E391a detector. K_L^0's enter from the left.

Table 3.1: Locations, dimensions, brief configurations and the number of readout channels of each detector element.

detector	z position (cm)	transverse size (cm)	configuration	# of readouts
CC00	-85.5	outer diameter: 21.0 inner diameter: 8.2	tungsten/scint.	4
FB	0.0	outer diameter: 145.0 inner diameter: 62.0	lead/scint.	32
MB	134.8	outer diameter: 276.0 inner diameter: 200.0	lead/scint.	128
BCV	134.8	outer diameter: 200.0 inner diameter: 199.0	pastic scint.	32
CC02	239.1	outer diameter: 62.0 inner diameter: 15.8	lead/scint.	8
CV	554.8	outer diameter: 190.6 inner: 12.0 (square)	plastic scint.	32+4
CsI	614.8	outer diameter: 190.6 inner: 25.0 (square)	CsI(pure)	576
CC03	609.8	outer: 25.0 (square) inner: 12.0 (square)	tungsten/scint.	6
Sandwich	614.8	(outside of CsI calorimeter)	lead/scint.	24
CC04	710.3	outer: 50.0 (square) inner: 12.6 (square)	lead/scint.	4
CC05	874.1	outer: 50.0 (square) inner: 12.6 (square)	lead/scint.	6
CC06	925.6	outer: 30.0 (square) inner: 15.0 (square)	lead glass	10
CC07	1000.6	outer: 30.0 (square) inner: 15.0 (square)	lead glass	10
BHCV	1029.3	23.0 (square)	plastic scint.	8
BA	1059.3	24.5 (square)	lead/scint. Quartz	36 42

calorimeter inside the support structure, specially shaped CsI crystals (Edge CsI) and lead / scintillator sandwich counter (Sandwich module) were placed at the outer edge of electromagnetic calorimeter.

CsI Crystals

Two different sizes of crystals were used in the array: 496 crystals were in 7 cm $\times$ 7 cm $\times$ 30 cm($=$ $16X_0$) and 24 crystals were in 5 cm $\times$ 5 cm $\times$ 50 cm($= 27X_0$). The 7 cm $\times$ 7 cm $\times$ 30 cm crystals were called "Normal CsI", which were used in a past experiment at KEK-PS. And the 5 cm $\times$ 5 cm $\times$ 50 cm crystals were called "KTeV CsI" since we borrowed them from the KTeV experiment.

Each Normal CsI crystal was wrapped with a 100 μm thick Teflon sheet and then wrapped with a 20 μm thick Aluminized mylar in order to isolate each crystal optically and to improve the light collection. The Normal CsI crystal yielded typically 15 photoelectrons per the energy deposition of 1 MeV. The scintillation light produced by the electromagnetic showers in the CsI crystals was detected by the photo-multiplier tubes (PMTs) mounted on the back of each crystal. As shown in Figure 3.7, each crystal was viewed by a 2 inch Hamamatsu R4275-02 PMT through a 3 mm thick silicone cookie and a UV transmitting filter that reduces the slow component of the scintillation light from the CsI crystal. Since these modules were operated in vacuum, the PMT divider was modified to reduce heat dissipation and heat conduction from the divider to the PMT. This was achieved by decreasing the divider current and taking a larger gap between the PMT and the divider circuit board as shown in Figure 3.7. We also filled the PMT divider with a 5 mm thick heat conductive glue (METACAST 5448). The PMT divider was connected to a cooling water pipe. The cooling system is described in Section 3.3.

Each KTeV CsI was wrapped with a 13 μm thick Aluminized mylar. The KTeV CsI yielded typically 25 photoelectrons per MeV. Each KTeV CsI was viewed by a 1.5 inch Hamamatsu R580-UV PMT through a 5 mm thick silicone cookie and a UV transmitting filter, as shown in Figure 3.7. The PMT divider for KTeV CsI was used with the same structure as those for the Normal CsI crystals. The PMT divider was filled with a heat conductive glue (EN11) and connected the divider to a cooling water pipe.
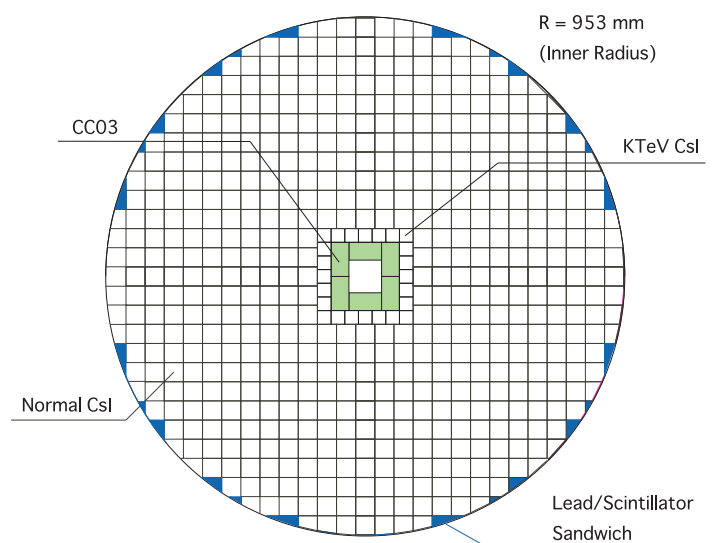
Figure 3.6: Cross sectional view of the electromagnetic calorimeter.
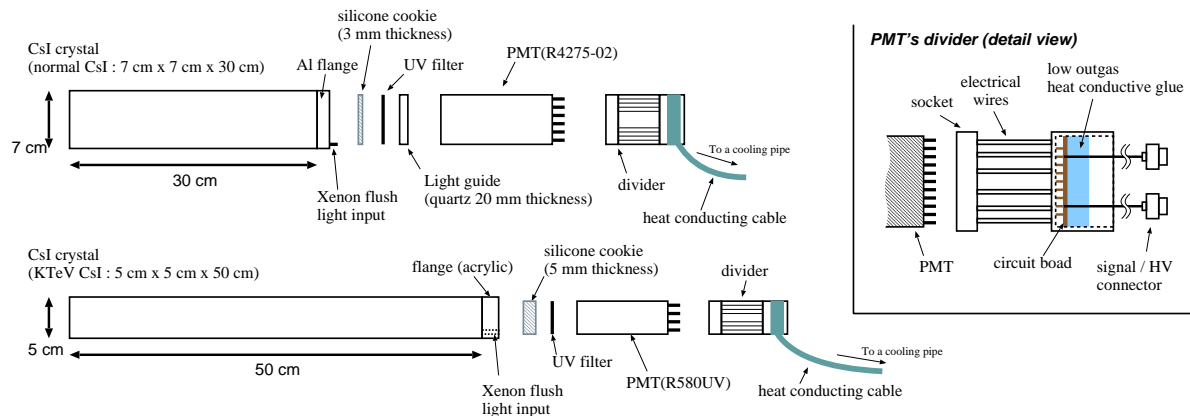
Figure 3.7: Schematic drawing of CsI crystal and associated equipments.
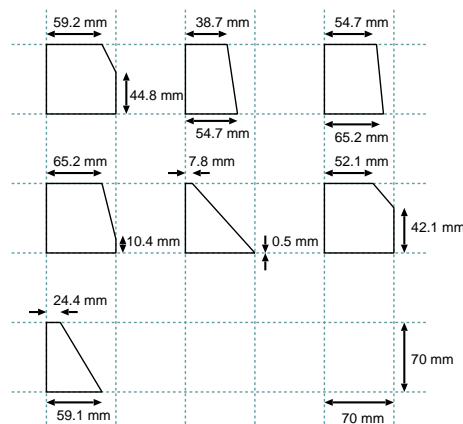
Figure 3.8: Edge CsI crystals in seven different shapes.

56 crystals in 7 cm $\times$ 7 cm $\times$ 30 cm were cut into seven different shapes to fit the calorimeter inside the support structure as shown in Figure 3.8. The optical treatment and its light yield was almost the same as the Normal CsI. $1\frac{1}{8}$ inch Photonis XP 2978 PMTs were used for smaller 32 crystals and 2 inch Hamamatsu R4275-02 PMTs were used for the others. These PMTs were directly attached to the crystals.

Sandwich module

In order to fill gaps between the CsI crystals and the support structure, we used 24 lead / scintillator sampling counters(Sandwich module). The Sandwich modules consisted of alternating layers of 1 mm thick lead and 5 mm thick plastic-scintillator plates. As shown in Figure 3.9, there were three different types: type-A, type-B and type-C, according to the number of layers. The scintillation light due to the electromagnetic shower in the Sandwich module was absorbed by wavelength-shifting (WLS) fibers, which were 1mm in diameter with a multi-cladding(KURARAY Y-11). They were glued to grooves on the surface of the scintillator plate. The light from the WLS fiber was detected by a $1\frac{1}{8}$ inch Hamamatsu H1398 PMT. The other end of the fiber was polished and treated with an aluminum coating. Typical light yield was 10–20 photoelectrons per MeV energy deposition.

Type-A   Type-B   Type-C
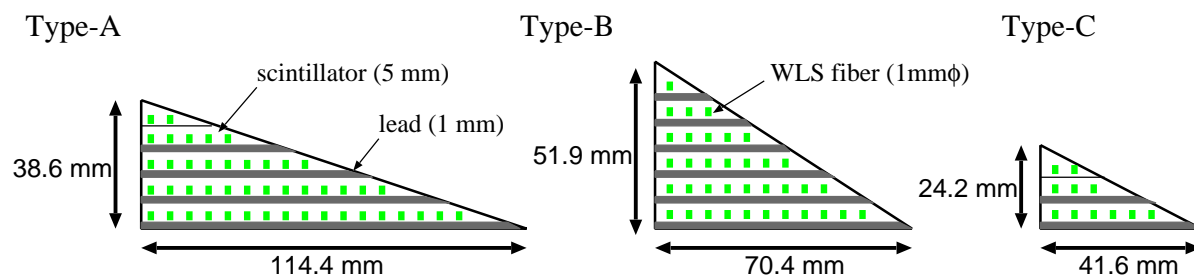
Figure 3.9: Sandwich modules.
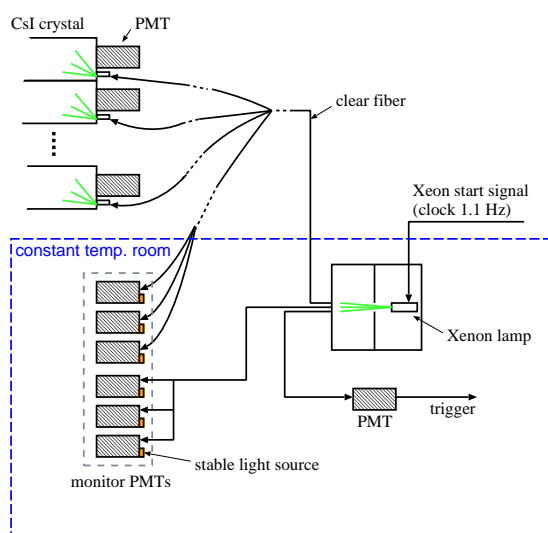
Figure 3.10: Schematic view of the Xenon gain monitoring system.

Xenon Gain Monitoring System

Figure 3.10 shows a schematic view of the calibration system to monitor the stability of the PMT gain. A Xenon lamp flashing at 1.1 Hz was located in the temperature-controlled box. The light from the Xenon lamp was distributed into each PMT through a clear fibers. There were seven PMTs in the same box. One of them was used for triggering, and three of them were used to monitor the light yield of the Xenon lamp distributed to the CsI crystals. Other three PMTs were used to monitor the light yield of the Xenon lamp itself by directly connecting clear fibers from the lamp to the PMTs. We checked the stability of each PMT with a stable light source attached on the front surface of each PMT.

Figure 3.11 shows the average gain of a CsI PMT as a function of operation days. The fluctuation of the gain was found to be within about $\pm 3\%$.

Performance of the Electromagnetic Calorimeter

Prior to the E391a experiment, we evaluated the energy resolution of the calorimeter. A part of the E391a calorimeter, a 5×5 array of Normal CsI crystals, were tested by using a positron beam in the energy range from 0.5 to 3 GeV. Figure 3.12 shows the result of the energy resolution as a function of
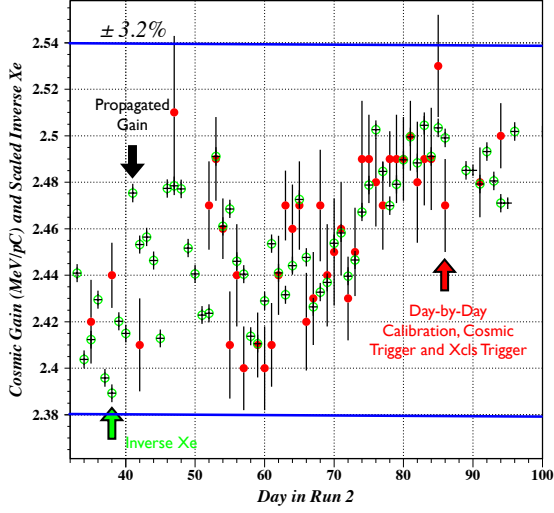
Figure 3.11: Gain stability of CsI's PMT as a function of the operation days. Red dots show the gain factor calibrated by the cosmic-ray data. Green open circles show the gain factor corrected by the Xe system.
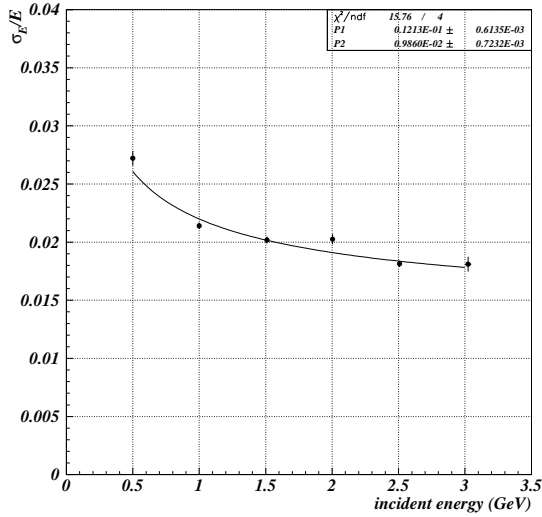
Figure 3.12: Energy resolution as a function of the incident energy as measured with a positron beam with 5×5 Normal CsI crystals. The function is represented as $\sigma_E/E = P1/\sqrt{(E)} + P2$.

the incident energy E by the measurement. We obtained the energy resolution:

$$\frac{\sigma_E}{E(\text{GeV})} \simeq \frac{1\%}{\sqrt{E(\text{GeV})}} \oplus 1\% \,, \tag{3.1}$$

where $\oplus$ denotes addition in quadrature.

We continually monitored and calibrated the energy scale factor using cosmic ray muons and minimum ionization particles from the beam during the operation [42, 43]. We also studied the energy scale factor by using the data as described in Chapter 6.
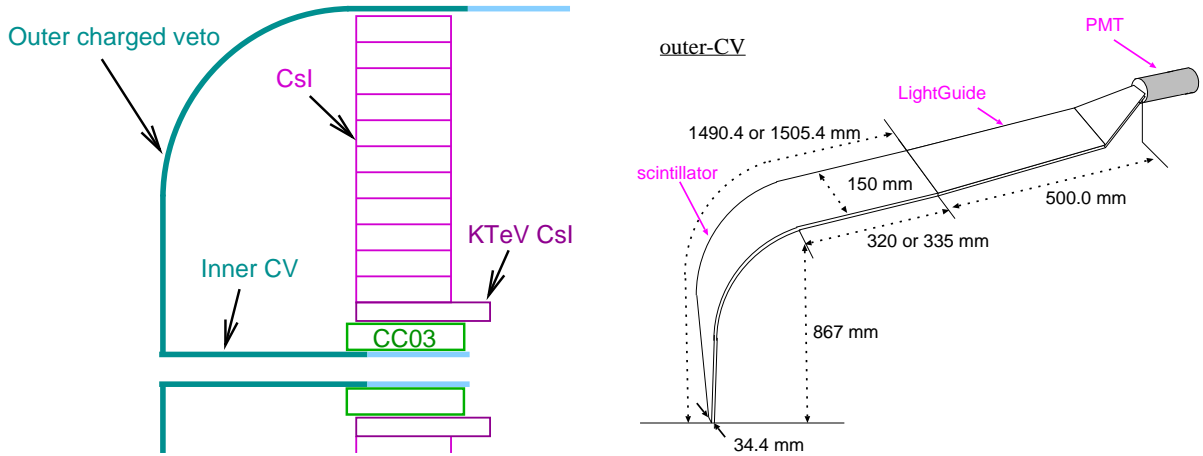
Figure 3.13: (Left) Schematic drawings of CV; (Right) structure of the outer CV.
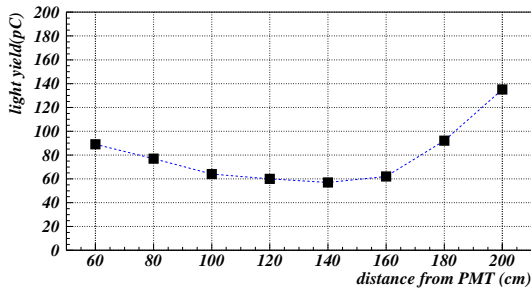
Figure 3.14: Light yield of the outer CV as a function of the distance from the PMT [44]. The yield is indicated by the collected charge.

3.2.2 Charged Veto

Main K_L^0 decay modes such as $K_L^0 \rightarrow \pi^\pm e^\mp \nu$, $K_L^0 \rightarrow \pi^\pm \mu^\mp \nu$ and $K_L^0 \rightarrow \pi^+ \pi^- \pi^0$ have at least two charged particles in the final states. In order to remove these decays, we installed the "Charged Veto" (CV) detector in front of the CsI calorimeter.

CV was categorized into the outer CV and the inner CV as shown in Figure 3.13. The outer CV consisted of 32 plastic scintillator plates with their thickness of 6 mm. They were placed 50 cm upstream from the CsI surface. At the outside of the calorimeter, they were bent and extended to the PMTs for readout. The inner CV consisted of 4 plastic scintillator plates with a thickness of 6 mm. They were aligned parallel to the beam axis, covering the beam region. We used 2 inch Hamamatsu R329 PMT for all the CV counters.

Figure 3.14 shows the light yield as a function of the distance from the PMT, which was measured with a β source [44]. The light yield increases at the far end, due to the scintillator's wedge-like shape.

3.2.3 Main Barrel

The Main barrel (MB) detector surrounded the K_L^0 decay region to detect photons from the K_L^0 decay and other interactions. As shown in Figure 3.15, MB was installed on the inner surface of the vacuum

vessel. MB consisted of 32 segments in azimuthal direction. The overall size of MB was 2.76 m in the outer diameter, 2.00 m in the inner diameter, and 5.5 m in the longitudinal length.

The cross section of the module was in a trapezoid shape as shown in Figure 3.16. It consisted of 45 pairs of a 5 mm thick plastic-scintillator plate and a lead sheet. For the innermost 15 layers, the thickness of the lead sheet and the scintillator were 1mm and 5mm, respectively. We called a group of these 15 layers "inner module". For the other 30 layers, called "outer module", each lead sheet was 2 mm in the thickness, Each scintillator plate was wrapped by white reflecting sheets. The total thickness of the module was 317.9 mm which corresponds to $13.5X_0$. These layers were compressed by 52 screw bolts by the 3 mm thick steel plate at the inside and the 28.6 mm thick steel backbone plate at the outside.
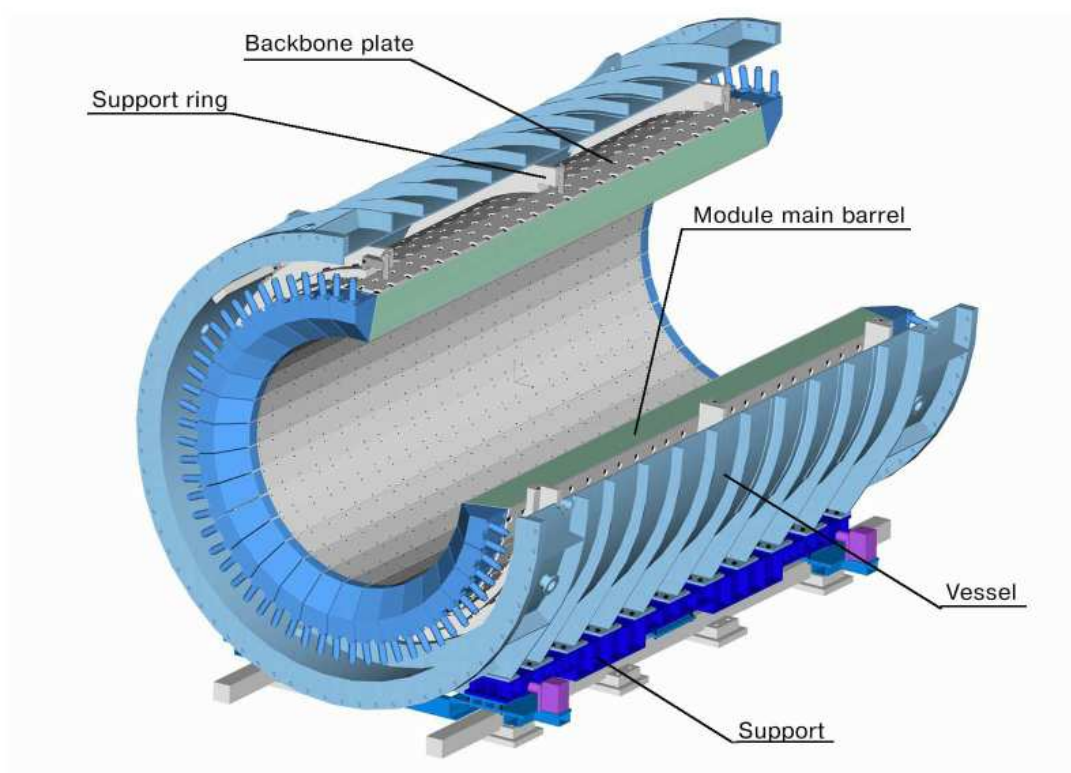
Figure 3.15: Overview of the detectors in the middle section; Main barrel (MB) and Barrel charged veto (BCV) are supported by the vacuum vessel.

Scintillator Plate

The scintillator plates for MB were made of a MS resin (a copolymer of methylmethacrylate and styrene) infused with the fluors PPO(1 %) and POPOP(0.02 %). The reason why we chose the MS resin, instead of usual polystyrene, was to increase the strength of the scintillator plate to sustain its
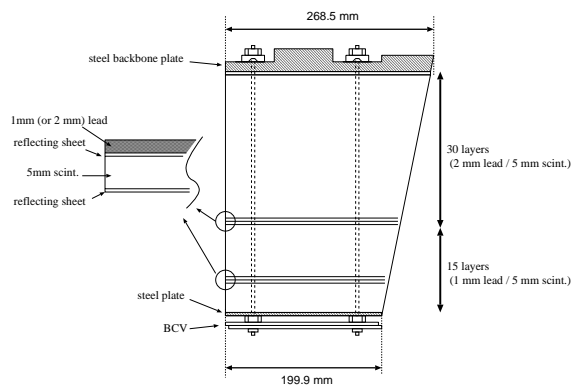
Figure 3.16: Schematic drawing of MB module.

long detector length. The scintillator plate had 1.3 mm-deep grooves at a 10 mm interval to insert wavelength shifting fibers.

Wavelength Shifting Fiber

In order to reduce the attenuation loss of the scintillation light, we used wavelength-shifting(WLS) fibers glued in the grooves of the scintillator plate. The WLS fiber was 1 mm in diameter with a multi-cladding structure(KURARAY Y-11). The scintillation light produced by the electromagnetic shower in the MB module was absorbed by the WLS fibers, which had the absorption peak at $\lambda = 430$ nm and emission peak at $\lambda = 476$ nm. Re-emitted light propagated through the fiber to both upstream and down stream ends.

Connection between Fibers and PMT

The fibers from each module, inner and outer modules, were grouped at the upstream and downstream ends. A PMT was attached on each end of each module. A schematic view of the fiber readout for the MB module is shown in Figure 3.17. The WLS fibers were glued with optical cement (BICRON BC-600) in the acrylic ring, and were cut and polished. The light from the fibers was guided to the PMT through a 3 mm thick silicone cookie and a 10 mm thick light guide.

PMT / Divider

We used the 2 inch Hamamatsu R329-EGP PMT, which we newly developed for the E391a experiment [45]. In order to increase the quantum efficiency for the light from the WLS fiber, we introduced a prism-shape photo-cathode (Figure 3.18) and modified the material of the photo-cathode to be sensitive to green light, i.e. to match the sensitive region with the emission spectrum of the WLS fiber. The R329-EGP PMT was 1.8 times more sensitive to the WLS emission light than a standard PMT.

In order to reduce heat dissipation of the PMT divider and its heat conduction to the PMT in the vacuum, we used the similar technique as used for the PMT of the calorimeter: we connected the divider with a cooling pipe, and used a new PMT divider as described in Section 3.2.1.
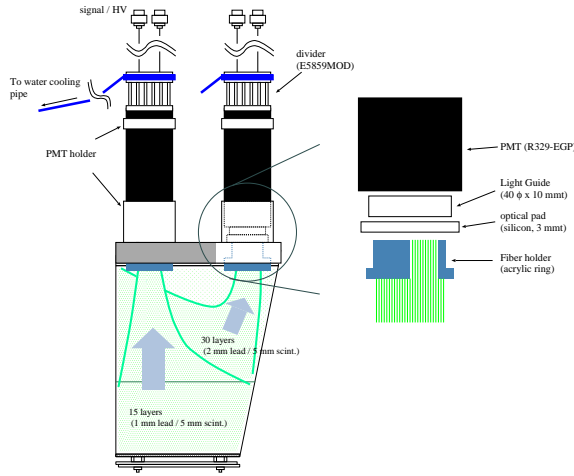
Figure 3.17: Readout scheme of the MB module.
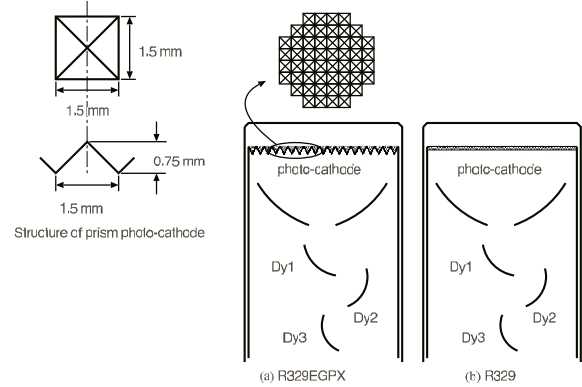
Figure 3.18: A prism-shape photo-cathode (left) and normal photo-cathode (right) [45].

Gain Monitoring System

To check the MB gain stability, we monitored the PMT gain by using an LED calibration system. A blue LED at the outside of the vacuum vessel was flashed with 1.1 Hz, and its light was guided through an acrylic flange and by clear fibers to each PMT.

The gain shift between the on-beam and off-beam periods was found to be less than 1 %.

Performance

The performance of MB was measured using cosmic ray muons. A typical pulse width (FWHM) was 16 nsec [46]. Figure 3.19 shows the light yield of a MB module as a function of the distance between the hit position and the PMT. A typical light yield was 35 (10) photo-electrons per MeV at the nearest (farthest) point from the PMT. As shown in Figure 3.20, the timing resolution was 0.6 nsec for inner module and 0.5 nsec for outer module, respectively.

Barrel Charged Veto

In order to identify charged particles, a plastic scintillator plate was placed in front of the MB segment. Figure 3.21 shows a schematic view of Barrel Charged Veto (BCV) detector. BCV was made of two 5 mm thick scintillator plates glued together with optical cement. Properties of the scintillator plate were the same as used in MB. The total size was 550 cm in the longitudinal length, 1 cm in the total thickness and 20 cm in the width. WLS fibers (KURARY Y-11) were sandwiched by the scintillator plates. The scintillator light was read out by the 1 inch Hamamatsu R7899-EGP PMT, which had a prism photo-cathode optimized for the WLS emission light.
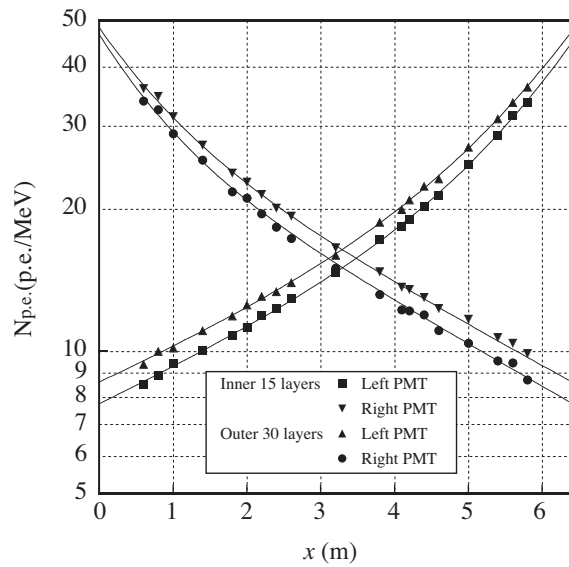
Figure 3.19: Light yield of MB module as a function of the distance from the PMT [46]. Four PMTs were attached on one MB segment.
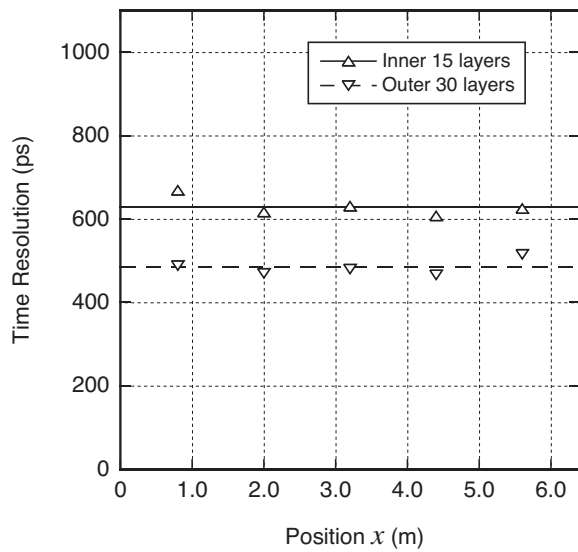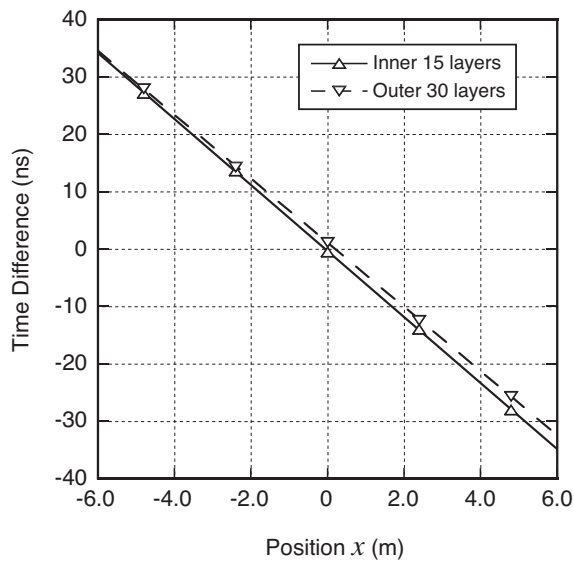
Figure 3.20: Linearity and resolution of timing in a MB module as a function of the distance from the PMT [46].
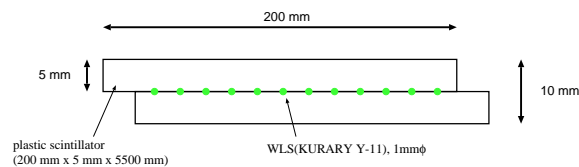
Figure 3.21: Schematic drawing of BCV. The green circles indicate the WLS fibers.

3.2.4 Front Barrel

The front barrel detector (FB) had a similar structure as MB. It surrounded the upstream of the K_L^0 decay region. FB was installed in the upstream part of the vacuum vessel as shown in Figure 3.22. FB consisted of 16 segments in azimuthal direction. The overall size of FB was 1.45 m in the outer diameter, 0.62 m in the inner diameter and 2.75 m in the longitudinal length.

A schematic drawing of the FB module is shown in Figure 3.23. It consisted of 59 pairs of a 5 mm thick scintillator plate and a 1.5 mm thick lead sheet. The total thickness of the module was 413 mm, which corresponds to $17.2X_0$. These layers were compressed by five steel belts (100 μm in thickness) with six screw bolts.

In FB, we used the WLS fibers of 1 mm in diameter with a multi-cladding structure (BICRON BCF-91a). At the upstream end of the fibers, we grouped them into two bundles: the innermost 27 layers and the other 32 layers, and attached the 2 inch PMT (Hamamatsu R329-EGP) to each bundle. The opposite edge of the fibers was covered by an Aluminized mylar to reflect light.

The performance of FB was measured using cosmic ray muons. A typical light yield was 20 (10) photo-electrons per MeV energy deposition with the muon hit at the nearest (farthest) point from the PMT.

3.2.5 Collar Counters

In order to detect photons which passed through just outside the beam region, we placed a series of photon veto detectors perpendicular to the beam axis. They were called "Collar Counters"(CC). There were seven collar counters: CC00, CC02, CC03, CC04, CC05, CC06 and CC07. (There was no CC01 for historical reasons.)

CC00

CC00 was placed in the upstream of the vacuum vessel, and surrounded the beam pipe in order to reduce halo neutrons. CC00 has sandwich structure with 2 cm thick tungsten disks and 5 mm thick scintillator plates. The scintillator plates were divided into the upper and lower parts. Each part was read out from both sides (left and right) by the PMTs through light guides.

CC02

CC02 was located at the downstream end of FB, lining the inner bore of FB, as shown in Figure 3.22. Figure 3.25 is a schematic drawing of CC02. CC02 consisted of 8 modules and formed an octagonal shape. The inner beam hole was 158.4 mm in diameter. To detect photons passing along the beam axis, CC02 had a shashlik structure in which radiators were set perpendicularly to the beam axis. Each module consisted of 43 pairs of a 5 mm thick scintillator plate and a lead sheet. The thicknesses of the lead sheet were 2 mm for the innermost 29 layers and 1 mm for the others. The total radiation length was $15.73X_0$. The whole layers were compressed by 1.5 cm thick aluminum plates.

We used the same WLS fibers as used for FB to read out the scintillation light. The WLS fibers were 2.5 m long, and attached to a PMT through 5 mm thick silicone cookies. We used 2 inch Hamamatsu R329-EGP PMTs.

A typical light yield was 10 photo-electrons per MeV energy deposition.
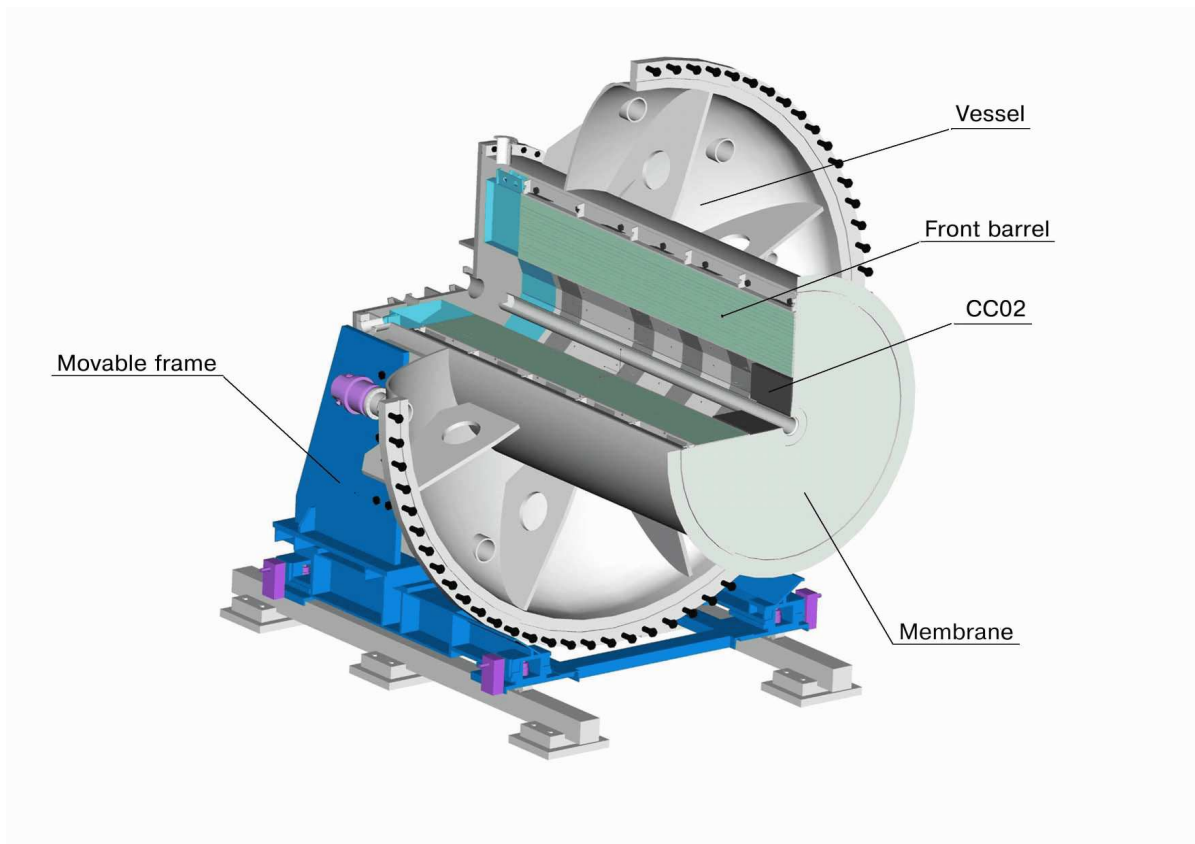
Figure 3.22: Overview of the upstream detectors.
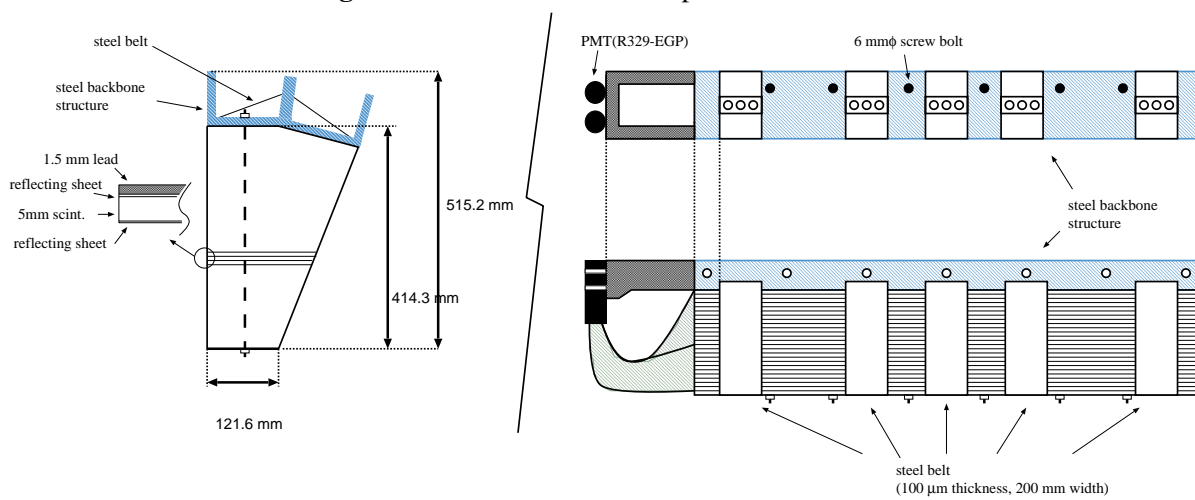
Figure 3.23: FB module, which consists of 59 lead (1.5 mm) and scintillator (5 mm).
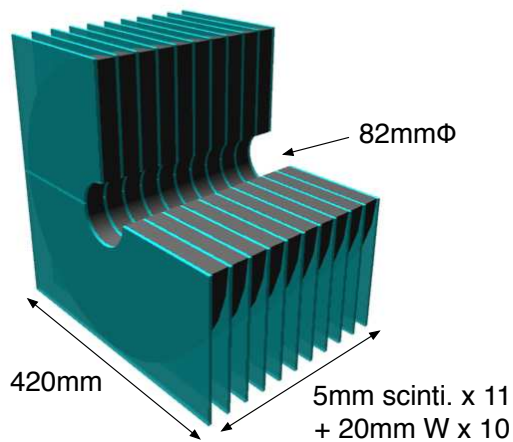
Figure 3.24: Drawing of the inner structure of CC00.
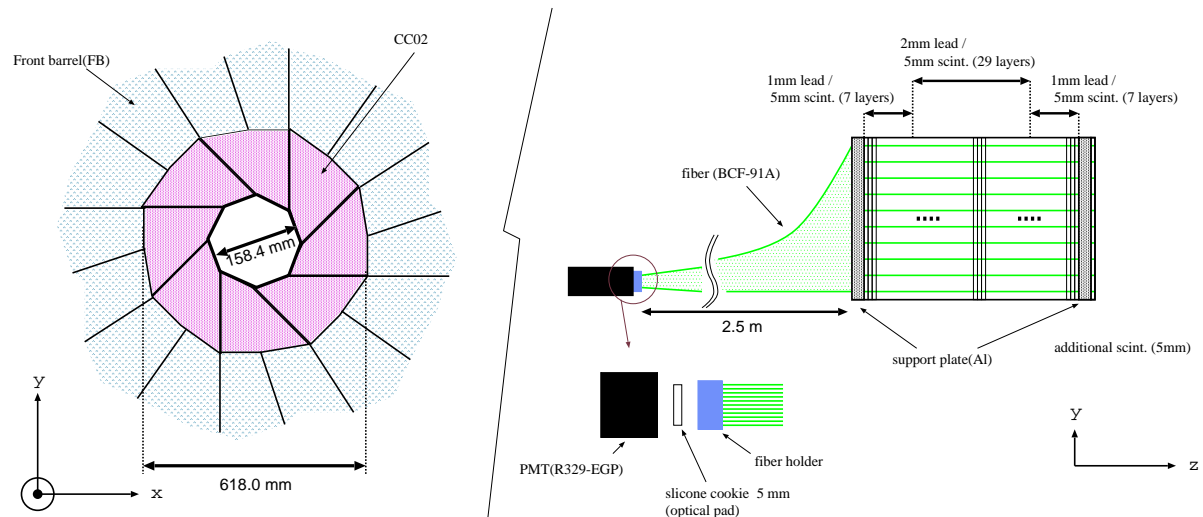
Figure 3.25: (Left) Schematic view of CC02 from the downstream end; (Right) details of the CC02 module.

CC03

CC03 was located at the center of the electromagnetic calorimeter. CC03 detected photons from K_L^0 decays near the electromagnetic calorimeter. The size was 250 mm × 250 mm × 400 mm with a 120 mm × 120 mm beam hole. The detector consisted of six modules. Each module consisted of 26 pairs of a 3.4 mm thick scintillator and a 1 mm thick tungsten plate. The direction of these plates were parallel to the beam axis.

CC04 and CC05

CC04 and CC05 were located at the downstream of the electromagnetic calorimeter in order to detect photons escaping from the decay region. Both CC04 and CC05 were 500 mm $\times$ 500 mm in the cross section with a 126 mm $\times$ 126 mm beam hole.

CC04 consisted of 32 pairs of a 5 mm thick scintillator and a 2 mm thick lead plate. In front of the first lead / scintillator layer, there were two additional scintillator plates with higher PMT gains in order to detect charged particles effectively. The total thickness was $11.4X_0$.

CC05 consisted of 32 pairs of a 5 mm thick scintillator and a 2 mm thick lead plate. There were two additional scintillator plates with higher PMT gains, at the downstream side of CC05, in order to detect charged particles effectively. The total thickness was the same as CC04.

For both detectors, we used WLS fibers to read out the scintillation light. The light from the fibers was viewed b 2 inch PMTs (Hamamatsu H1161).
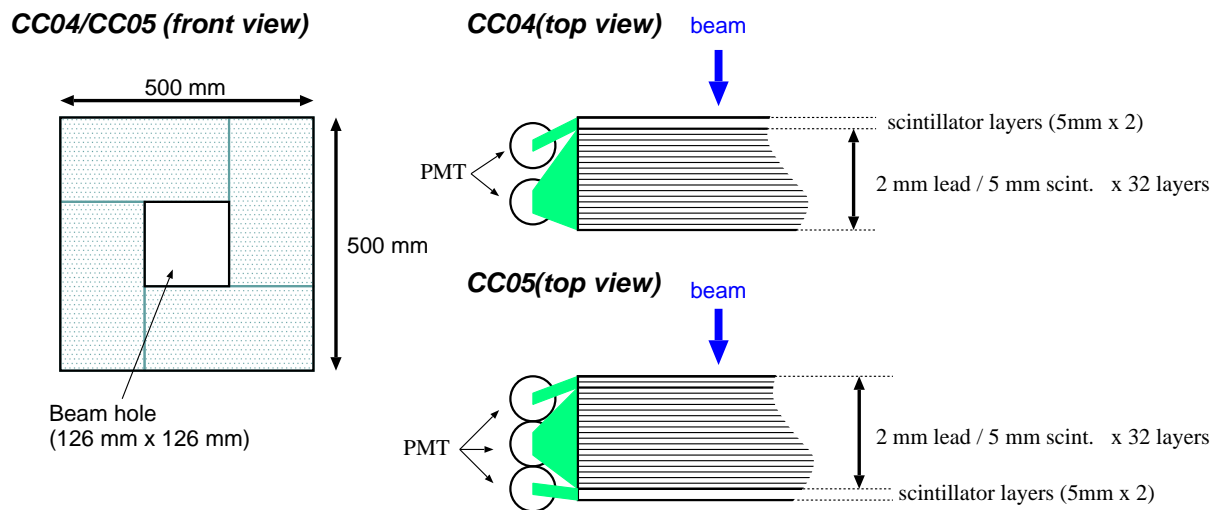
Figure 3.26: Schematic drawing of CC04 and CC05.

CC06 and CC07

CC06 and CC07 were located at the downstream of CC05 and detected photons escaping from the decay region. They had the same structure, and consisted of 10 lead glass blocks as shown in Figure 3.27. The lead glass block was 300 mm $\times$ 150 mm in the cross section and 150 mm long in the beam direction. The chemical composition of the lead glass was 55 % of PbO, 4 % of K_2O, 39 % of SiO_2 and 2 % of Na_2O. The density was 4.08 g/cm^3 and the refractive index was 1.7. The total radiation length was $6.3X_0$. Electrons and positrons in the electromagnetic shower emitted Cherenkov light, and were detected by a 5 inch PMT (Hamamatsu R1250) directly attached to the lead glass with a optical cement.

CC06/CC07 (front view)

Lead glass
(300 mm x 150 mm x 150 mm)

PMT
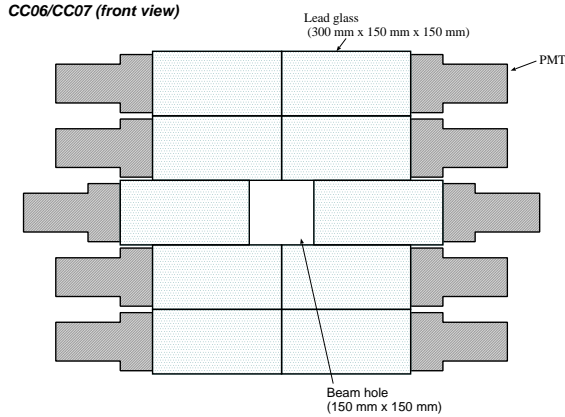
Figure 3.27: Front view of CC06 and CC07.

Beam hole
(150 mm x 150 mm)

3.2.6   Back Anti and Beam Hole Charged Veto

Back Anti

Back anti (BA) was located at the end of the neutral beam. BA covered the beam core region. The purpose of BA was to detect photons going to the beam hole.

Many neutrons in the beam hit BA directly. Mis-identification of neutron signals as electromagnetic showers from photon would lose the acceptance for $K_L^0 \rightarrow \pi^0 \nu \bar{\nu}$. Thus, we should discriminate photons from neutrons in BA. We also had to make BA tolerant to its high counting rate.

In order to satisfy these requirements, BA was designed as shown in Figure 3.28. It consisted of six lead / scintillator modules and six quartz modules. The lead / scintillator module consisted of seven 5mm-thick plastic scintillators and six 2mm-thick lead plate, alternatively. Each quartz module consisted of seven quartz crystals whose dimension was 35 mm $\times$ 245 mm in the cross section and 30 mm thick in the beam direction. The total radiation length was $14 X_0$. Cherenkov light was emitted in the quartz crystals. Since most of secondary charged particles from neutron interactions in BA had the momentum below the Cherenkov threshold with the refractive index of the quartz, 1.46, there should be no signal in the quartz crystals from these particles. On the other hand, secondary particles from both photon and neutron interactions deposited their energy in the scintillator. Thus, we were able to discriminate photons from neutrons by comparing signals in the lead / scintillator layers and in the quartz layers.

Scintillation light in each scintillator plate was transmitted along WLS fibers glued on the scintillator plate. The WLS fiber was 1 mm in diameter and with multi-cladding (KURARY Y-11). The WLS fibers from each plate were viewed by a $1\frac{1}{8}$ inch PMT (Photonis XP 2978). Cherenkov light in each quartz crystal was directly detected by the PMT. We used active PMT dividers (Photonis VD109/T : transistor-based divider) for all the readout channels in BA in order to reduce gain drift due to the high rate. The typical counting rate was 1 MHz per channel. It caused 3 % gain shift between beam on and off periods.

Beam Hole Charged Veto

The purpose of Beam Hole Charged Veto (BHCV) was to detect charged particles escaping from the decay region through the beam hole.
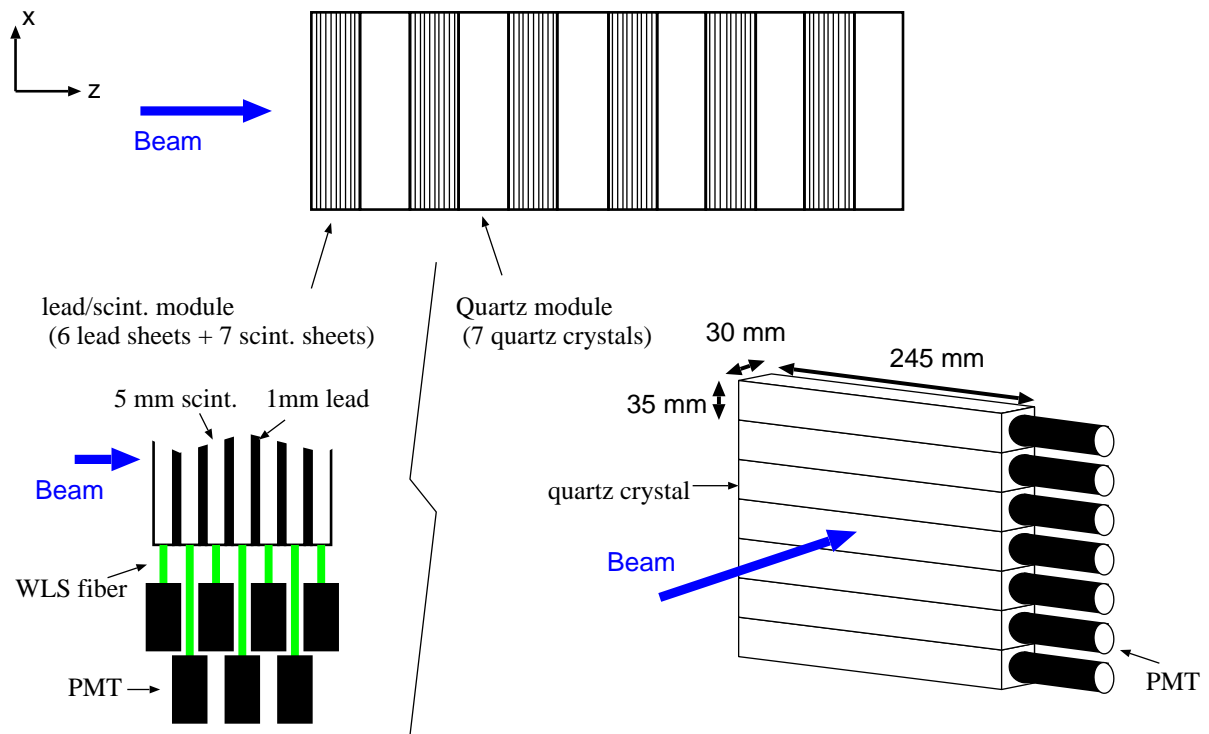
Figure 3.28: Schematic views of Back Anti (BA).

BHCV was located in front of BA in the beam region. It consisted of eight plastic scintillators with their thickness of 3 mm. They were aligned perpendicularly to the beam direction, being overlapped with adjacent plates to eliminate gaps between the plates. The scintillator light was directly detected by the PMTs on both ends. The PMT was EMI 9954B and the PMT divider was an active divider developed by the KTeV experiment.
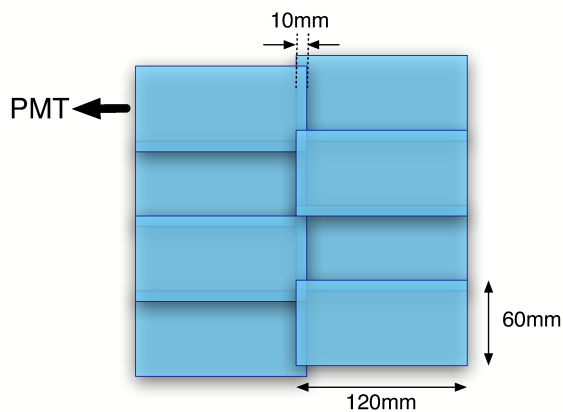
Figure 3.29: Front view of BHCV, They were overlapped by one another with 10 mm width of each edge.

3.3   The Vacuum System

One of the background sources was the neutron interactions with residual gas in the decay region which produced one or more π^0. As described in Chapter 2, we need a high vacuum of 10^{-4} Pa to suppress such backgrounds to be ≤ 0.1 events level[40].

In addition, most of the detector components must be located inside the vacuum to prevent particles from interactions before detection. Our vacuum system was designed to fulfill these requirements.
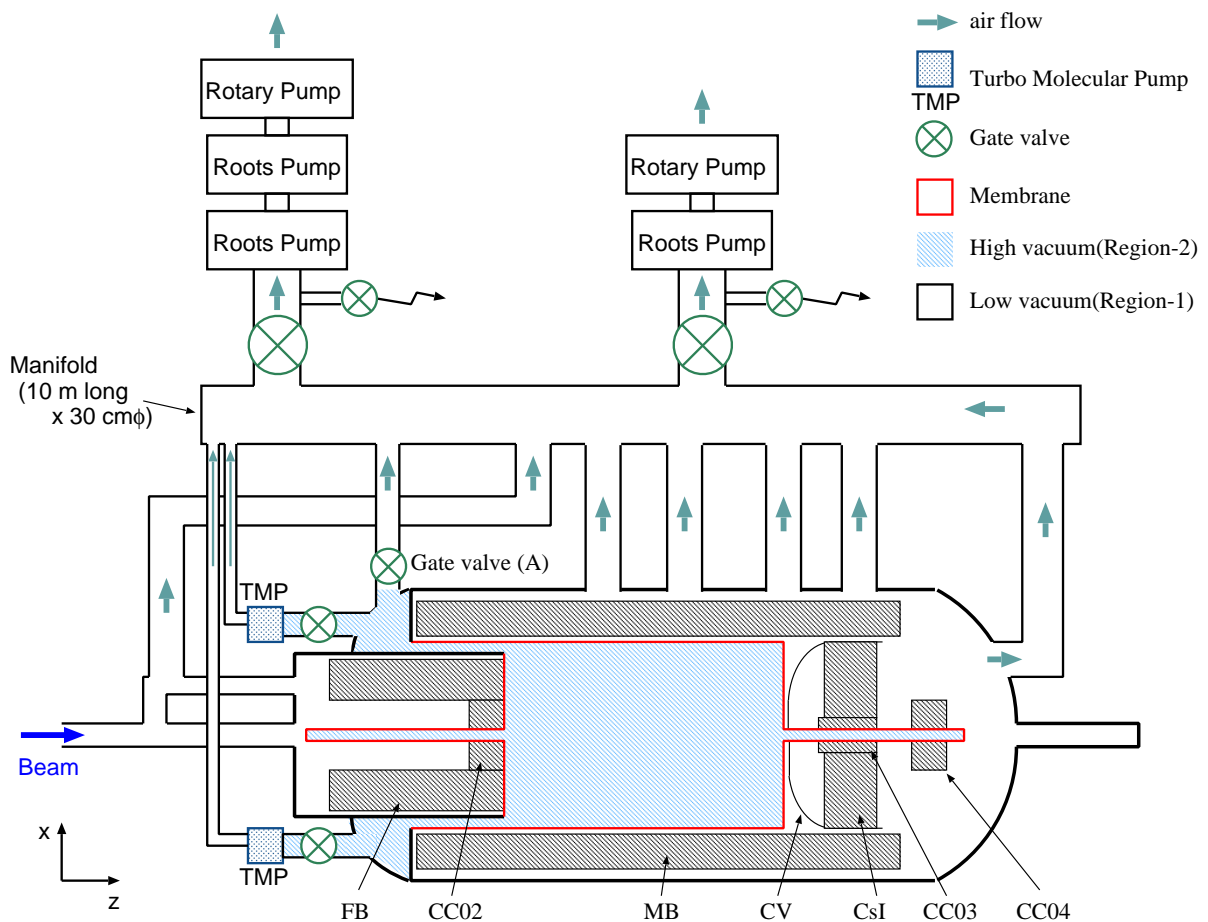
Figure 3.30: E391a vacuum system. Region-2 corresponds to the high vacuum region, and Region-1 corresponds to the region in which all the detector components were located. There are two sets of the rotary pump and the roots pump systems, and four turbo molecular pumps (TMP). First, we turned on the rotary pump and evacuate gas from the whole area down to 10 Pa level. Next we turned on the roots pump. After the pressure reached to 1 Pa, we closed the gate valve (A) in order to separate the low vacuum region and the high vacuum region and then turned on the all TMPs.

Table 3.2: Total volume and surface area for the fiducial region and the outside region as shown in Figure 3.30.

	Volume	Surface area	Pressure in the operation
Region-1(outside region)	100 m^3	220 m^2	0.1 Pa
Region-2(fiducial region)	10 m^3	40 m^2	10^{-5} Pa

3.3.1 Overview

It is difficult to evacuate a gas down to the 10^{-5} Pa level with the detector components inside, due to large amount of out-gassing from detector materials. In order to avoid this problem, we separated the vacuum region into two, and placed the detector components in the "low vacuum" region. Hereafter, we define the "high vacuum" region for the beam as Region-2, and the low vacuum region for the detector components as Region-1.

Figure 3.30 shows the overview of the vacuum system. The total volume and the surface area for both regions are summarized in Table 3.2. We evacuated gas from the Region-1 down to 0.1 Pa and the Region-2 down to 10^{-5} Pa. The pressure difference between two vacuum regions was $\Delta P \simeq 0.1$ Pa.

We used a thin film to separate two vacuum regions. Requirements for the film were:

- it should be as thin as possible in order to avoid absorption of photons and charged particles, and

- it should be made of low out-gassing material in order to achieve 10^{-5} Pa in the high vacuum region.

To satisfy these requirements, we used a multi-structure film. Figure 3.31 shows a schematic drawing of the film, which is usually used for blimps. We call this film as "membrane". The total thickness was 190 μm which corresponds to 4×10^{-4} X_0. The membrane consisted of 4 layers; a low-density polyethylene with thickness of 80 μm, an Aluminized EVAL film with thickness of 15 μm, a nylon film with thickness of 15 μm and a low-density polyethylene with a thickness of 80 μm.

We fixed the membrane to the inner surface of the detectors surrounding the decay region using a support structure, which was a combination of aluminum pipes.

3.3.2 Pumping System and its Performance

Two sets of the rotary pump and the roots pump system were used to evacuate gas to the 0.1 Pa level. They were attached to a large manifold (10 m long, 30 cm in diameter). The manifold was connected to the vacuum vessel with eight pipes (10 cm in diameter). Throughput of the roots pump was 0.27 m^3/s. For the high vacuum, we used four turbo molecular pumps (TMPs), which were able to evacuate gas down to a high vacuum (10^{-2} to 10^{-6} Pa level). Operation of the TMPs should start from at least 1 Pa level. Throughput was 3200 m^3/s using all the TMPs.

It took a half day to reach 10^{-4} Pa and two weeks to reach 10^{-5} Pa.

3.3.3 Operation of the PMT in the Vacuum

Since PMTs were operated in the vacuum, it was impossible to air-cool the PMT bases. This was a serious problem for the CsI calorimeter since the light yield of the crystal has a temperature dependence

Low density
Polyethylene (80μm)
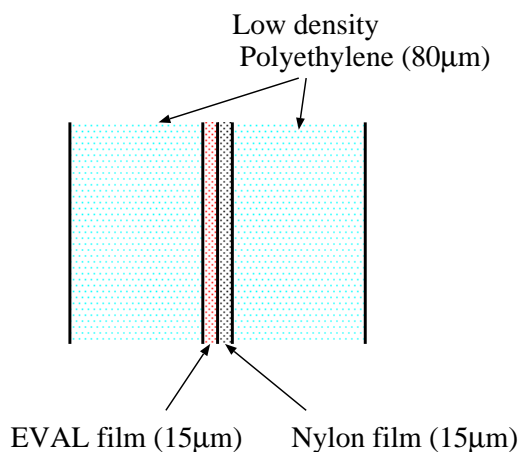
Figure 3.31: Cross section of the film, "Membrane", used to separate the high vacuum region and the low vacuum region.

EVAL film (15μm)   Nylon film (15μm)

of $-1.3\%/^\circ$C. In order to cool the bases, we installed a water cooling system. Cold water with a temperature of 10 $^\circ$C flowed in a copper pipe behind the CsI crystals. Heat conducting cables, made of copper, were attached between the PMT dividers and the copper pipe. The temperature of the CsI crystal and the PMT divider was approximately 20°C during the operation. We also used the water cooling for FB, MB and BCV.

Figure 3.32 shows the discharge voltage as a function of the vacuum pressure. In order to avoid the discharge, we tuned the HV after the pressure was down to 1 Pa.
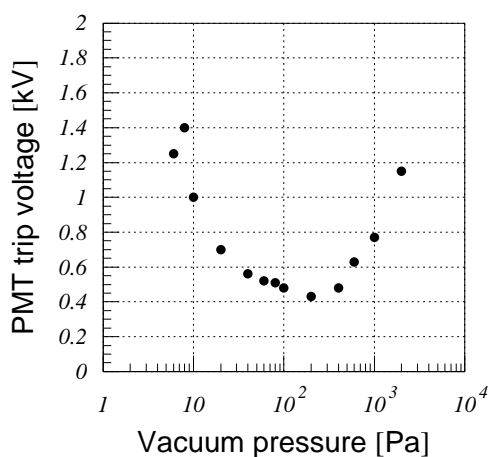
Figure 3.32: Discharge voltage as a function of the vacuum pressure. Typical HV value in the actual operation was 1.0 kV – 1.6 kV.

3.4 Trigger

A hardware-based single-level trigger system was employed in E391a. There were several trigger conditions for specific purposes.

3.4.1 Physics Trigger

As mentioned in Section 2.3, the signal for the $K_L^0 \to \pi^0 \nu \bar{\nu}$ decay is two photons from a π^0 decay and no other particles detected in the final state. For the physics trigger, we counted the number of electromagnetic shower in the CsI calorimeter using "Hardware cluster counter" (HCC), and rejected events with extra particles by requiring no energy deposition in CV and several photon veto detectors.

AmpDiscri (AD) module

We developed a new module, "AmpDiscri (AD)" with the help of the KEK Electronics Online Group. It was a NIM module for multi purposes used in the front-end system. This module was used for the readout of all the detector components. The purposes of the AD module were:

- to make an analog-sum of the PMT signals to be used in the trigger decision, and

- to discriminate PMT signals with a low threshold to make the input signals for the time-to-digital converter (TDC) with less electronic noise.

The AD module had 8×2 inputs. And the AD module provided:

1. analog output for each PMT signal (called "through"),

2. two outputs of the analog sum of the 8 PMT signals, and

3. discriminated pulses in the ECL level for each PMT signal.

The analog outputs were used to measure the charge of the PMT signals by the analog-to-digital converter (ADC), and the discriminated pulses were used to measure their timing by TDC. In order to avoid electronic noises during the signal transfer, we placed the AD modules right behind the detector system. We applied 0.4 mV threshold to make the signal for TDCs.

The analog-sum signals were used for the "Hardware cluster counter" of the calorimeter and for vetoes in the other detectors.

Hardware cluster counter

We made a hardware cluster counter (HCC) in order to count the number of electromagnetic showers in the CsI calorimeter. We grouped eight neighboring CsI crystals and made 72 regions in total, as shown in Figure 3.33. The analog sum of signals from each region was formed by the AD module. We counted the number of regions whose analog sum exceeded 40 mV, which corresponded to approximately 80 MeV energy deposited in the CsI calorimeter, and defined the number as N_{HC}.

Figure 3.34 shows the distribution of N_{HC} from the real data. Since there were many events with $N_{HC} = 1$ due to beam associated events, we required $N_{HC} \geq 2$ in the trigger.
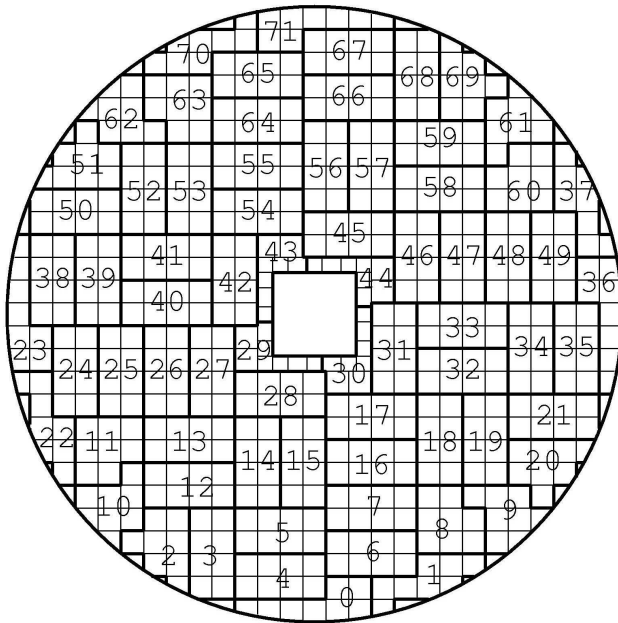
Figure 3.33: Schematic view of CsI crystals with 72 regions for the Hardware cluster counter.
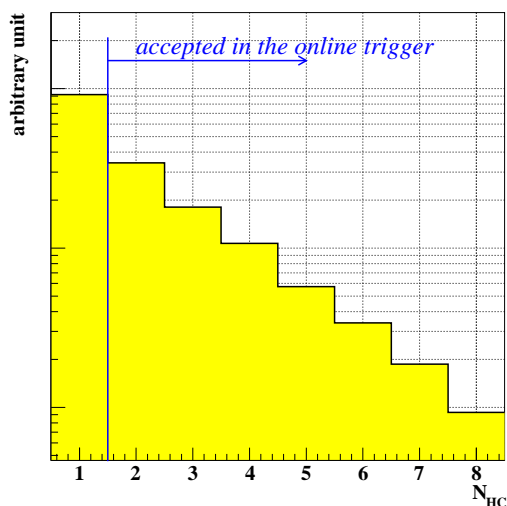
Figure 3.34: Distribution of the number of the hardware clusters from the real data.

Requirements of the Physics trigger

To select events with two photons and no other particles detected in the final state, we required energy deposition in CV and other photon veto detectors to be less than the thresholds that are summarized in Table 3.3.

The K_L^0 decay rate in the decay region was approximately 1.6×10^5 events per 2 second spill with typical intensity of 2.6×10^{12} protons on the target. After the requirements described above, the trigger rate was reduced to 300 events per 2 second spill.

Table 3.3: Requirements for CV and photon veto detectors. E_{cls} is a summed energy in each eight channel in the detector. E_{tot} is the total energy deposition in the detector. For MB, the energy at the trigger stage was measured in the upstream end.

Detector	Requirement	Detector	Requirement
CV	$E_{cls} \leq 1.2\text{MeV}$	MB	$E_{tot} \leq 20\text{MeV}$
FB	$E_{cls} \leq 25\text{MeV}$	CC02	$E_{tot} \leq 15\text{MeV}$
CC03	$E_{tot} \leq 15\text{MeV}$	CC04	$E_{tot} \leq 40\text{MeV}$
CC05	$E_{tot} \leq 25\text{MeV}$		

3.4.2 Other Triggers

In addition to the physics trigger, there were following triggers.

- Calibration triggers :
  Xenon trigger was used to flash the Xenon lamp with a 1.1 Hz clock for monitoring the CsI calorimeter, as described in Section 3.2.1. LED trigger was used to flash the LED with a 1.1 Hz clock, for monitoring MB as described in Section 3.2.3. The frequency of 1.1 Hz was chosen not to synchronize with the spill. Cosmic trigger and Muon trigger collected muons passing through the detector vertically and horizontally, respectively, to calibrate each detector system.

- Minimum bias triggers :
  In order to check the performance of the physics trigger, we formed a set of triggers with relaxed conditions with prescaling. One was the trigger requiring $N_{\text{HC}} \geq 1$ without any vetoes. Another was the trigger requiring $N_{\text{HC}} \geq 2$ without any vetoes.

- Accidental trigger :
  In order to collect events to monitor the detector's accidental activities, the accidental trigger was prepared. Since the accidental activities depended on the beam intensity, we used a signal from the counter which was located nearby the production target.

3.5 Data Acquisition System

The data acquisition (DAQ) system in the E391a experiment was built to collect data with high efficiencies. Figure 3.35 shows the overview of the E391a DAQ system. The total number of detector channels was approximately 1000. Energy and timing information of each detector were recorded every event.

We used a network distributed system with multiple CPUs. Three CPUs were used to read out two Fastbus-VME systems and a TKO-VME system. The dead time of the DAQ system was 600 μs/event, which was dominated by the processing time of the Fastbus-VME. It corresponded to 91 % live time with 300 triggers per spill ($\sim$ 150 Hz). The typical data size was 3 MByte/spill.

3.5.1 Details of the E391a DAQ

The E391a DAQ system consisted of two Fastbus-VME systems, one TKO-VME system and one Linux PC for the event-building. In addition, there were several Linux PCs for online monitoring, an environment monitor, and HV control. All the CPUs and the PCs were connected each other through the GbE network.

The energy information (analog signal) from each detector was transmitted from the AD module to the 1885F ADC through a 90 m coaxial cable. For BA and BHCV, the timing information (ECL signal) was transmitted from the AD module to the 1877 MTDC through a 30 m twist-pair cable. The 1885F and 1877 modules were mounted in two Fastbus crates. We used two sets of a Fastbus-VME interface (SIS4100 NGF) and a VME CPU (FORCE54 UltraSPARCH 500 MHz boards). After waiting for the 1885F conversion time of 256 μs which was started by the gate signal with the width of 200 nsec, the event sequence signal started the data transfer from the 1885F and the 1877 to NGF's FIFO buffer (2 kByte) in the DMA block transfer mode. The data in the FIFO was moved to the CPU's memory every
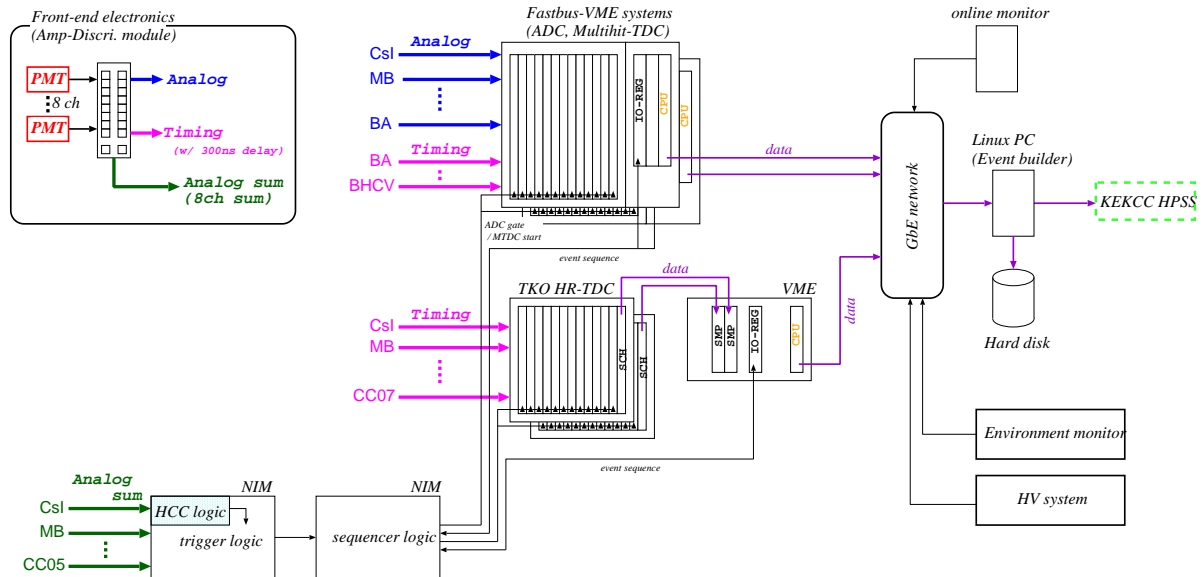
Figure 3.35: Schematic view of the E391a DAQ system.

event. The data in the CPU's memory was transferred to the Linux PC for the event-building every spill. Total processing time was 600 μs per event.

The timing information except for BA and BHCV was transmitted from the AD module to the TKO HR-TDC through a 30 m twist-pair cable. The data of the HR-TDC was read out by the TKO-VME system. It consisted of two TKO-SCH controllers and one VME CPU. The HR-TDC was operated in the common-start mode, and its full range was 200 ns. After waiting for the HR-TDC conversion time of 100 μs, the event sequence signal started the data transfer. The TKO-SCH module controlled the data transfer from the HR-TDC to the VME memory module (SMP) every event. The data in the SMP was transferred to the Linux PC for the event-building every spill. Total processing time per event was 500 μs.

In order to confirm that data in the three buffers belonged to the same event, we sent 8 bit event ID to each buffer.

The data from the Fastbus-VME and the TKO-VME systems were combined and written in the local Hard-Disk-Drive(HDD). The data in the local HDD was transferred to large storage system in the KEK Computing Center (HPSS system) through the KEK Giga-bit network. Typical data size per day was 60 GByte. The consistency of the combined data was checked at the beginning of the offline analysis.

Chapter 4

Data Taking

We have carried out three run periods for data taking. In this chapter, the information of each run and the running conditions are summarized.

4.1   Run Periods

The first data taking (Run-I) was carried out from February 2004 to June 2004. At that time, there was a serious problem that the membrane happened to droop in the beam at CV, and became the source of neutron interaction events. It caused a large acceptance loss in the analysis to reduce the backgrounds [35].

In Run-II, carried out from February 2005 to April 2005, the problem of the membrane was fixed, and several upgrades were made to the electronics.

Another important modification in Run-II was the installation of a beryllium(Be) absorber in the neutral beam line, as shown in Figure 3.2. The interaction length of Be for neutrons was shorter than the radiation length for photons, and the neutrons in the beam line were effectively reduced. The Be absorber reduced the number of K_L^0 in the same time, however the ratio of the interaction length is $\lambda_I(K)/\lambda_I(n) \sim 1.7$, and better K_L^0-to-neutron ratio can be expected. In this thesis, we used the whole data collected in Run-II.

Run-III was carried out from October 2005 to December 2005. In Run-III, sampling-calorimeter part of BA was replaced by PWO crystal, and a photon counter with a lead plate and aerogel was installed in front of BA, which could act as a photon tagging counter.

Each run period, its statistics, and other conditions are summarized in Table 4.1.

4.2   Physics Run

In the physics run, the physics trigger and calibration triggers with pre-scaling, as described in Section 3.4, were active in the data taking. With the typical proton intensity of 2.6×10^{12}, the Be and Pb absorbers, and the HCC threshold at 40 mV (80 MeV), the trigger rate was 300 events per spill.

We monitored the number of reconstructed $K_L^0 \rightarrow \pi^0\pi^0\pi^0$ events every spill during the physics run. This number depended on the proton intensity, the detector stability, etc.. Hence, we were able to monitor data quality at the online stage. The beam profile and the trigger quality were also monitored during the data taking.

Table 4.1: Summary of the run periods.

Run-I	Period	Feb. 2004 to Jun. 2004
	Total protons	2.1×10^{18}
	Remarks	Membrane problem
Run-II	Period	Feb. 2005 to Apr. 2005
	Total protons	1.4×10^{18}
	Remarks	Be absorber
Run-III	Period	Oct. 2005 to Dec. 2005
	Total protons	1.2×10^{18}
	Remarks	New BA,
		Additional photon counter

4.3   Al plate Run

An aluminum(Al) plate with a thickness of 5 mm and a diameter of 10.6 cm was inserted in the beam at 6.5 cm behind CC02 ($z = 281.5$ cm) as shown in Figure 4.1, in order to intentionally produce π^0 and η by neutrons in the beam.

The primary purpose of the Al plate run was to check the calibration of the electromagnetic calorimeter. Since the vertex position of π^0 was known (at the Al plate), it was possible to reconstruct the invariant mass of the two photons. By comparing the reconstructed mass with the π^0 and η masses, we could calibrate the energy scale of the calorimeters.

The data taken in the Al plate run was also used to estimate the background from π^0's produced in the CC02, and to evaluate the cross section of the η production by beam neutrons. They will be described in Chapter 9 in detail.

During the Al plate run, the intensity of the primary proton beam was about half of the intensity in the physics run. Thus, Be absorber was taken out in order to increase the beam particles. In order to reduce the low energy contribution by the neutrons and photons produced in the Al plate, the threshold for HCC was raised to 150 mV (300MeV). Other parameters in the physics run and the Al plate run are summarized in Table 4.2.

Table 4.2: Summary of the condition of the data taking.

Parameter	Physics Run	Al plate Run
Typical proton intensity	2.6×10^{12}	1.0×10^{12}
Total protons	1.40×10^{18}	5.57×10^{16}
Beryllium absorber	IN	OUT
Lead absorber	IN	IN
HCC threshold	80 MeV	300 MeV
Physics trigger rate	300 events/spill	550 events/spill
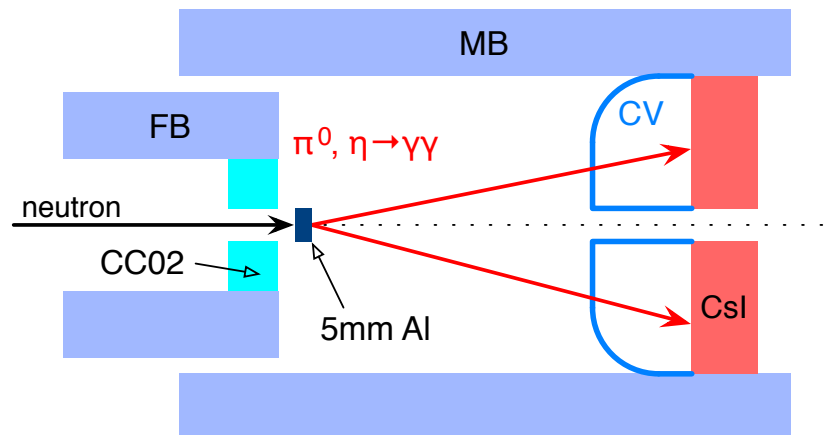
Figure 4.1: Illustration of the Al plate run set-up. The Al plate was located at 6.5 cm downstream of the edge of CC02.

4.4 Calibration Runs

In addition to the physics run and the special runs for the physics analysis, we took data for the detector calibration.

4.4.1 Cosmic Run

When the beam from the accelerator was stopped, the data with the cosmic trigger were taken without the pre-scaling. The gains of the CsI calorimeters were monitored with data taken in the cosmic run.

4.4.2 Muon Run

Muons came from the upstream of the neutral beam line through the collimators and the radiation shield. The muons entered the detector uniformly and almost perpendicularly. When the shutter in the collimator system was closed, neutral particles in the beam were blocked and only the high energy muons could be enhanced; this condition was called "Muon" run. CC00, CC02, CC04–07, outer CV, BHCV, and BA were calibrated by the data with the muon trigger. The Muon run was carried out once per week.

Chapter 5

Monte Carlo Simulation

It is necessary to understand the acceptance ratio of the signal to the normalization modes in order to estimate the single event sensitivity (SES) and measure the branching ratio. The Monte Carlo simulation (MC) was used to calculate the detector acceptance for both signal and normalization modes. In addition, MC was crucial in the background estimation because the acceptance for background sources were also evaluated by using MC. To obtain the detector acceptance for the signal decay, the normalization modes, and background sources, MC simulated the parent particles' production, their decays, and the response of the detector. In MC, the output had the same format as in real data. This allowed us to analyze both real data and MC events in the same framework, with the same algorithm and the same selection criteria (cuts).

In this chapter, our techniques of MC is explained. First, the production of parent K_L^0's and neutrons is described in Section 5.1. Specific methods to generate K_L^0's and the halo neutrons are described in Section 5.2 and Section 5.3, respectively. Section 5.3.1 describes the special method of η production. The explanation of the simulation of detector responses follows in Section 5.4, and finally, Section 8.1.3 presents how the effect of accidental activities was included in MC.

5.1 Beam Line Simulation

We separated the MC scheme into several stages in order to save computing time. The first stage was the production of the particles at the target. The primary protons with the 12 GeV kinetic energy were generated to hit the platinum target, and all the particles produced in the target were collected.

In the second stage, the performance of the neutral beam line was simulated. The collimator C1 through C6 and the Pb and Be absorbers were implemented in the simulation according to their real positions. The particles collected in the first stage were transported to the collimator system, and the particles at the exit of C6 (Figure 3.2) were collected for the next stage. The stages up to the exit of the collimators are called "Beam line simulation" [40, 41]. The GEANT3 package [47] was employed and the GFLUKA code therein was used for the hadronic interactions in the beam line simulation of E391a.

The profiles of K_L^0's and neutrons were measured at the exit of C6. The momentum distribution of the K_L^0 beam is shown in Section 3.1.2 in Figure 3.4. Figure 5.1 shows the distribution of the beam density and the momentum at C6 for the core and halo neutrons. Here the definition of the "halo"

neutrons is the neutrons which ran off the beam hole when extrapolated to the CC05 position. The ratio of the halo to the core neutrons was obtained to be about 10^{-4}, as shown in Figure 3.3. The information of the momentum, position, and direction for K_L^0's and halo neutrons collected in the beam line simulation were used for the detector simulation, as described in Section 5.3

Statistics of the beam line simulation corresponded to 4×10^{11} of the primary protons on the target (POT).
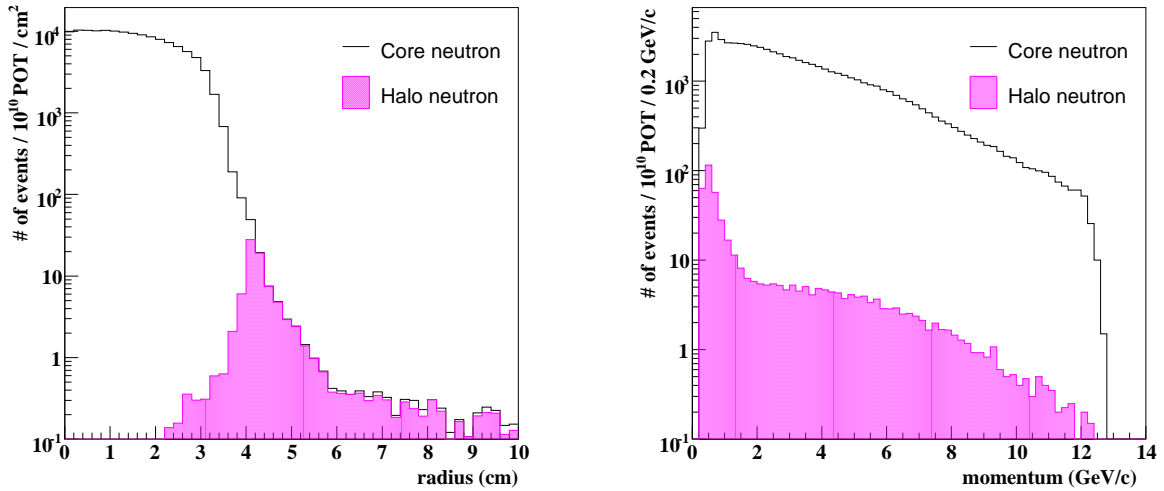
Figure 5.1: Distributions of the beam density (left) and the momentum (right) for the core and halo neutrons at the exit of C6 with their momentum above 0.3 GeV/c.

5.2 K_L^0 **Generation**

The third stage of the simulation was the step in which all the interactions in the detector system were treated. From here, explanations of K_L^0 generation, neutron generation, and detector response are described in each section.

5.2.1 **Parameters for the K_L^0 beam**

In the detector simulation, the parameters for the K_L^0 beam were initially set according to the results from the beam line simulation. The parameters were iteratively tuned to reproduce the distributions with data. The tuning will be described in Section 8.1.2.

Momentum

The momentum (p) distribution was fitted by a function,

$$\frac{dN}{dp} = N_0 \exp\left(-\frac{(p-\mu)^2}{2\sigma^2}\right) ,\tag{5.1}$$

$$\sigma = \sigma_0 \left(1 - (A + S \cdot p)(p - \mu)\right) ,$$

where N_0 is a normalization factor. The description of the other parameters and their values used in MC are summarized in Table 5.1. The momentum distribution produced by this function is shown in Figure 3.4.

Table 5.1: Parameters for the K_L^0 momentum in MC.

parameter	description	value
μ	mean	1.788529
σ_0	dispersion	1.291137
A	asymmetric offset	-0.3290585
S	asymmetric slope	0.0303398

Density

The Radial position of K_L^0's at C6 was approximated by a function:

$$\frac{dN}{dr} \approx \frac{N_0}{1 + \exp((r - x_0)/s)} ,\tag{5.2}$$

where N_0 is a normalization factor, x_0 represents a falling edge, and s determines a slope of the beam shape. Their values are summarized in Table 5.2.

Table 5.2: Parameters for the density of K_L^0 beam at C6 in MC.

parameter	description	value
x_0	edge	1.85893
s	slope	0.20780

Beam Angle

The angle of the beam was defined with the polar (zenith) angle, θ, and the azimuthal angle, ϕ, to the beam axis. Basically, the beam direction could be determined by connecting the radial position at C6 and the target positions. However, the direction has an ambiguity due to the size of the target. In order to include the ambiguity, small fluctuation was added to θ. The ϕ distribution was initially set to be flat from 0 to 2π radian and later tuned with the data, as described in Section 8.1.2.

5.2.2 K_L^0 **Decay**

The K_L^0, produced at the target, traveled until decayed. The decay position was simply determined by K_L^0's proper life time τ and its Lorentz-boost factor. The distribution of the decay vertex (z) with a momentum ($p_{K_L^0}$) is expressed as:

$$f(z) \propto \exp\left(-\frac{z}{\Delta z}\right) , \tag{5.3}$$

where

$$\Delta z = c\tau\beta\gamma = c\tau \times \frac{p_{K_L}[\text{GeV}/c]}{m_{K_L^0}[\text{GeV/c}^2]} . \tag{5.4}$$

At the decay vertex, the parent particle was forced to decay into secondary particles of a specific decay mode. The secondary particles decayed according to their life times and branching ratios which were defined in the GEANT3 package. For $K_L^0 \to \pi^0\nu\bar\nu$, $K_L^0 \to \pi^\pm e^\mp \nu$ and $K_L^0 \to \pi^\pm \mu^\mp \nu$ (K_{l3}) decays, the Dalitz plot distribution was calculated by assuming the V-A interaction.

$K_L^0 \to \pi^0 \nu\bar\nu$ **decay**

The distribution of the π^0 momentum in the $K_L^0 \to \pi^0\nu\bar\nu$ decay was calculated as follows [32, 48]. In the Standard Model calculation substituting the neutrino mass to zero, the differential decay rate can be represented as

$$\frac{d\Gamma}{dE_\pi} \sim \lambda f_+^2 [(m_K^2 - m_\pi^2 - q^2)^2 - \frac{2}{q^2}(\frac{q^2\lambda^2}{3} + 2m_\pi^2 q^4)] , \tag{5.5}$$

where m_K is the mass of the K_L, and E_π and m_π are the energy and the mass of the π^0, respectively, and

$$q^2 \equiv m_K^2 + m_\pi^2 - 2m_K E_\pi , \tag{5.6}$$

$$\lambda \equiv [(m_K^2 + m_\pi^2 - q^2)^2 - 4m_K^2 m_\pi^2]^{1/2} . \tag{5.7}$$

The form factor, f_+, was parameterized as $f_+ = 1 + \lambda_+ q^2/m_\pi^2$ with $\lambda_+ = 0.032$, which was measured by experiments [8]. The kinematic constraint,

$$m_\pi \le E_\pi \le (m_K^2 + m_\pi^2)/2m_K, \tag{5.8}$$

was also required.

Once the π^0's energy was chosen, by following the spectrum expressed in Equation 5.5, its direction was determined isotropically in the K_L rest frame. The π^0 was then boosted in the K_L direction, and immediately decayed into two photons with a branching ratio of 98.8%.

5.3 Neutron Generation

As described in Section 5.1, the neutrons in the beam line were separated into "core" and "halo". The core neutrons were used in the simulation for the Al plate run, and the halo neutrons were used in the estimation of the background in the physics run.
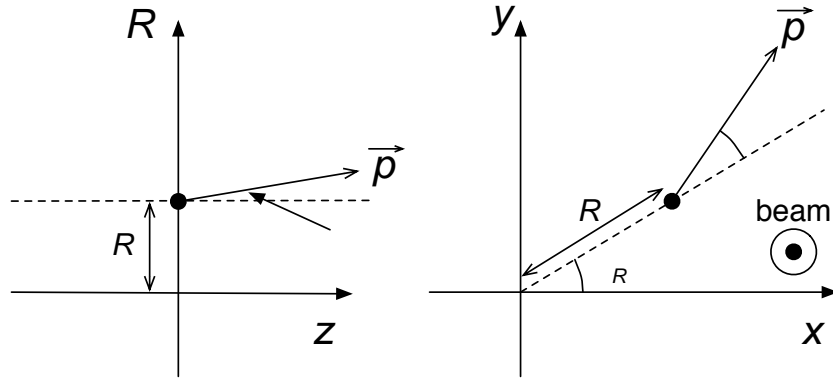
Figure 5.2: Definition of the parameters used in the halo neutron generation.

In generating of neutrons, the parameters of each event collected in the beam line simulation was directly used, instead of the fitting functions as in the case of K_L^0 generation. The particles' position at C6 was represented by (R, ϕ_R). R is the distance from the beam line and ϕ_R is the azimuthal angle with respect to x-coordinate. Also the particles' momentum was represented by $(\theta, \phi_R + \Delta\phi)$. θ is the polar angle, and $\Delta\phi$ is difference of the azimuthal angle from ϕ_R, as shown in Figure 5.2.

Halo neutrons, by definition, could be recognized as the neutrons scattered at least once, or produced in the absorbers and collimators. Thus, the position and momentum direction were expected to have a certain correlation which could not be described by a simple formula. In this situation, we decided to take the method to recycle the collected neutrons, by adding the small fluctuation with the Gaussian distribution. An example of adding the fluctuation for the momentum is:

$$p' = p\left(1 + g(\sigma_p)\right), \tag{5.9}$$

where $g(\sigma)$ is a Gaussian random function with the standard deviation of σ and the mean of 0. We set $\sigma_p = 5\%, \sigma_R = 2\%, \sigma_\theta = 2\%$, and $\sigma_{\Delta\phi} = 0.5\%$. ϕ_R was uniformly distributed in the generation.

5.3.1 η Production

In the simulation of the neutrons, GFLUKA was also used for the hadronic interactions. However, the cross section of the production of η-meson was not implemented in GFLUKA. Thus, we developed the method to simulate η-productions by GEANT4/QBBC [49], and to introduce the result into our standard simulation on the GEANT3 framework.

First, we placed the materials of the detectors around the beam line in the GEANT4 simulation, and produced the particles and collected the information of the events that contain η-mesons. Then, we generated all collected particles in each event in GEANT3 simulation framework. Also, the simulation for the Al plate run was done by this method.

The results of the neutron MC are described in details in Section 9.2.

5.4 Detector Response

We simulated the detector response using GEANT3. The interactions, such as pair production, multiple scattering, etc., were simulated with detector materials according to their cross sections. We traced their interactions until particle's energy became below a cut-off energy. The cut-off energy was set at 0.05 MeV for electrons, positrons and photons, and 0.1 MeV for hadrons and muons. We summed visible energy depositions in the sensitive detector material. The hit "timing" was simulated as the time when the summed energies exceeded the discriminator threshold used in the data taking. The summed energy deposition in each detector channel was defined as the "energy" in the detector except for MB, BCV, CV and BA. For the energy in CsI, we added the special treatment to simulate the energy resolution.

CsI

The energy resolution σ_E/E can be parameterized [8] as

$$\frac{\sigma_E}{E} = a \oplus \frac{b}{\sqrt{E}} \oplus \frac{c}{E}, \tag{5.10}$$

where $\oplus$ represents addition in quadrature and E is in GeV. The constant term a comes from non-uniformity and calibration uncertainty. b is a stochastic term, and c is a noise term, which was known to be negligible in our electronics system. Since the a and b terms could not be reproduced by the interaction in the simulation, we imposed the additional fluctuation, called "smearing", to the energy in CsI, in order to adjust the energy resolution of MC to data.

The parameters for two types of CsI crystals were found to be different due to the difference of their light yields. They are summarized in Table 5.3.

Table 5.3: Parameters for the crystal-by-crystal smearing.

Crystal Type	Constant Term (a)	Stochastic Term (b)
Normal CsI	0.4%	0.8%
KTeV CsI	0.4%	0.6%

MB, BCV

Since the barrel detectors MB and BCV were 5 m long, the attenuation of scintillation light should be taken into account. The scintillation light was transmitted through WLS fibers and detected by PMTs at the end of the fibers. When a particle hit MB or BCV at a distance l from a PMT, the energy measured by the PMT was expressed as

$$E = E_0(a_1 e^{-\frac{l}{\lambda_1}} + a_2 e^{-\frac{l}{\lambda_2}}), \tag{5.11}$$

where E_0 is the energy deposition at the incident position, $\lambda_1(\lambda_2)$ is the attenuation length and $a_1(a_2)$ is a normalization factor for the long (short) term component. The energy to be detected at the PMTs was defined for minimum ionization particles (MIPs) passing through the center of the barrel. It is 15 MeV for the MB inner module, 30 MeV for the MB outer module, and 2 MeV for BCV.

The hit timing of the incident particles at the PMTs was also simulated by taking the light propagation into account. Using cosmic ray muons, we measured the attenuation length and the light propagation speed. They are summarized in Table 5.4.

Table 5.4: Parameters for the attenuation in the barrel detectors [46].

detector	light propagation speed (cm/ns)	λ_l(cm)	λ_s(cm)
MB	17.7 ± 0.1	608.0 ± 56.1	112.5 ± 14.8
BCV	18.2 ± 0.1	481.1 ± 54.5	87.7 ± 23.2

CV

As mentioned in Section 3.2.2, CV had an odd shape; it had a triangle shape at the top, and a 90°-bend at the middle. As a consequence, the relative light yield as a function of the hit position had a non-exponential dependence, as shown in Figure 3.14. We corrected the effective light yield of the outer CV by using the relative light yield as the function of the hit position, as shown in Figure 3.14.

BA

BA consisted of the lead-scintillator and quartz modules as shown in Figure 3.28. Since the quartz is a Cherenkov radiator, the light yield was calculated with β of each particle. The emitted photons was traced within the quartz blocks with the condition of the total reflection and detected at the positions of the PMTs.

5.5   Accidental Activity

Since there were accidental activities in the detectors, those effect had to be added to the simulation.

In the real experiment, the detector had many accidental activities, which were caused by particles coming either from the target or from other reactions. These accidental activities caused additional energy deposition in the detector, and affected the acceptance.

In order to check the effect of the accidental activities, we overlaid the experimental data collected by the accidental trigger on the generated MC events. The energy deposition was simply added together channel by channel. As for the timing information, we took the arrival time of the earliest hit.

Acceptance loss due to the accidental activities was estimated independently, as described in Section 8.1.3.

Chapter 6

Event Reconstruction

In order to identify the signal of the $K_L^0 \to \pi^0 \nu \bar{\nu}$ decay, we searched for the events with a single π^0 decaying to two isolated photons.

The outline of the event reconstruction is:

1. finding energy clusters in the CsI calorimeter,

2. identification of two isolated photons,

3. reconstruction of the π^0 decay vertex by assuming the π^0 mass,

4. correction of the energy and position of the photons according to the reconstructed vertex,

5. iterative reconstruction of the π^0.

6.1 Photon Reconstruction

When a photon hits the CsI calorimeter, it generates an electromagnetic shower and its energy is spread over multiple CsI crystals. Figure 6.1 shows an example of the $K_L^0 \to \pi^0 \pi^0 \pi^0$ decay in which each π^0 decays into two photons, producing six photons hitting the CsI calorimeter.

The task of the photon finding is to reconstruct the electromagnetic showers due to photons from the energy deposition in CsI crystals. It is important to reconstruct all the photons that hit the calorimeter. In particular, we should distinguish two photons hitting close to each other in the calorimeter. Thus, we first attempted to find energy clusters, which are contiguous groups of the CsI crystals with energy deposit exceeding a certain threshold. We then required that each cluster shape should be consistent with a single photon.

6.1.1 Cluster Finding

"Cluster" was defined as a group of neighboring CsI crystals with finite energy deposit. We picked up CsI hits with their energy deposit above 5 MeV and defined them as "seeds". The CsI hits neighboring a cluster seed which shared common edge were grouped as a cluster. An example of forming a cluster is shown in Figure 6.2. The algorithm started with the CsI crystal which had a maximum energy deposit among the seeds. Then we added the seed crystals to the cluster by including every neighbor.
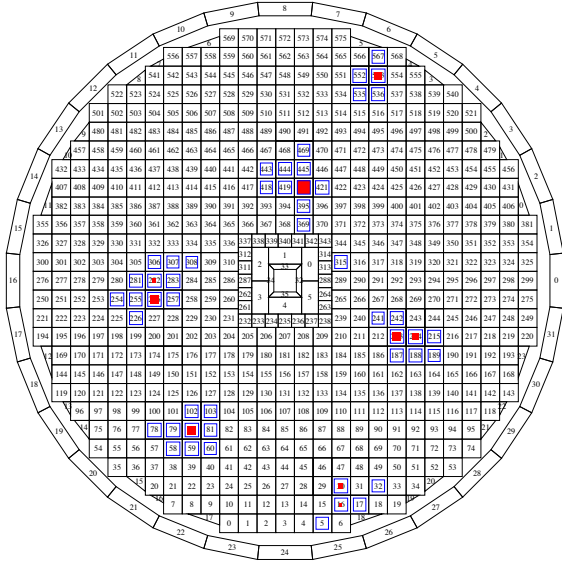
Figure 6.1: Example of the $K_L^0 \to \pi^0\pi^0\pi^0$ decay in which each π^0 decays into two photons, producing six photons hitting the CsI calorimeter. The size of the filled boxes indicates the amount of energy deposition. The boxes with blue lines show the crystals with hits in TDC. Note that the energy threshold for TDC was very low, equivalent to 0.8 MeV.

After the cluster finding, the number of local maxima in each cluster was counted. A local maximum was defined as a crystal whose energy was greater than any of the four neighboring crystals. If a cluster had two or more local maxima, it was identified as a non-isolated cluster.

In this step, we removed events with the non-isolated clusters, because those clusters had a possibility to have more than one photons. On the other hand, even a single photon can produce a cluster with multiple local maxima due to a fluctuation of the electromagnetic shower. This caused the acceptance loss. We found that the acceptance loss was 8 % for the $K_L^0 \to \pi^0\nu\bar{\nu}$ decay by MC studies.

6.1.2   Energy and Position Calculation

The deposited energy of the photon was defined as the sum of energies in the cluster:

$$E_{dep} \equiv \sum_{i=1}^{n} e_i \, , \quad (e_i \geq 5\mathrm{MeV}) \tag{6.1}$$

where e_i is the energy deposit in each crystal and n is the number of crystals in the cluster.

The position of the photon, (x, y), was initially defined by the energy weighted mean, analogous to the center of gravity (COG):

$$x_{COG} = \frac{\sum_{i=1}^{n} x_i e_i}{\sum_{i=1}^{n} e_i} \, , \quad (e_i \geq 5\mathrm{MeV}) \tag{6.2}$$

where x_i is the center position of each CsI crystal in the cluster.

The E_{dep} and x_{COG}, calculated in this stage, apparently deviated from the true energy and position. Due to the leakage of the electromagnetic shower out of the CsI crystals, there can be significant shifts for the visible energy. And, due to the incident angle and the shower propagation of the photons, x_{COG} can be shifted from the real incident position. The corrections for the effects are described in Section 6.3.

(1) sort cluster seeds by the size of the deposit energy in descending order
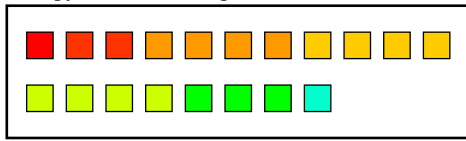
(2) start cluster growth with a first crystal in the cluster seeds, i.e. crystal with max. energy
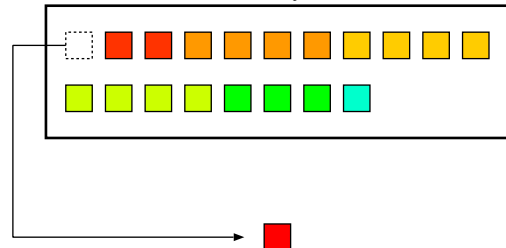
(3) look for neighboring crystals which are sharing an side with the cluster
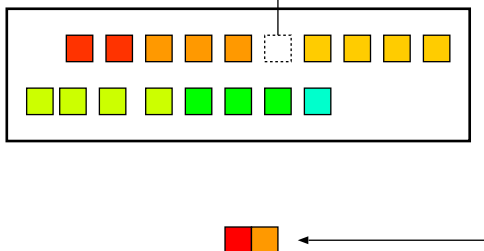
(4) if there are no more neighboring crystals, the cluster growth is stopped
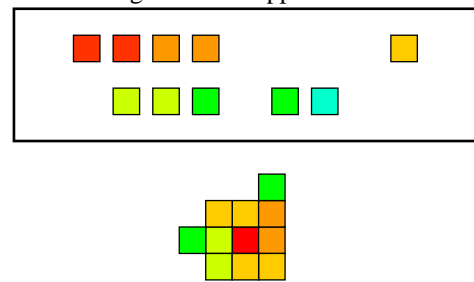
(5) sort cluster seeds again, and start next cluster growth and continue (3) - (4)
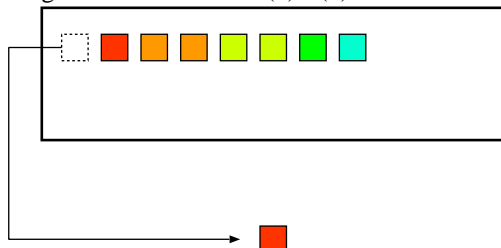
(6) continue the procedures until all cluster seeds are used up.
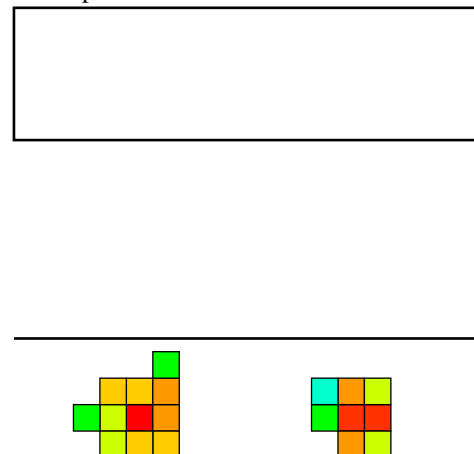
Figure 6.2: Algorithm of the cluster finding in the E391a CsI calorimeter. We stored the cluster seeds by their energy deposit in descending order. The neighboring cluster seeds were grouped to form clusters according to the procedures (2) through (5). The neighboring crystals are defined as the four crystals sharing an edge.

6.1.3 Photon Quality Cuts

The next procedure was to examine the consistency of the cluster with the electromagnetic shower due to a single photon. In order to identify a photon cluster, we used parameters as the number of CsI crystals in the cluster, timing dispersion among them and the energy dispersion of the cluster. Good photon sample, to obtain the proper distributions of parameters, were extracted from the $K_L^0 \rightarrow \pi^0 \pi^0 \pi^0$ decays in the real data. In particular, we required each cluster to have two or more CsI crystals in the photon identification. The cuts for the quality of photons are summarized in Section 7.3.

6.2 π^0 Reconstruction

Once we obtained two photon clusters, we calculated the decay vertex, Z_{vtx}, assuming that the two photons came from a π^0 decay and their invariant mass was equal to the π^0 mass. In this calculation, we also assumed that the vertex is on the z-axis, $(0, 0, Z_{\text{vtx}})$.

Figure 6.3 shows the relation between several parameters used in the calculation. The distance between the vertex and the CsI calorimeter is defined as $dz \equiv Z_{\text{CsI}} - Z_{\text{vtx}}$. There are following geometrical relations:

$$r_{12}^2 = d_1^2 + d_2^2 - 2d_1 d_2 \cos\theta , \tag{6.3}$$

$$d_1 = \sqrt{r_1^2 + (dz)^2} , \text{ and} \tag{6.4}$$

$$d_2 = \sqrt{r_2^2 + (dz)^2} , \tag{6.5}$$

where r_{12} is the distance between the two photons, θ is the angle between the direction of the two photons, d_1 and d_2 are the distances between the decay vertex and the hit positions, r_1 and r_2 are the distances of the hit positions from the z-axis. In addition, assuming that the invariant mass of the two
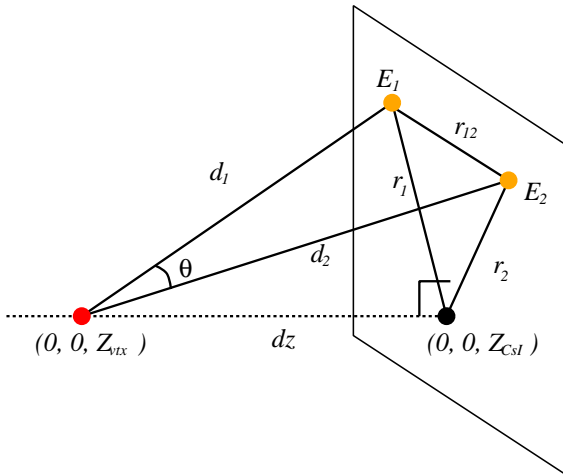
Figure 6.3: Schematic view of parameters used to reconstruct the π^0 vertex.

photons is the π^0 mass(M_{π^0}), we get:

$$\cos\theta = 1 - \frac{M_{\pi^0}^2}{2E_1 E_2} \ ,$$ (6.6)

where E_1 and E_2 are the energies of the photons.

Using these equations, the decay vertex Z_{vtx} was calculated. Also the standard deviation of the decay vertex, σ_{vtx}, was calculated from the standard deviation of the measured quantities: $\sigma_{E_i}, \sigma_{x_i}$ and σ_{y_i} for each photon ($i = 1, 2$), using the error propagation of these equations.

After reconstructing the vertex $(0, 0, Z_{\text{vtx}})$, the momentum vector of the π^0 was calculated as the sum of two photon momenta. The transverse momentum of the π^0, P_T, is expressed as

$$P_T = \sqrt{(P_x^{\pi^0})^2 + (P_y^{\pi^0})^2} \ ,$$ (6.7)

where $P_x^{\pi^0}$ and $P_y^{\pi^0}$ are x and y components of the π^0 momentum, respectively. The P_T is approximately independent of the reference frame [1], and stays within a kinematic limit. This feature played an important role in background suppression as discussed in Chapter 9.

6.3 Energy and Position Corrections

The reconstructed vertices of π^0 and the calculated directions of the two photons were used to correct the energy and position information for the photons [50].

The correction tables were prepared using MC by injecting photons with various energies, positions and angles into an array of 11×11 crystals. One table was designed to correct the energy leakage out of the CsI crystals, either forward- or backward-going. Figure 6.4 shows dependence of the energy leakage on the incident angle. The other table was designed to correct the incident angle and the position of the photons. As illustrated in Figure 6.5, the reconstructed position of the photons $P_{COG}(x_{COG}, y_{COG})$ was shifted from the true incident position P_{inc}, and should be corrected as a function of the incident angle. Figure 6.6 is an example of the correlation table obtained by MC.

The correction was iterative as shown in Figure 6.7. Once we reconstructed π^0 with two photons, we returned to the correction by using the energy correction table, and the angular correction table on that output. When the difference in one correction cycle converged, the correction was finished. Typically, the correction process converged within three iterations.

The correction tables improved the position and energy resolution of the photons, and therefore improved the resolution of the reconstructed vertices of π^0's. The results are shown in Figure 6.8.

---

[1] Strictly, the momentum direction of K_L^0 was different from the z-axis. Thus, the reconstructed P_T was not exactly the component of the momentum that is perpendicular to the K_L^0 direction.
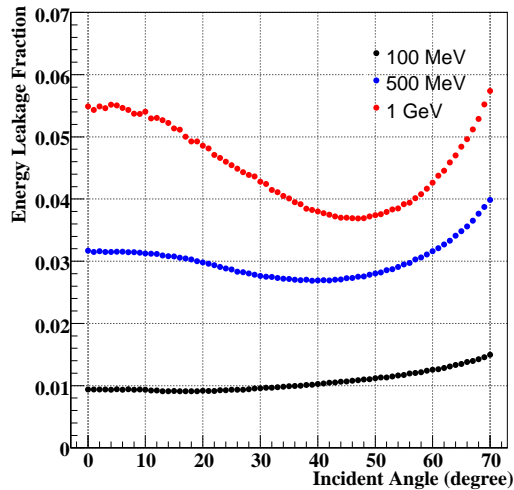
Figure 6.4: Fraction of the energy leakage in MC with photon injection to the center of 11×11 Normal CsI array. The leakage depended on the energy and the incident angle of the photons. In the case of high energy photons, the leakage was dominated by the part from the back end of the CsI crystals at $0°$ (perpendicular to the CsI surface), and dominated by the part into the upstream (called "splash-back") in higher incident angle.
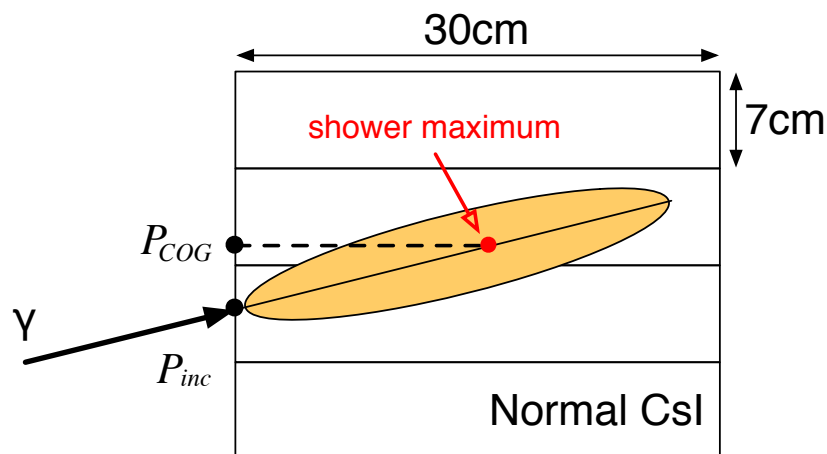
Figure 6.5: Schematic view of the position correction. Taking the shower length (L) into account, the incident position (P_{inc}) was calculated from the position of the center of gravity (P_{COG}) and the incident angle.
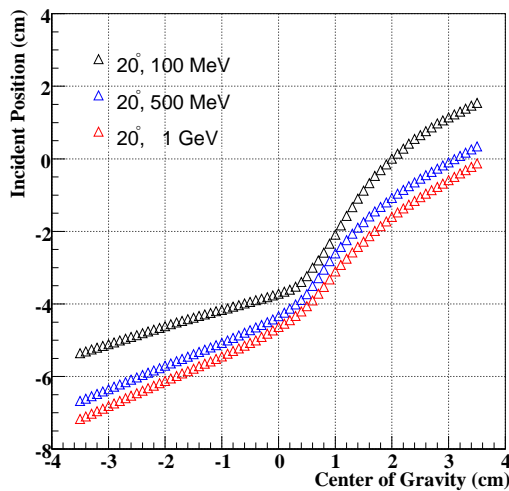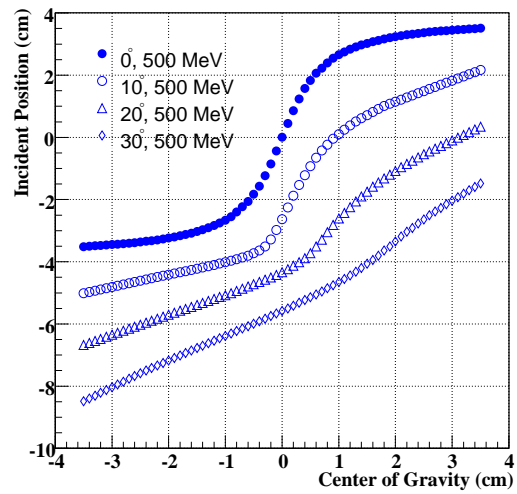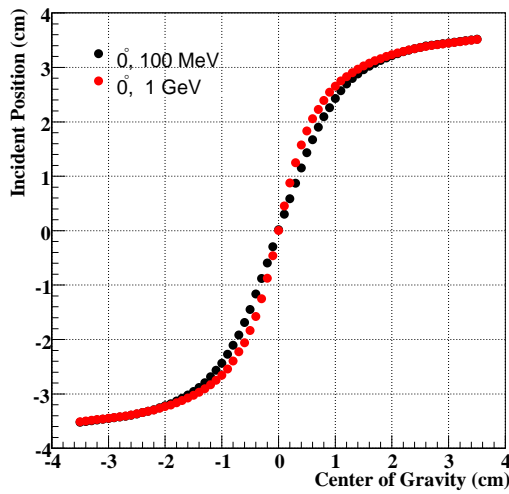
Figure 6.6: Correlation between the true hit position and x_{COG} in MC. Each plot shows dependency of the correlation on the energy and the incident angle of the photons. The CsI crystal had the size of 7×7 cm^2, thus 0 cm and 3.5 cm corresponded to the center and the edge of the crystal, respectively. Note that the vertical scales are different among the plots.
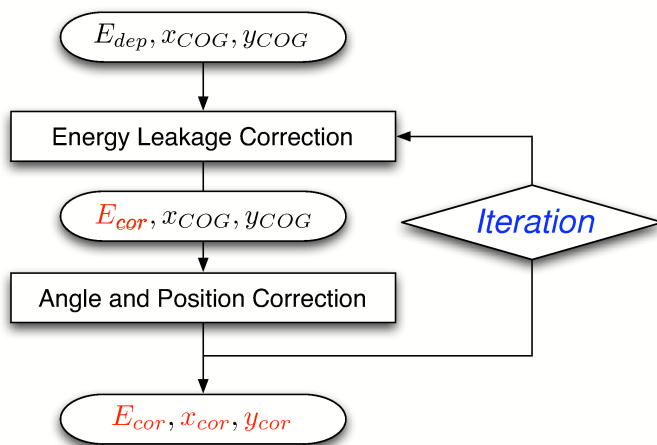
Figure 6.7: Diagramatic representation of the cluster correction table application. "cor" is an abbreviation for *corrected*.
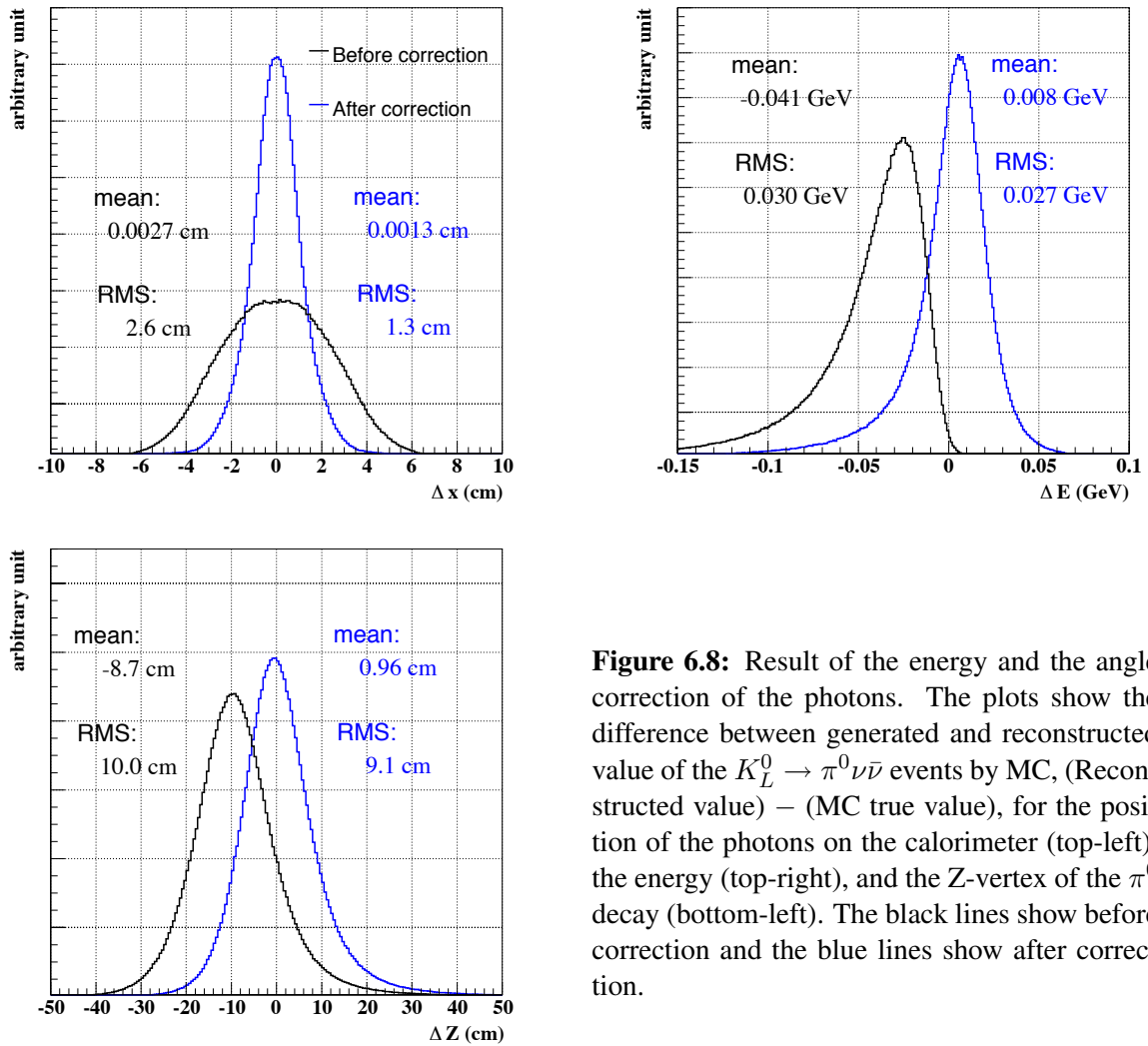
Figure 6.8: Result of the energy and the angle correction of the photons. The plots show the difference between generated and reconstructed value of the $K_L^0 \to \pi^0 \nu \bar{\nu}$ events by MC, (Reconstructed value) − (MC true value), for the position of the photons on the calorimeter (top-left), the energy (top-right), and the Z-vertex of the π^0 decay (bottom-left). The black lines show before correction and the blue lines show after correction.

Chapter 7

Event Selection

In this chapter, we summarize the background sources, and describe the event selections to discriminate the signal from the background.

In order to avoid human bias on event selection, we performed the so-called "Blind Analysis" technique [51]. First, we defined the region of interest for the $K_L^0 \to \pi^0 \nu \bar{\nu}$ signal in a certain space of kinematic variables (in the plane of P_T and Z_{vtx} in our case). The primary policy for the definition of Z_{vtx} range was to use "clean" region, separated from any materials, which is the region between CC02 and CV. For the P_T range, we used relatively high P_T according to the kinematics of $K_L^0 \to \pi^0 \nu \bar{\nu}$. Then, we determined all the selection criteria without seeing the properties of events in the region. The background estimation was finished in this stage. Finally we revealed the region. No additional criteria would be implied after that.

In Section 7.1, the background sources are summarized. We describe the veto cuts in Section 7.2, and the kinematic cuts in Section 7.3. In Section 7.4, the signal region and the blind method are discussed.

7.1 Background Sources

Figure 7.1 shows the two-dimensional plots of P_T vs. Z_{vtx} by Monte Carlo for $K_L^0 \to \pi^0 \nu \bar{\nu}$ and main background sources.

7.1.1 Kaon Backgrounds

Neutral Decay Modes

The largest background source from the kaon decays was $K_L^0 \to \pi^0 \pi^0$, where two extra photons were undetected due to the effects as:

- photon detection inefficiency and

- two overlapping photons, reconstructed as one cluster ("fused" cluster) in the CsI calorimeter.

As described in Section 2.4, the $K_L^0 \to \pi^0 \pi^0$ "even" background events remained even after being imposed kinematic constraints. Thus, the contribution of the $K_L^0 \to \pi^0 \pi^0$ background was determined by the detection inefficiency of photons.
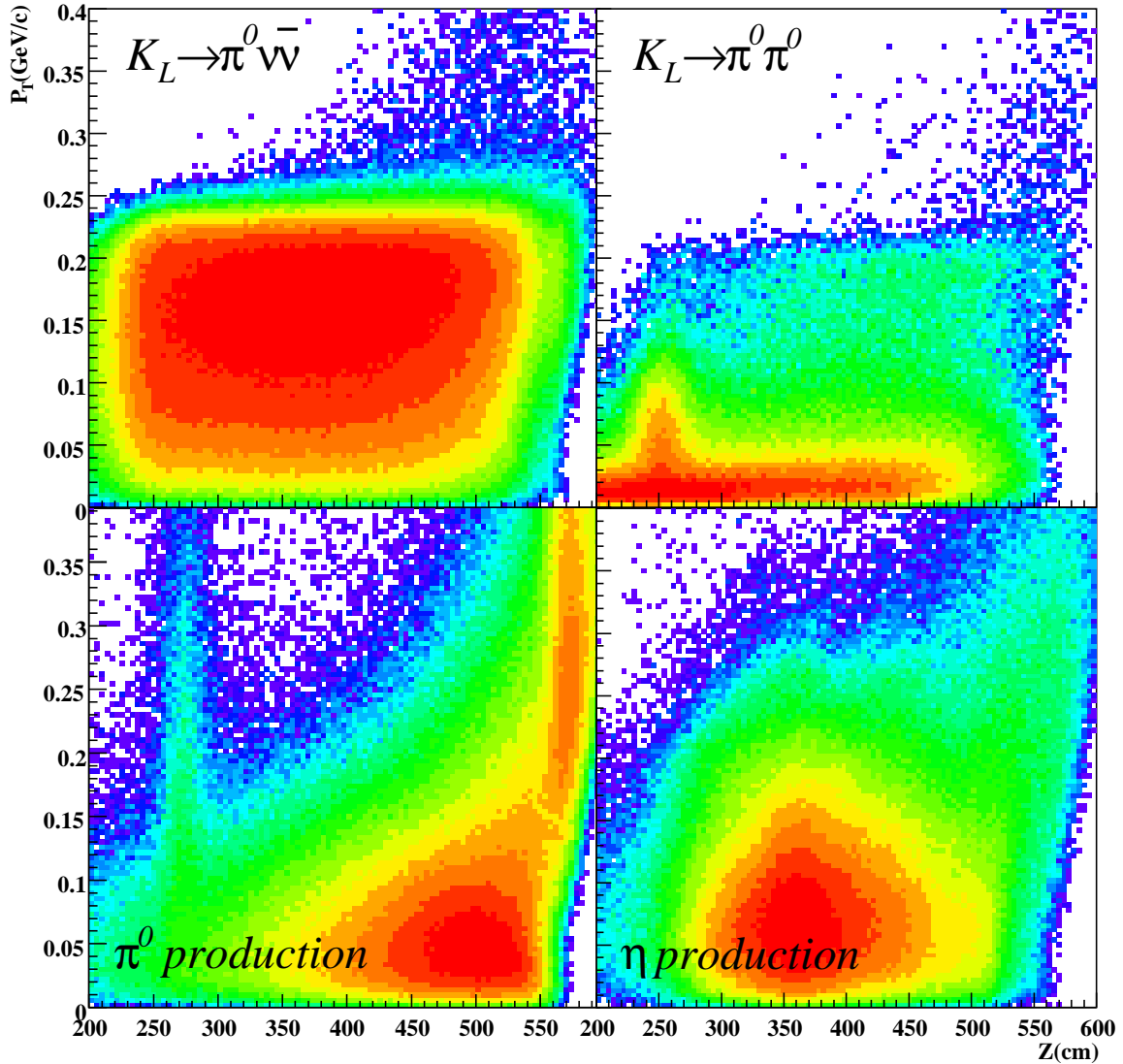
Figure 7.1: P_T versus Z_{vtx} distributions of the reconstructed π^0's for $K^0_L \rightarrow \pi^0 \nu\bar{\nu}$ signal and the background sources by MC.

Since $K^0_L \rightarrow \gamma\gamma$ has only two photons in the final state, it is impossible to remove them by the photon veto cuts. However, they could be isolated from $K^0_L \rightarrow \pi^0 \nu\bar{\nu}$ by imposing kinematic cuts.

Charged Decay Modes

Other background sources were charged decay modes, and the $K^0_L \rightarrow \pi^- e^+ \nu$ decay was a possible source if the following interactions happened in CV:

1. The charge-exchange interaction $\pi^- + p \to \pi^0 + n$

2. The pair annihilation $e^+ + e^- \to \gamma + \gamma$ in CV with the energy deposition too low to detect

3. Two of the four photons escaped detection due to detector inefficiencies and the fused cluster reconstruction.

In addition, the $K_L^0 \to \pi^+\pi^-\pi^0$ decays with the π^+ and π^- going through the beam hole without being detected by the BHCV, could be another source of background.

7.1.2 Neutron Backgrounds

There were backgrounds due to the interaction of the halo neutrons with the material in the detector components. Since the materials were placed at the Z position outside our region of interest, these interactions could be separated from the signal by the vertex position. However, as can be seen in Equations 6.3-6.5, mis-measurement of photon energies and positions caused wrong vertex reconstruction. Below, neutron backgrounds are categorized and their mechanism to contaminate the signal region are explained.

CC02 Events

The Collar Counter 02 (CC02) was exposed to the beam halo. The neutron interactions in the rear part of CC02, such as $n + N \to \pi^0 + X$ produced the $\pi^0 \to \gamma\gamma$ events that could be reconstructed with large P_T.

In principle, the reconstructed vertex should be approximately equal to the downstream face of CC02 at $Z = 275$ cm (See Figure 3.5). However, if the energy of either photon was mis-measured due to shower leakage or photo-nuclear effect, Z_{vtx} could be shifted to the downstream. Also, the finite accuracy of the vertex reconstruction, due to the position and energy resolution in the calorimeter, worsened the separation between the signal and background.

The CC02 events were the most difficult background to estimate and reject. One reason was that π^0's reconstructed from the CC02 events were indeed π^0's and quality cuts for genuine photons were not effective. The second reason was that our MC for the halo neutrons was not able to reproduce the position distribution of events in CC02 for the low energy hadronic interactions. The structural complexity of CC02 was also the reason for difficulties in comparison of parameters in the simulation and real situation.

Finally, we decided to use the data taken in the Al plate run to estimate the CC02 events (See Figure 4.1). Since the vertices of the CC02 events and the π^0's produced at the Al target were very close, the π^0 events in the Al plate run enabled us to estimate the contamination from the position of CC02 to the signal region.

CV Events

The halo neutron interactions in CV, such as $n + N \to \pi^0 + X$ and $n + N \to \eta + X$, caused background events. The $n + N \to \pi^0 + X$ events in CV, called "CV-π^0", could contaminate the signal region if an accidental hit overlapped one of the photon clusters, or if multiple-π^0's were produced and we reconstructed single π^0 with a wrong pair of photons.

The $n + N \rightarrow \eta + X$ events, called "CV-η", could enter the signal region due to the assumption in the reconstruction process that the invariant mass of two photons was m_{π^0}. If the true parent particle was an η whose mass is 547.5 MeV/c^2, the reconstructed vertex could be shifted to the upstream.

These two kinds of the background in CV were treated in different MC schemes. CV-π^0 was reproduced and estimated by GEANT3. The CV-η event was estimated by GEANT4, in which the code for η production was implemented. The cross section of η production was examined with the data in the Al plate run.

7.2 Veto Cuts

In order to reject backgrounds, our primary tool was the veto system which enables us to discard events with extra particles.

In this section, details of veto conditions are described in order.

7.2.1 Veto Timing

The event time (t_0) was defined as the average time of the two clusters in the CsI calorimeter. The relative time (or "timing") in each channel was obtained with respect to t_0. The hits in the veto counters whose timing was within the timing "windows", which depended on the time resolution in each counter, were considered to be due to visible energy.

Since the reproduction of the timing distributions was difficult to be simulated in MC, we simply set the timing window to be large enough, typically with $\pm 5\sigma$ from the peak of the timing distribution fitted by the Gaussian function. The special treatment for MB and BCV are explained later in this section.

7.2.2 Photon Veto Cuts

The backgrounds involving extra photons were suppressed by imposing the cuts to all the photon veto detectors. In the following paragraphs, we describe the selection criteria on each photon veto counter. The energy thresholds are summarized at the end of this subsection.

MB

As described in Section 3.2.3, the length of MB was 5.5 m. The scintillation light in MB was attenuated in propagating through the fibers to the PMTs. We approximated the signal attenuation from the interaction position to the PMTs as $E_{\mathrm{PMT}} = E_0 \exp(-\frac{z}{\lambda})$, where z denotes the distance to the PMT. We defined the energy deposition in MB as:

$$
\begin{aligned}
E_{\mathrm{MB}} & = c\sqrt{E_{up} \cdot E_{dn}} \\
\\
& = c\sqrt{[E_0 \exp(-\frac{z_{hit}}{\lambda})] \cdot [E_0 \exp(-\frac{L - z_{hit}}{\lambda})]} \\
\\
& = cE_0 \exp(-\frac{L}{\lambda}) \,,
\end{aligned}
\tag{7.1}
$$
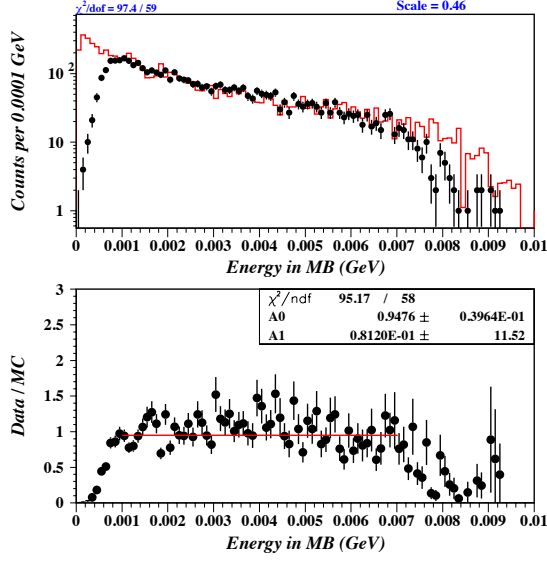
Figure 7.2: Energy distribution in MB using four cluster data (dots) and the $K_L^0 \rightarrow \pi^0\pi^0\pi^0$ MC (red histogram). The edge at 0.0008 GeV (0.8 MeV) corresponded to the TDC threshold, and the edge at around 0.008 (8 MeV) corresponded to the online veto effect. The bottom plot shows the ratio of the data divided by MC.

where c is calibration factor to each counter, $E_{dn(up)}$ is the signal recorded in the PMT at the downstream (upstream) end, E_0 is the energy deposition of the incident photon, z_{hit} is the distance from the hit position to the upstream PMT, λ is the effective light attenuation length, and L is the length of the MB. We calibrated the energy scale of MB with cosmic-ray muons whose energy deposition was 15 MeV (30 MeV) to the scintillators of inner (outer) MB module. Figure 7.2 shows the energy distribution of a MB modules with the data and the $K_L^0 \rightarrow \pi^0\pi^0\pi^0$ MC with 4 photons reconstructed in CsI and remaining 2 photons detected in MB. The energy in MB was well-reproduced by MC. We set the threshold for E_{MB} to be 1 MeV.

We found that some particles in the electromagnetic shower in the CsI calorimeter went back to MB. We called this as "splash-back" of the shower. The splash-back caused acceptance loss since it killed the signal without real extra particles.

Figure 7.3 shows the timing structure in MB with the two photon events in MC and the data. The hit position in MB was calculated with the time difference between the PMTs at the upstream and the downstream ends (T_{up}, T_{dn}) as $Z_{hit} = v \cdot (T_{dn} - T_{up})$, where v is the light velocity in the MB modules. The absolute event timing was calculated as $T = (T_{dn} + T_{up})/2$ with offsets. In Figure 7.3, the events (a) were distributed from the downstream-earlier region to the upstream-later region. This means that the particles propagated back to the upstream, thus it is correct to understand those events as "splash-back". On the other hand, (b) in Figure 7.3 shows the events in which photons hit MB directly.

It seems that there was a chance to discriminate genuine photon hits and splash-back hits by timing information. However, Figure 7.3 also shows that there were many events (c) in the later timing due to the halo neutrons. We had to impose the MB veto for all the time range in order to suppress the neutron background, except for the limited time gate of the TDC, for which we imposed $(T_{up} + T_{dn})/2 < 150(120)$ ns to MC(data).
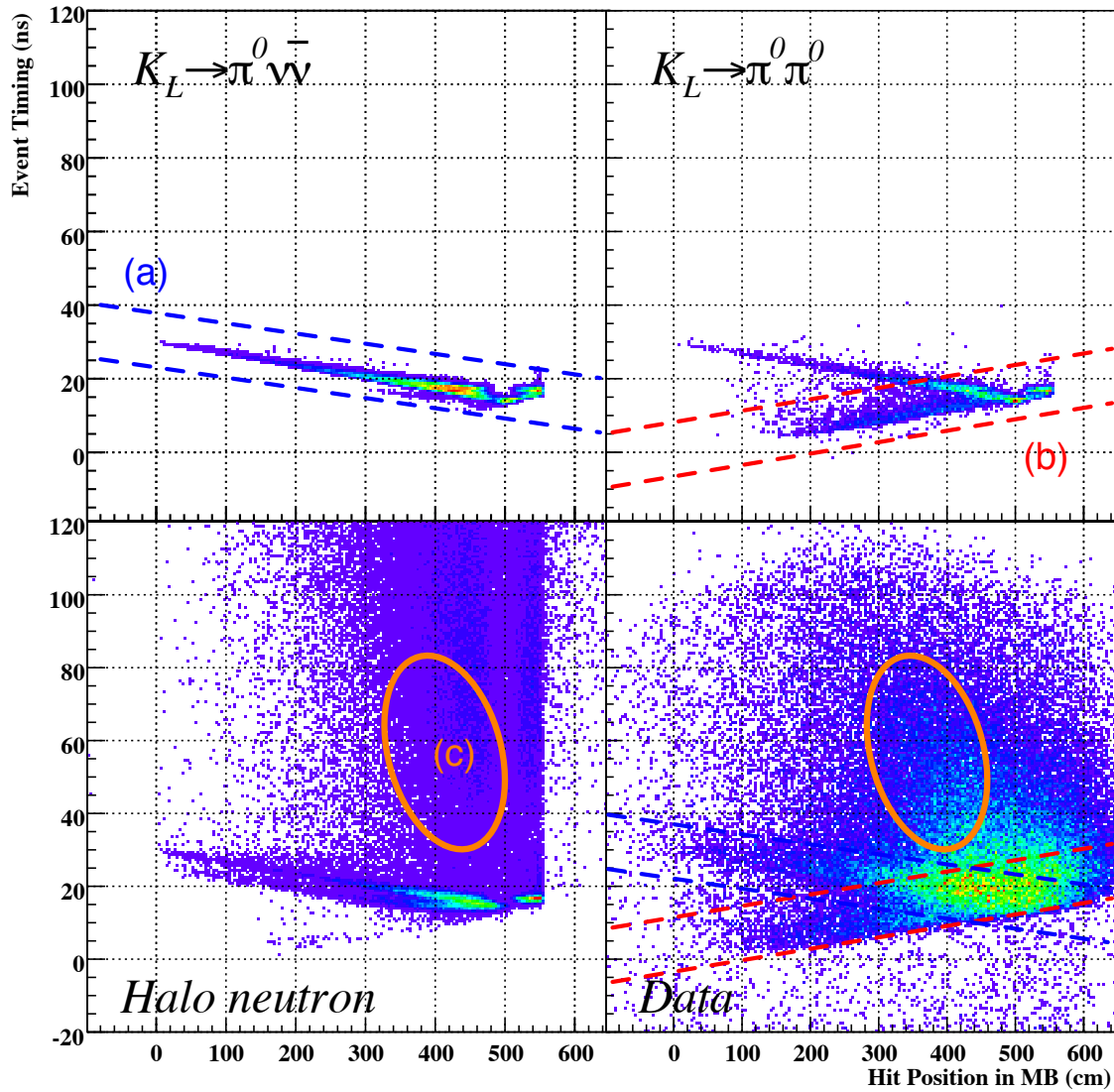
Figure 7.3: Hit timing vs. position in MB with the two photon sample for (a): splash-back from $K_L^0 \to \pi^0 \nu \bar{\nu}$, (b): incident photons from $K_L^0 \to \pi^0 \pi^0$, (c): neutrons hits from the halo neutrons in MC and the real data.
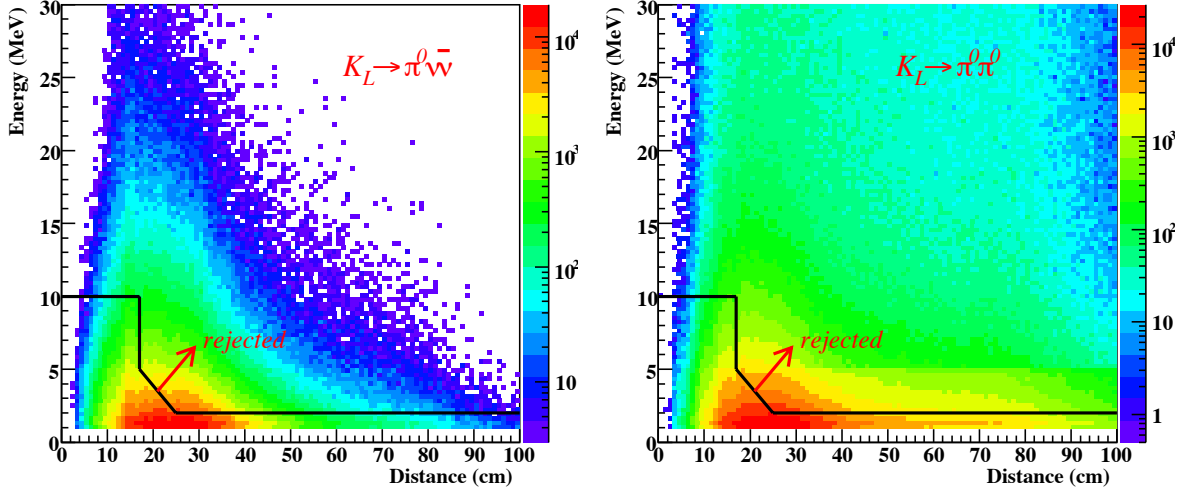
Figure 7.4: Energy in the CsI single-crystal hit vs. distance from the closest cluster with $K_L^0 \to \pi^0 \nu \bar{\nu}$ and $K_L^0 \to \pi^0 \pi^0$ MC events. The lines show the selection criteria.

CsI

Basically, the CsI veto had a function to reject the events with any additional hit in the calorimeter other than photons that constituted the signal. However, the fluctuation of the electromagnetic shower sometimes made isolated hits in its peripheral which were not judged as a part of the photon cluster, and could kill the genuine event (called "single-crystal hits"). To reduce the acceptance loss due to this effect, keeping the veto inefficiency as low as possible, we needed special treatment for the single-crystal hits.

As shown in Figure 7.4, the CsI veto was defined as a two-dimensional cut using the energy of the crystal and their minimum distance to a photon cluster. We defined the hit condition as:

1. $E > 10$ MeV for $d < 17$ cm,

2. $E > 5 - (3/8)(d - 8)$ MeV for $17 < d < 25$ cm,

3. $E > 2$ MeV for $d > 25$ cm,

where E is the energy in the single-crystal hits and d is the distance to the closest photon cluster. We imposed a loose condition for $d < 17$ cm because the single-crystal hit might be a part of the shower of the photon cluster.

BA

The BA veto had to be imposed to remove the events with extra photons escaping through the beam hole. BA were suffered from many accidental hits due to the neutrons in the beam, and we could not impose a simple and tight energy cut. The quartz part in BA, which was a Cherenkov radiator, should

be insensitive to heavy charged hadrons such as protons and pions in the hadronic shower by neutrons, and effective to select the photon hits.

The light yield in the quartz was normalized by minimum ionization particles (MIPs). The BA hit condition was that the quartz part had the Cherenkov light corresponding to 0.5 MIPs, coinciding with the energy deposition of 20 MeV in the scintillator part.

Other Detectors

We imposed simple cuts on the energy deposition in other photon veto detectors: CC00, FB, CC02, CC03, Sandwich, CC04, CC05, CC06 and CC07. For each detector subsystem, the energy was calibrated with MIPs. Each energy threshold is listed in Table 7.1.

7.2.3 Charged Particle Veto Cuts

CV

The cut on CV using the energy deposition was imposed to remove the charged decay modes, as described in Section 7.1. CV consisted of the outer and inner parts (See Figure 3.13). Since the inner part had a longer path length to the PMT than the outer part and the inner part was exposed to much more halo neutrons and decay products, we required the larger energy threshold of 0.7 MeV for the inner part. The threshold for the outer part was 0.3 MeV.

BCV

For BCV, the energy deposition by MIPs was 2 MeV. The energy and timing information of BCV were taken care of in the same way as MB. The energy threshold was set at 0.75 MeV to each module.

CC04, CC05

The one 5 mm-thick scintillator in the front layer of CC04 and in the front and rear layers of CC05 were separated from the lead-scintillator sandwich part and read out independently as charged veto counters, as described in Section 3.2.5. We set the energy thresholds of 0.7 MeV to them.

BHCV

A cut on the energy deposit in the BHCV was important for suppressing the background from the $K_L^0 \rightarrow \pi^+\pi^-\pi^0$ decay when π^+ and π^- went through the beam hole. The energy was calibrated with MIPs. We set the threshold to be 0.1 MeV.

Table 7.1: Summary of the energy thresholds imposed to the veto counters.

Detector	Threshold	Remarks
CC00	2 MeV	
FB	1 MeV	Inner & Outer Sum
CC02	1 MeV	
BCV	0.75 MeV	$\sqrt{E_{up} \cdot E_{dn}}$
MB Inner	1 MeV	$\sqrt{E_{up} \cdot E_{dn}}$
MB Outer	1 MeV	$\sqrt{E_{up} \cdot E_{dn}}$
CV Outer	0.3 MeV	
CV Inner	0.7 MeV	
CC03	2 MeV	
CsI Close	10 MeV	$d < 17$ cm
CsI Intermediate	$5 - (3/8)(d - 17)$ MeV	$17 < d < 25$
CsI Far	2 MeV	$d > 25$ cm
		d: from the closest cluster
Sandwich	2 MeV	
CC04 Scintillator	0.7 MeV	
CC04 Calorimeter	2 MeV	
CC05 Scintillator	0.7 MeV	
CC05 Calorimeter	3 MeV	
CC06	10 MeV	
CC07	10 MeV	
BHCV	0.1 MeV	
BA Scintillator	20 MeV	Sum over layers
BA Quartz	0.5 MIPs	Max layer
		(AND logic)

7.3   Kinematic Cuts

In the analysis of $K_L^0 \to \pi^0 \nu \bar{\nu}$, we called the cuts based on the energy and position of the two photons in the CsI calorimeter as "Kinematic Cuts". They were grouped into three categories:

- **Photon Quality Cuts**
  Cuts on the energy and position of each photon

- **Two Photon Cuts**
  Cuts on relations between the two photons

- π^0 **Cuts**
  Cuts on the variables of the π^0 reconstructed from the two photons

The description of the cuts and cut points are briefly summarized at the end of this section in Table 7.2.

7.3.1   Photon Quality Cuts

The photon quality cuts were imposed in order to remove the clusters that were not due to single electromagnetic shower: neutrons, charged particles, and two photons fused into one cluster.

Photon Energy Cut

We imposed a cut on the photon energy in order to remove low energy hadronic showers as well as poorly-reconstructed electromagnetic showers. We required photons that had higher and lower energy, E_H and E_L, to have more than 250 MeV and 150 MeV, respectively.

Cluster Size Cut

Cuts on the number of the CsI crystals in one cluster (Cluster Size) were imposed to remove low energy hadronic showers and recoiled protons. Cluster Size cut was also effective to remove the minimum ionizing particles from the charged decay modes.

   Figure 7.5 shows an example of the photon cluster. The parameters "csize-5" and "csize-1" are the numbers of CsI crystals with the energy deposition greater than 5 MeV and 1 MeV, respectively. We required csize-5 ≥ 3 and csize-1 ≥ 5.

Energy Ratio

We defined the energy ratio E_R as:

$$E_R = \begin{cases} \dfrac{e_1}{E_{dep}} & N \leq 2 \\[2ex] \dfrac{e_1 + e_2}{E_{dep}} & N = 3 \\[2ex] \dfrac{e_1 + e_2 + e_3}{E_{dep}} & N \geq 4 \end{cases} \tag{7.2}$$

where N is the number of the crystals whose energy is greater than 1 MeV in the cluster (csize-1), and E_{dep} is the total energy deposition in the cluster. The e_1, e_2 and e_3 are the largest, the second largest and third largest energy depositions in the crystals, respectively. This cut was effective to remove the wide-spread hadronic shower by the neutron hits. We required $E_R > 0.88$.

Timing Dispersion

We defined the timing dispersion TDI as

$$\text{TDI} \;=\; \frac{1}{N} \sqrt{ \sum_{\substack{i=1 \\ (e_i > 1\text{MeV})}}^{N} (T_i - T_m)^2 }, \qquad T_m \equiv \frac{1}{n} \sum_{\substack{i=1 \\ (e_i > 5\text{MeV})}}^{n} T_i \tag{7.3}$$

where e_i is the energy deposition in each CsI crystal, n and N are csize-5 and the csize-1, respectively. T_m is the average time of the crystals in the cluster. This cut was used to remove the accidental hit overlapped the photon cluster. We required TDI to be less than 2.0.

Photon RMS Cut

The RMS for each photon cluster was defined as:

$$\text{RMS} = \sqrt{ \frac{ \displaystyle\sum_{i=1 (e_i > 5\text{MeV})}^{n} e_i d_i^2 }{ E_{dep} } } \;, \tag{7.4}$$

where e_i is the energy deposition in each CsI crystal, n is csize-5 and d_i is the distance between the center of each CsI crystal and the center of energy of the photon cluster.

The background events involving fused clusters, where two nearby photons were misidentified as one photon, were suppressed by this cut. The RMS cut was also sensitive to the photons with large incident angles due to wide spread of the electromagnetic shower. RMS was required to be less than 4.0.
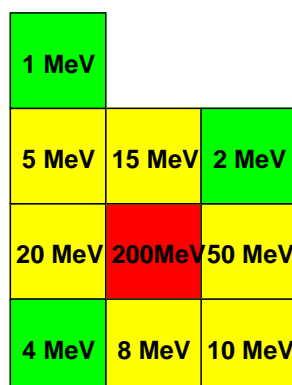
csize-5 $= 7$

csize-1 $= 10$

Figure 7.5: Example of the photon cluster.

Hit Position Cut

We required that the position of the photons in the CsI calorimeter should be outside the 18.0 cm ×
18.0 cm square area centered at the CsI calorimeter. This is because the photons produced by the halo
neutrons hitting CV produced hits close to the beam hole.

    We also required that all the photons in the CsI calorimeter should be within 88 cm from the center
of the CsI calorimeter. This was to remove photons with shower leakage out of the calorimeter.

7.3.2   Two Photon Cuts

The cuts using the information of both two photons were mainly used to remove the accidental hits.

Distance Cut

We required the minimum distance between two clusters to be 15 cm in order to avoid mis-identification
of one photon to two.

Time Difference Cut

In addition to the spatial separation, we also required that the difference between the timings of two
photons to be from -9.6 to 18.4 ns in order to suppress background contamination due to the accidental
activity.

Energy Balance Cut

The energy balance of the two photons B_E was defined as:

$$B_E = \frac{E_H - E_L}{E_H + E_L} \; , \tag{7.5}$$

where E_H and E_L are the higher and lower energy of the photons, respectively. In order to remove
events including a soft cluster due to accidental activities, we required B_E to be less than 0.75.

7.3.3 π^0 Cuts

We imposed the π^0 cuts in order to remove $K_L^0 \to \gamma\gamma$ events, $\eta \to \gamma\gamma$ events, and the π^0 events
produced by halo neutrons.

Kinetic Energy Cut

The kinetic energy of the reconstructed π^0 was required to be below 2 GeV to remove energetic neutron
interactions.
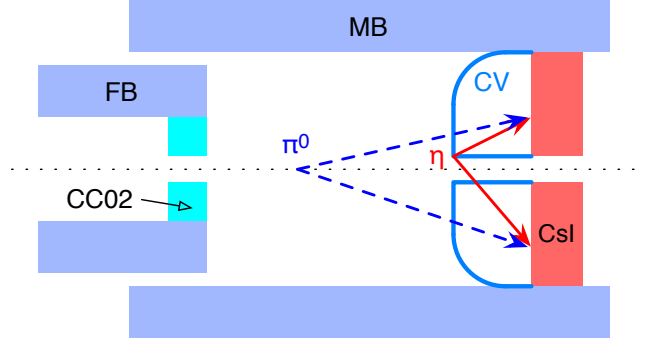
Figure 7.6: Example of the η production. The red arrows show the photons from the $\eta \to \gamma\gamma$ decay. The blue dashed arrows show the reconstructed path of the photons by assuming that the invariant mass of the two photons is equal to the π^0 mass.

$\Delta\theta\chi^2$ Cut

In order to remove the η background, we developed a cut using the difference between the incident angle measured by the cluster shape and the angle calculated with the reconstructed vertex [52]. As shown in Figure 7.6, if we reconstructed a π^0 with two photons from the $\eta \to \gamma\gamma$ decay at CV by assuming that the invariant mass is equal to the π^0 mass, the reconstructed incident angles would be different.

We first defined a spherical expansion of the photon RMS r_l with the angle α, as shown in Figure 7.7:

$$r_l = \sqrt{\frac{\sum\limits_{\substack{i=1(e_i>5\mathrm{MeV})}}^{n} e_i \cdot (d_i P_l(\cos\alpha))^2}{E_{dep}}} \ , \tag{7.6}$$

where P_l are the l-th order Legendre polynomials, and the other variables are the same as those used in Equation 7.4. Thus, r_0 is the same as the photon RMS and r_1 is the RMS projected along the radial direction. Using the single photon MC, we made the map which connected r_1 with the photon incident angle as a function of energy, as shown in Figure 7.8. We achieved resolution of about $9°$, as shown Figure 7.9.

Since the resolution of this angle measurement depended on the energy of the photons, as shown in Figure 7.8, we defined a weighted variance of the difference between the measured angle and the reconstructed angle as:

$$\Delta\theta\chi^2 \equiv \left(\frac{\theta_{r_1} - \theta_{rec.}}{\sigma_{r_1}}\right)^2 \ , \tag{7.7}$$

where the notations θ_{r_1} and $\theta_{rec.}$ represent the angles measured by the function with r_1 and by the reconstructed angle, respectively. σ_{r_1} means the resolution of the r_1 measurement.

We took the sum of the $\Delta\theta\chi^2$ for two photons, and required the sum to be less than 1.0, as shown in Figure 7.10.

Acoplanarity Angle Cut

$K_L^0 \to \gamma\gamma$ events had small P_T and were generally unable to contaminate in the signal region. However, if one of the photons was mis-measured due to the photo-nuclear interaction or the large leakage of the
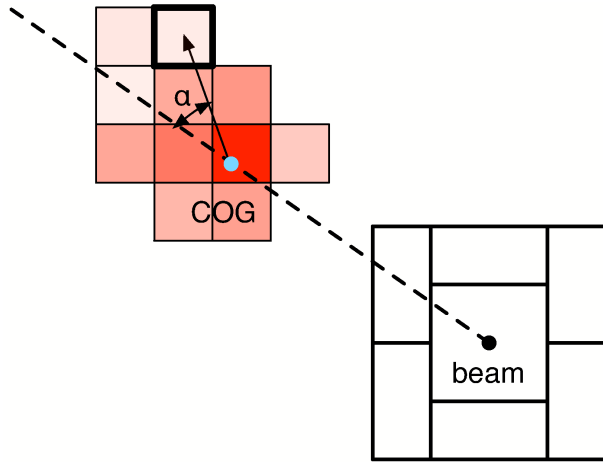
Figure 7.7: Example of the angle α to calculate r_l in Equation 7.7 in a photon cluster: α for each CsI crystal is defined by the angle between the radial direction and the line between the center of gravity (energy) of the photon cluster to the center of the crystal.
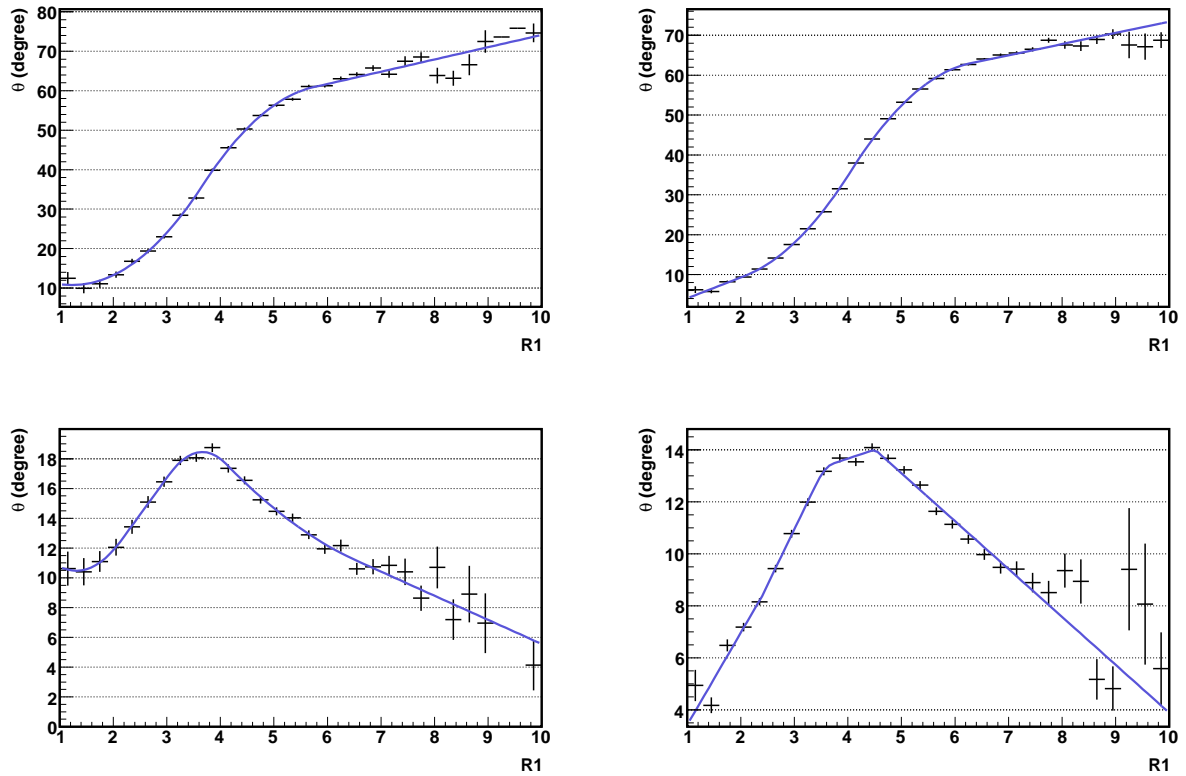
Figure 7.8: Examples of mapping from r_1 to the photon incident angle. The top-left figure shows the mean value, and the bottom-left figure shows the resolution of the mapping. Both of the results were produced with the photons of $E_\gamma < 0.5$ GeV. The right figures were with the photons of $0.5 < E_\gamma < 1.0$ GeV.
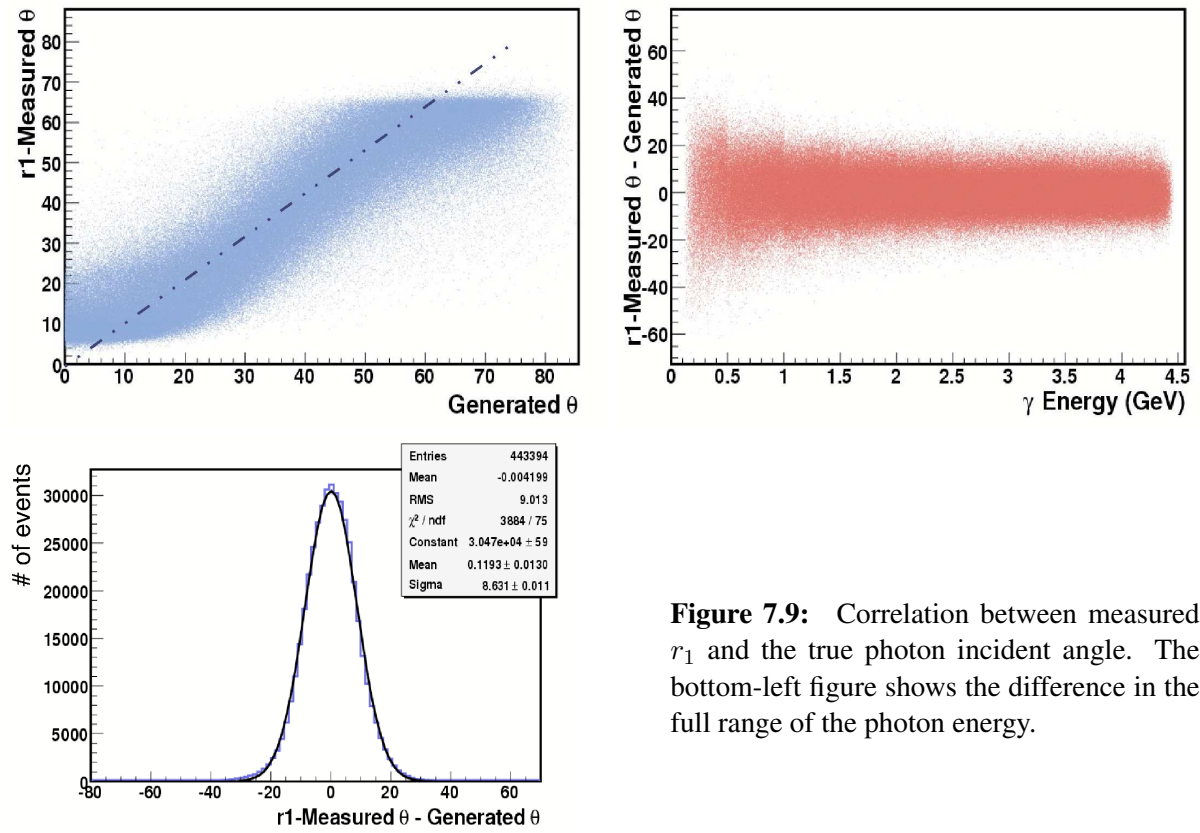
Figure 7.9: Correlation between measured r_1 and the true photon incident angle. The bottom-left figure shows the difference in the full range of the photon energy.
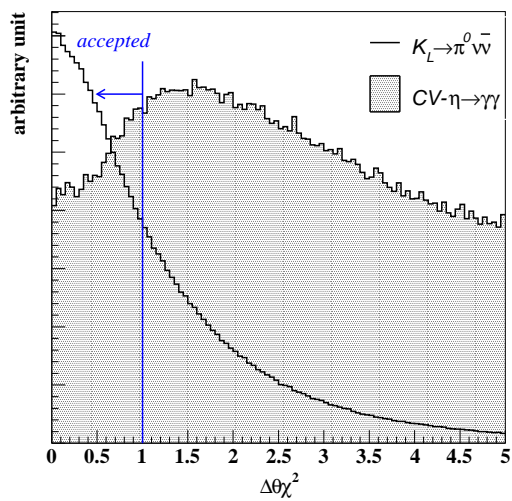
Figure 7.10: Distribution of $\Delta\theta\chi^2$ obtained by the $K_L^0 \to \pi^0\nu\bar{\nu}$ and CV-η MC.

electromagnetic shower, the $K_L^0 \to \gamma\gamma$ events could result in high P_T. In order to suppress such events, we introduced the quantity so-called "acoplanarity angle", as shown in Figure 7.11:

$$\theta_{acop.} = \pi - \arccos\left(\frac{\mathbf{r}_{\gamma_1} \cdot \mathbf{r}_{\gamma_2}}{|\mathbf{r}_{\gamma_1}||\mathbf{r}_{\gamma_2}|}\right), \tag{7.8}$$

where $\mathbf{r}_{\gamma_1}$ and $\mathbf{r}_{\gamma_2}$ are the transverse momentum vectors of the two photons.

The acoplanarity angle distributions are different between the $K_L^0 \to \pi^0 \nu\bar{\nu}$ signal and the $K_L^0 \to \gamma\gamma$ background, as shown in Figure 7.12. We required the acoplanarity angle to be larger than $45°$.
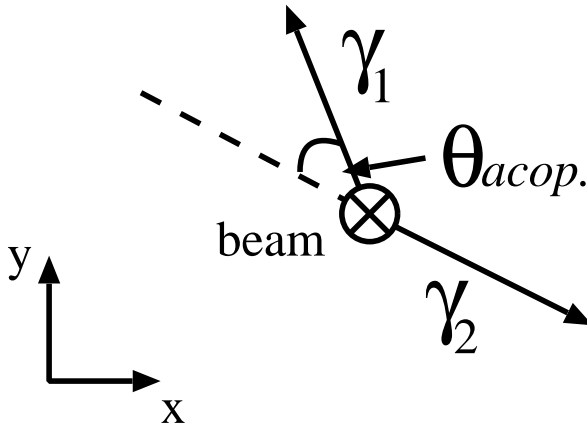
Figure 7.11: Schematic view of the acoplanarity angle, defined in Equation 7.8.
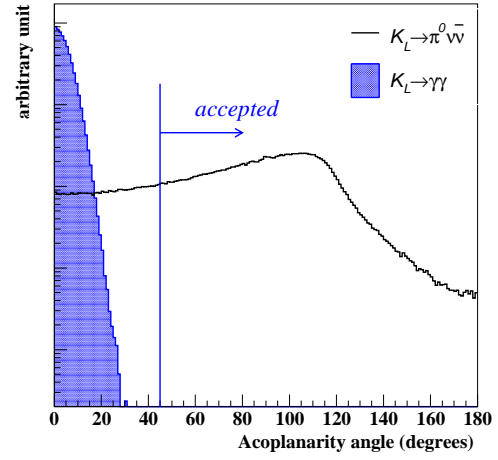
Figure 7.12: Distributions of the acoplanarity angle obtained by the $K_L^0 \to \pi^0 \nu\bar{\nu}$ and $K_L^0 \to \gamma\gamma$ events in MC.

π^0-Projection Cut

In order to remove the CV-π^0 and CV-η backgrounds, we imposed another kinematic cut. We defined "π^0-projection" using $P_R \equiv P_T/P_Z$ vs. Z plot (where P_Z is longitudinal momentum). As shown in Figure 7.13, the events outside red lines were rejected. The selection criteria were set as

- $Z < 400$ and $P_R < 0.1$

- $Z > 400$, and the events are located below the line defined by (400 cm, 0.1) and (500cm, 0.15) in (Z, P_R) the space in Figure 7.13

- the events are located above the line defined by (300 cm, 0.2) and (500 cm, 0.34) in (Z, P_R) space in Figure 7.13

P_R represents the direction of π^0, thus $P_R \times (Z_{CsI} - Z_{\text{vtx}})$ means the projection of the trajectory of the π^0 on the CsI surface.
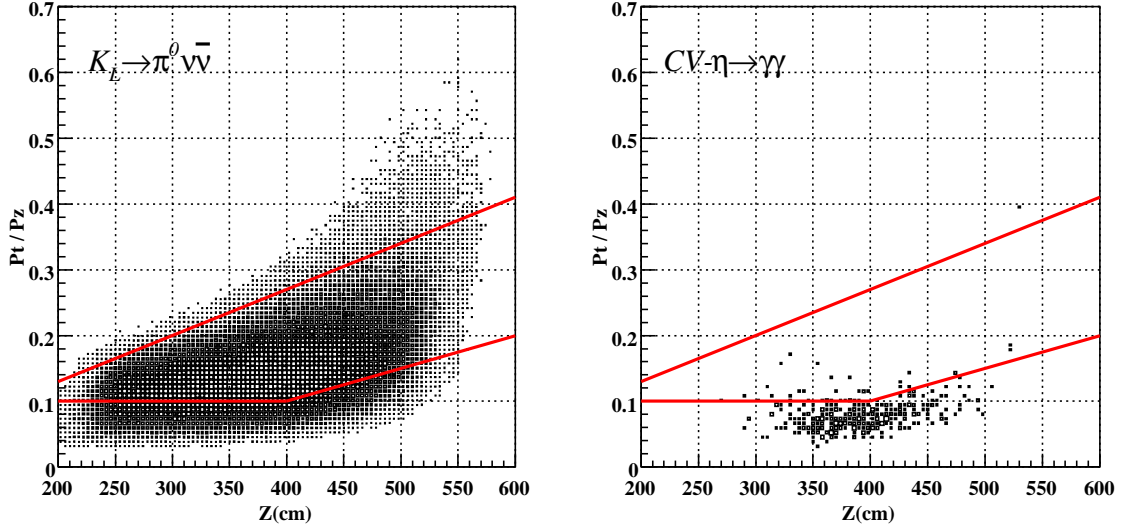
Figure 7.13: π^0-projection cut by the $K_L^0 \to \pi^0 \nu \bar{\nu}$ (left) and CV-η (right) MC. The events in the region within the red lines were accepted.

Missing Momentum Cut

With known invariant mass of the $\nu\bar{\nu}$ system, we would be able to reconstruct the momentum of K_L^0 from the π^0 momentum in the $K_L^0 \to \pi^0 \nu\bar{\nu}$ decay. We defined the "missing momentum" of the $\nu\bar{\nu}$ system in each event by assuming the invariant mass of the $\nu\bar{\nu}$ system ($m_{\nu\bar{\nu}}$) to be 0, i.e., assuming a two-body decay.

We calculated the missing momentum (P_{miss}) with the constraint that P_T of the whole system should be balanced:

$$m_{\nu\bar{\nu}} \equiv 0$$

$$A = E^2 - P_Z^2$$

$$B = \frac{1}{2}(m_{K_L^0}^2 - m_{\pi^0}^2) - P_T$$

$$D = (B \cdot P_Z)^2 - A(E^2 \cdot P_T^2 + m_{\nu\bar{\nu}}^2) - B^2)$$

$$P_{miss} = (B \cdot P_Z - \sqrt{D})/A$$

$$P_{min} = P_{miss} + P_Z$$

(7.9)

where E, P_T and P_Z are the total energy, the transverse momentum, and the longitudinal momentum of π^0, respectively. P_{min} is the minimum value of the reconstructed momentum of K_L^0 within the range of the $K_L^0 \to \pi^0 \nu\bar{\nu}$ decay. P_{min} was found to be larger in the CC02 background events than the typical

signal events, as shown in Figure 7.14. The distribution of the CC02 background were reproduced by the events in the Al plate run, as described later in Section 9.2. Thus, we studied this cut with the data in the Al plate run. We required $P_{min} < 2$ GeV.
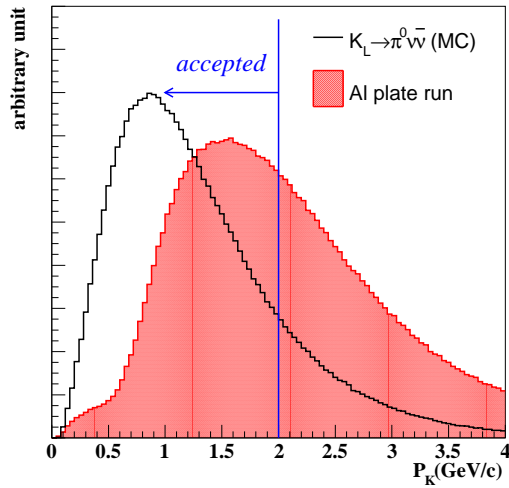
Figure 7.14: Distribution of the reconstructed K_L^0 momentum, P_{min}, assuming $m_{\nu\bar{\nu}} = 0$ in the $K_L^0 \rightarrow \pi^0 \nu \bar{\nu}$ signal MC (solid) and the data in the Al plate run (hatched).

Table 7.2: Summary of the kinematic cuts for the $K_L^0 \to \pi^0 \nu \bar{\nu}$ events

Cut		Min.	Max.
Photon Quality Cuts	Higher Energy	250 MeV	
	Lower Energy	150 MeV	
	Cluster Size 5 MeV	3	
	Crystal Size 1 MeV	5	
	Energy Ratio	0.88	
	TDI		2.0
	RMS		4.0
	Hit Position (square)	18 cm	
	Hit Position (radial)		88 cm
Two Photon Cuts	Distance	15 cm	
	Timing Differece	-9.6 ns	18.4 ns
	Energy Balance		0.75
π^0 Cuts	Kinetic Energy		2 GeV
	$\sum \Delta\theta\chi^2$		1.0
	Acoplanarity Angle	45°	
	π^0-Projection	see text	
	Missing Momentum		2.0 GeV

7.4 Signal Region

In this section, we explain the way to determine the signal region with Z-vertex and P_T.

7.4.1 Vertex

The signal region of the reconstructed Z vertex with two photons was originally set as $300 \leq Z_{\text{vtx}}(\text{cm}) \leq 500$ in order to avoid the contamination from the beam interactions at the detector; the surface of CV was located at $Z = 565$ cm and the downstream side of CC02 was located at $Z = 275$ cm.

Since the upstream end of the signal region was too close to the background source of CC02 events, we tightened the end by checking the S/N to the CC02 events. We finally set the Z vertex region to be $340 \leq Z_{\text{vtx}}(\text{cm}) \leq 500$. The Z_{vtx} region 300–340 cm was called "control region" and used to confirm the validness of our background estimation.

7.4.2 P_T

We primarily required $P_T \geq 0.12$ GeV/c in order to suppress π^0 from the $\Lambda \to \pi^0 n$ decay, whose maximum P_T is 109 MeV/c. The P_T cut was also effective to remove the $K_L^0 \to \pi^0\pi^0$ odd background.

The upper boundary on P_T was determined to be $P_T \leq 0.24$ GeV/c due to the kinematic limit of the $K_L^0 \to \pi^0 \nu\bar{\nu}$ decay ($P_{max} = 0.231$ GeV/c), allowing for the smearing effects of P_T due to detector resolutions.

7.4.3 Blind Region

For the blind analysis, we first made the data sample excluding the events with $300 \leq Z_{\text{vtx}}(\text{cm}) \leq 500$ and $0.12 \leq P_T(\text{GeV}/c) \leq 0.24$. After we established the background studies of the CC02 events, we opened the control region $300 \leq Z_{\text{vtx}}(\text{cm}) \leq 340$ to confirm the number of the background events. Since then, we examined the signal region with $340 \leq Z_{\text{vtx}}(\text{cm}) \leq 500$ and $0.12 \leq P_T(\text{GeV}/c) \leq 0.24$.

Chapter 8

Normalization

We calculated the K_L^0 flux with the normalization modes: $K_L^0 \to \pi^0\pi^0\pi^0$, $K_L^0 \to \pi^0\pi^0$, and $K_L^0 \to \gamma\gamma$ decays. This chapter first provides the number of the K_L^0 and the overall systematic uncertainty concerning to the flux. We describe the methods to tune various distributions in MC to reproduce the data, and to estimate the accidental loss. The acceptance for $K_L^0 \to \pi^0\nu\bar{\nu}$ and the single event sensitivity (SES) were obtained with these studies.

8.1 K_L^0 Flux

8.1.1 K_L^0 Reconstruction

Here we briefly explain the reconstruction of K_L^0's with $K_L^0 \to \pi^0\pi^0\pi^0$, $K_L^0 \to \pi^0\pi^0$, and $K_L^0 \to \gamma\gamma$ decays. More details of the methods and the selection criteria are discussed in Appendix A.

For $K_L^0 \to \pi^0\pi^0\pi^0$ and $K_L^0 \to \pi^0\pi^0$, we first reconstructed π^0's from all the possible combinations of the photons: $(_6C_2 \times_4 C_2 \times_2 C_2)/3! = 15$ for $K_L^0 \to \pi^0\pi^0\pi^0$, and $(_4C_2 \times_2 C_2)/2! = 3$ for the $K_L^0 \to \pi^0\pi^0$ decay. For each combination we calculated the variance of reconstructed Z-vertices, "pairing χ_Z^2", as:

$$\chi_Z^2 = \sum_{i=1}^{n} \frac{(Z_i - \bar{Z})^2}{\sigma_i^2} \ , \tag{8.1}$$

where

$$\bar{Z} = \frac{\sum_{i=1}^{n} Z_i/\sigma_i^2}{\sum_{i=1}^{n} 1/\sigma_i^2}, \tag{8.2}$$

$n = 3$ for $K_L^0 \to \pi^0\pi^0\pi^0$ and $n = 2$ for $K_L^0 \to \pi^0\pi^0$ (See Figure 8.1). Here, Z_i is the reconstructed vertex of each π^0 and σ_i is the error of Z reconstruction propagated from the energy and position resolution of the CsI calorimeter. We then ordered combinations by the pairing χ_Z^2 and chose the combinations with two lowest χ_Z^2's values. The lowest χ_Z^2 was the most preferable solution; However, in order to discriminate the cases where two combinations were close to each other in the χ_Z^2's and the correct solution might have been fluctuated to the larger value of χ_Z^2, we required the χ_Z^2 value of the second best solution to be relatively large.

For $K_L^0 \to \gamma\gamma$ reconstruction, we calculated P_T and Z_{vtx} assuming K_L^0 mass with the two photons, in the same way as π^0 reconstruction.
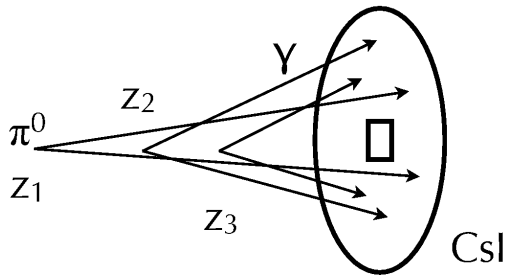
Figure 8.1: Diagram of $K_L^0 \rightarrow \pi^0\pi^0\pi^0$ reconstruction. We independently reconstructed the Z_{vtx} of each pair of photons, and checked their consistency. 15 combinations of photon pairs were tried and the combination with the smallest variance was chosen.
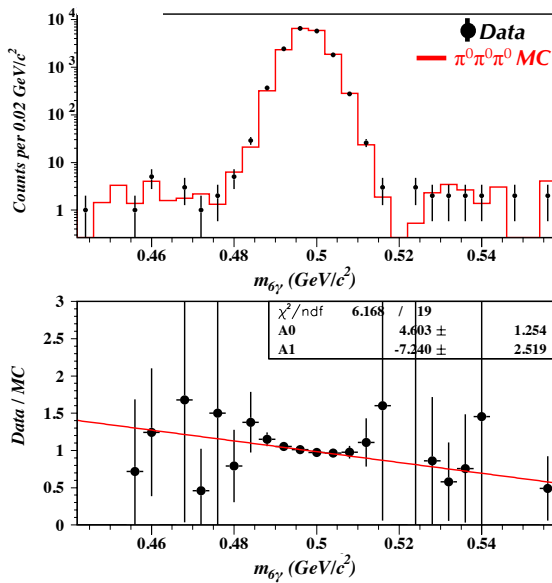
Figure 8.2: Invariant mass spectrum with $K_L^0 \rightarrow \pi^0\pi^0\pi^0$. The data are represented by the black dots and the MC by the red histogram in the top plot. The bottom plot shows the ratio of (Data/MC). The red line shows the result of a linear fitting to the radio.

8.1.2   MC Tuning

The initial distributions in MC for the K_L^0 beam were taken from the beam line simulation. However, due to deviations from the actual distributions, the results from data and MC were sometimes found to disagree. In order to reproduce data, we tuned parameters in MC. Here, the comparisons between data and MC are shown and the tuning process are described.

Invariant Mass

As mentioned in Section 5.4, we introduced additional smearing to the photon energy measured in the CsI calorimeter. Figure 8.2 shows the results of the reconstruction of $K_L^0 \rightarrow \pi^0\pi^0\pi^0$ events. The width of the invariant mass was well-reproduced. The small difference, indicated by the slope in the fitting for the event ratio, was included in the systematic uncertainty.
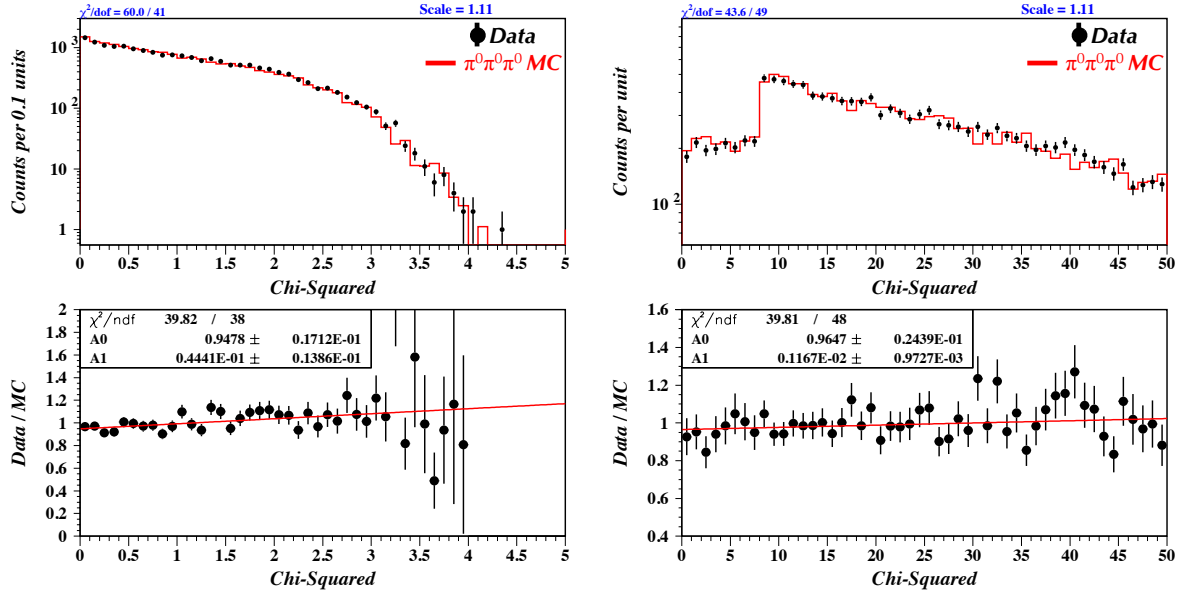
Figure 8.3: Lowest χ_Z^2 value (left) and the second-lowest χ_Z^2 minus the lowest χ_Z^2 values (right) with $K_L^0 \to \pi^0\pi^0\pi^0$.

Pairing χ_Z^2

The pairing χ_Z^2, defined in Equation 8.1, was sensitive to the resolution in the calorimeter and was one of the most difficult distributions for us to reach agreement. We obtained good agreement by the crystal-by-crystal energy smearing functions described in Section 5.4, as shown in Figure 8.3.

Momentum and Decay Vertex

We tuned the K_L^0 generator in MC to check the momentum and Z-vertex distributions. Here, we used $K_L^0 \to \pi^0\pi^0\pi^0$ which had many kinematic constraints. We moved the parameters for the momentum distribution in K_L^0 generation described in Section 5.2, and searched for the optimized point. As shown in Figure 8.4 and 8.5, even after tuning, the ratio between the data and the MC in the momentum and Z-vertex spectra was not flat. However, when we remove the CsI veto for the $K_L^0 \to \pi^0\pi^0\pi^0$ reconstruction, the spectrum of the ratio was improved. Thus, we did not tune it any further and included this uncertainty in the systematic error.

Radial Beam Shape

We found a significant discrepancy in the radial shape of the K_L^0 beam at the exit of the last collimator (C6), as shown in Figure 8.6. This was because we used a cylindrically-symmetric generator while the real shape was oval. Thus, we applied an empirical weight function to the reconstructed values of MC
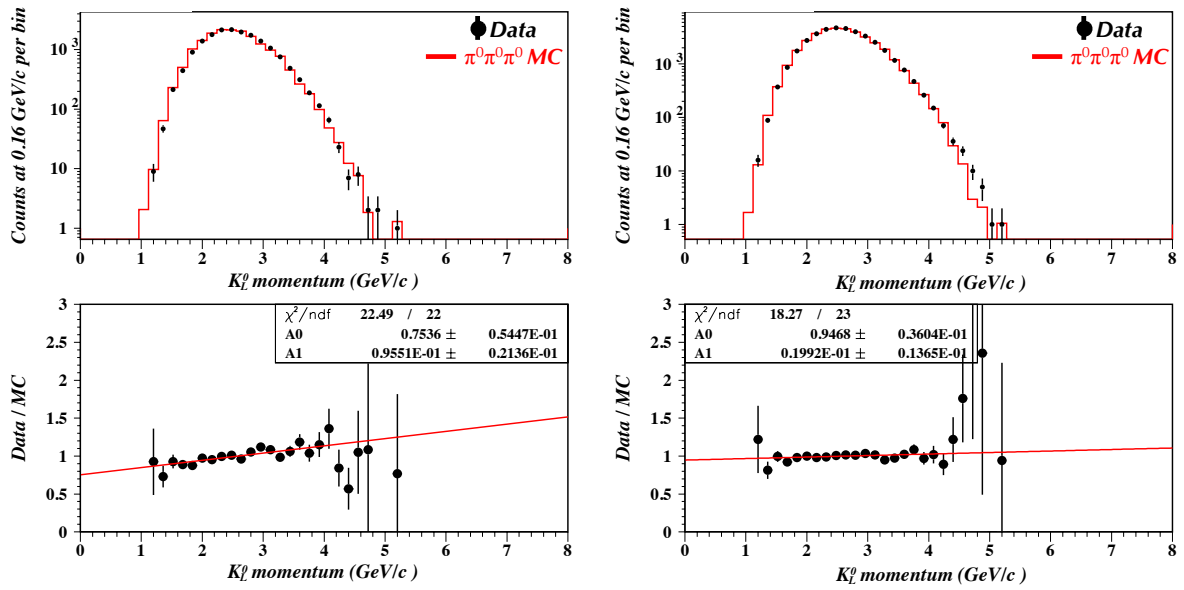
Figure 8.4: K_L^0 momentum spectrum from $K_L^0 \to \pi^0\pi^0\pi^0$. All cuts were imposed for the figure on the left while the CsI veto cut was removed for the figures on the right.
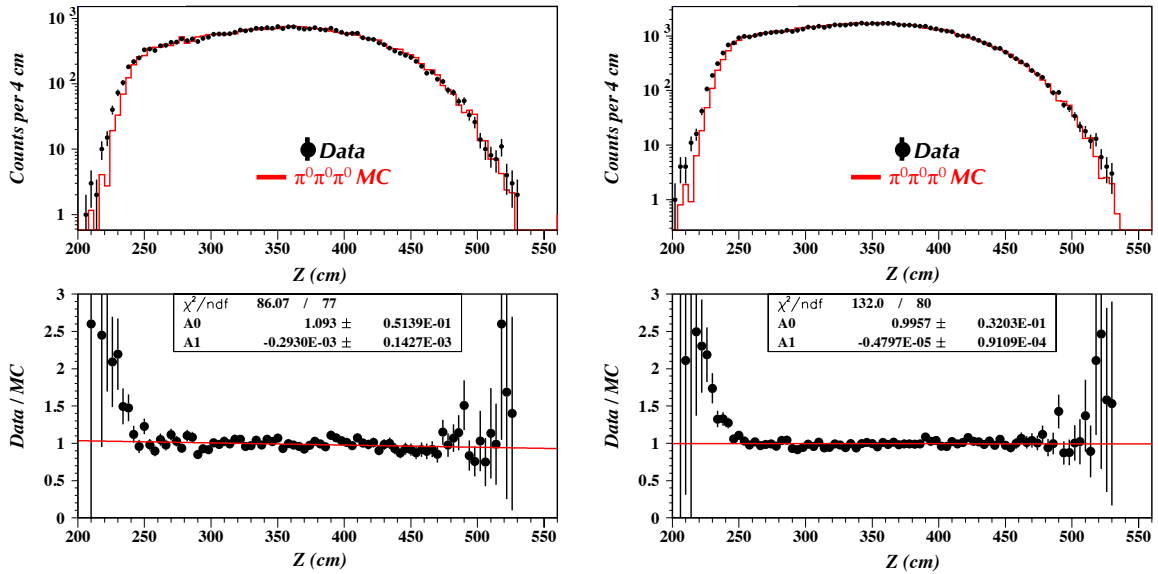
Figure 8.5: Decay Z spectrum from $K_L^0 \to \pi^0\pi^0\pi^0$. All cuts were imposed except for the fiducial cut to the figures on the left. The CsI veto cut was removed from the figures on the right.
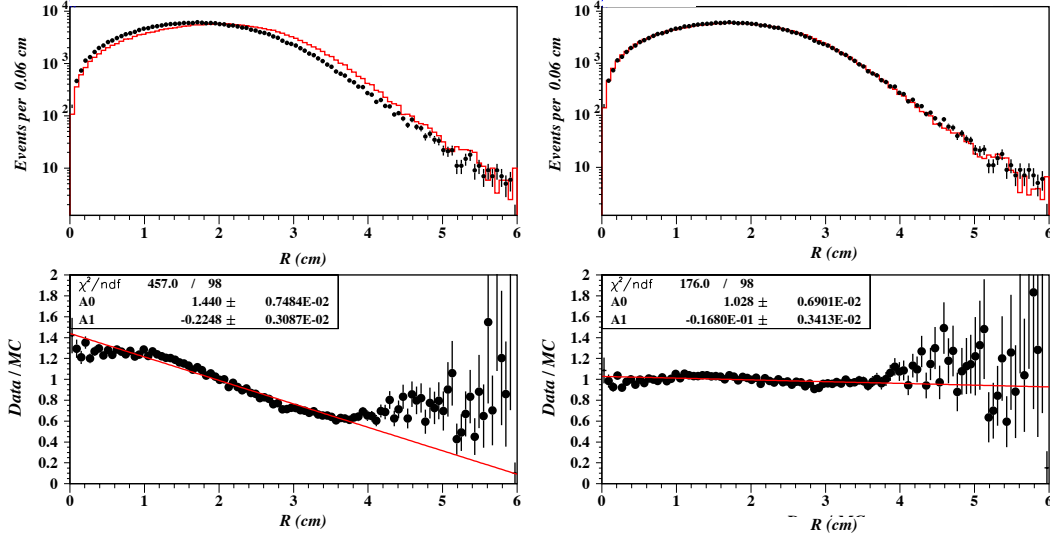
Figure 8.6: Reconstructed radial spectrum of K_L^0 at the exit of the last collimator (C6): before (left) and after (right) the weight factor was applied described in the text.

events (not in the generation) [1] as:

$$w = 1.305 - 0.192559 \, r_{gen}^2 + 0.0029822 \, r_{gen}^4 \,, \tag{8.3}$$

where r_{gen} is the radius of the generated K_L^0 at C6.

Beam Angle

In Figure 8.7, we show the beam direction angles θ and ϕ obtained with $K_L^0 \to \pi^0 \pi^0 \pi^0$ events. The polar angle was coupled explicitly to the radial position at C6 in the generation stage. We applied additional weight for the radial distribution of the K_L^0 beam, as described above.

The azimuthal angle distribution was approximated by a sinusoidal function, as shown in the right plot in Figure 8.7.

8.1.3 Accidental Loss

When the primary protons struck the target, a huge number of particles were produced. Many of these particles could be removed via sweeping magnets and absorbers; however, a large flux of photons and neutrons remained and entered the detector simultaneously with the K_L^0's. These additional particles interacted with the detector materials and made accidental hit, which caused an efficiency loss (accidental loss) due to over vetoing.

We employed two methods to take this effect into account. One was to analyze data taken by the accidental trigger and multiply estimated loss to the results from the analysis on raw MC sample, called the "Pure" MC. The other was to overlay the accidental data on the MC sample event-by-event,

---

[1]This weight factor was also applied on all the other decay modes including $K_L^0 \to \pi^0 \nu \bar{\nu}$.
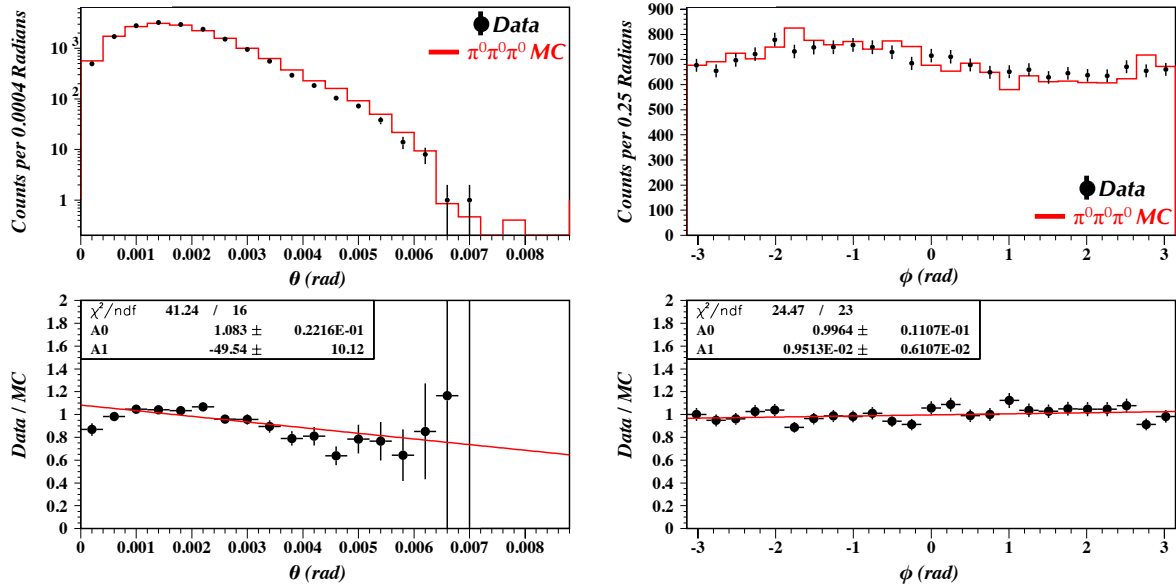
Figure 8.7: Polar and azimuthal beam angles at C6 with $K_L^0 \to \pi^0\pi^0\pi^0$.

called the "Add-BG" MC. In the latter, we took the earliest time among the native MC output and the accidental to merge their timing information for each channel. We set the same time window on the Add-BG MC as the data.

For the Pure MC, the accidental loss is expressed as:

$$\text{Accidental Loss} = B \cdot C_1 \cdot C_2 \ , \tag{8.4}$$

where B is the loss due to all the photon veto cuts except for the CsI calorimeter, C_1 is the loss due to additional clusters in CsI, and C_2 is the mode-specific loss in the CsI due to accidental activity that did not produce any extra cluster. B was estimated by examining accidental data and counting the number of events that were vetoed by the detectors other than CsI. C_1 was estimated by counting the fraction that contained one or more reconstructed cluster in the CsI in the accidental triggers. We imposed no photon quality cuts on these events.

The CsI hits which did not belong to any cluster should be specially treated because the veto condition was a function of the distance from photon clusters, as explain in Section 7.2.2. The effect could not be estimated from accidental data alone. Also, it depended on the number of genuine clusters, thus on the decay modes. C_2 was estimated by looking at the ratio of the exclusive acceptance of the CsI veto with the Pure and Add-BG MC, where the "exclusive" acceptance was the acceptance of one cut with all the other cuts imposed.

The results of the accidental loss estimation are summarized in Table 8.1.

Table 8.1: Accidental losses for the normalization modes. The parameters B, C_1 and C_2 are defined in the text. The errors are statistical only.

Mode	$K_L^0 \to \pi^0\pi^0\pi^0$	$K_L^0 \to \pi^0\pi^0$	$K_L^0 \to \gamma\gamma$
B	$84.76 \pm 0.05\%$		
C_1	$99.33 \pm 0.04\%$		
C_2	$98.45 \pm 1.43\%$	$97.99 \pm 1.35\%$	$97.95 \pm 0.57\%$
Total	$82.89 \pm 1.43\%$	$82.50 \pm 1.35\%$	$82.47 \pm 0.57\%$
Weighted average	$82.57\ \%$		

8.1.4 Systematic Errors

The systematic error on the flux was defined as:

$$\sigma_{\text{syst.}}^2 = \frac{\sum_{i=\text{cuts}} \left(F^i / A_{data}^i\right)^2}{\sum_{i=\text{cuts}} \left(1/A_{data}^i\right)^2} \,, \tag{8.5}$$

$$F^i = \frac{A_{data}^i - A_{MC}^i}{A_{data}^i} \,,$$

where i denotes a specific cut, and A is defined as the acceptance of the cut with all the other cuts imposed, called "exclusive acceptance". F is called "fractional difference". This definition for the systematic error was chosen to reflect explicitly the dependence of the accuracy of the flux on data reproducibility by MC. All the fractional differences were summed in quadrature, and were weighted by the exclusive acceptance obtained with data.

The results of the systematic errors are summarized in Table 8.2. As can be seen in the table, the contribution from the CsI veto dominated the systematic uncertainty. Figure 8.8 shows the fractional differences of various kinematic cuts and veto cuts (The kinematic cuts for $K_L^0 \to \pi^0\pi^0$ are described in Appendix A). The acceptance loss of the CsI veto in the MC is much higher than in the data. There were three potential reasons that could contribute to the discrepancy in the CsI veto:

1. the energy scale error,

2. the treatment of the timing information,

3. non-linearities in the response which were not properly modeled.

The scale error could lead to more or less rejection. The timing information could be the reason because we used timing windows to minimize losses due to accidental activities. If we did not control accidental effects correctly, the time window caused the discrepancy in the behavior of the veto. Finally, the non-linearity would appear in the resolution, as represented in Equation 5.10. If we did not correctly match the resolution of the CsI to the single crystal level, the discrepancy would appear in the veto behavior, in particular for the low energy depositions where the constant term is dominant.

Table 8.2: Systematic errors for the K_L^0 flux based on $K_L^0 \to \pi^0\pi^0$

Cut	Pure MC Uncertainty	Add-BG Uncertainty
CsI Veto	6.2%	6.7%
$Z(K_L^0)$	2.3%	2.4%
R^2 at C6	1.7%	1.8%
CV Veto	1.3%	1.4%
Hit position(square ,radial)	1.2%	1.3%
24 Others	1.9%	1.8%
Total	7.3%	7.8%
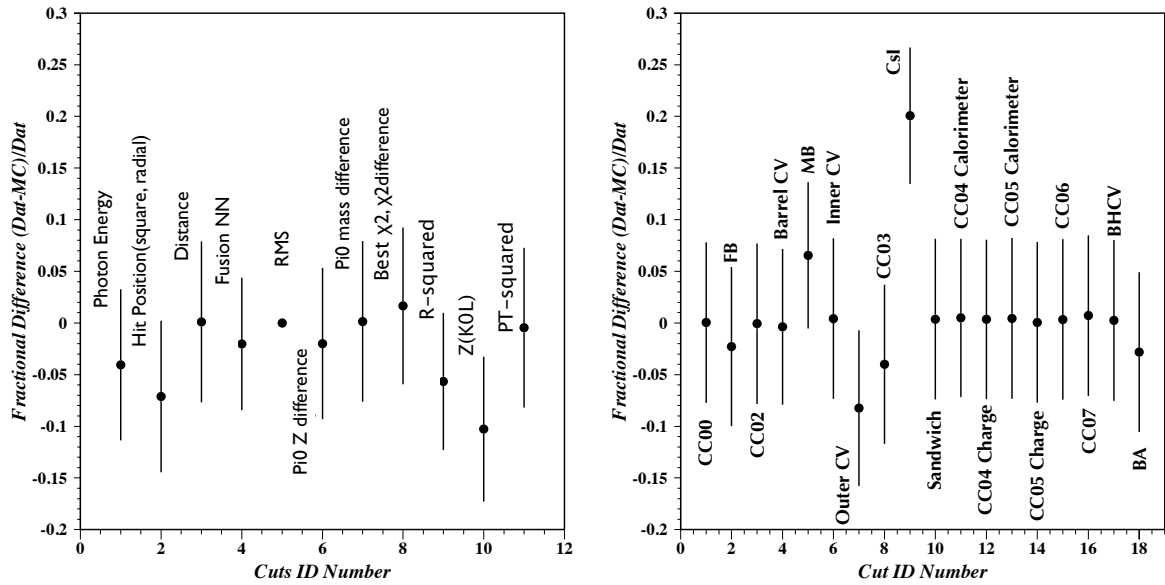
Figure 8.8: Differences in the exclusive acceptance fractions, (DATA-MC)/Data, for the Pure MC. A positive value indicates the acceptance loss was higher in the MC than in the data.

8.1.5 Decay Probability

We generated the K_L^0's in MC at the exit of C6 which is the downstream end of the collimator system. The standard signal region of the decay Z-vertex was determined to be 340–500 cm, where 0 cm was defined to be the front end of the FB. We generated $5 \times 10^5 K_L^0$ to calculate the K_L^0's decay probability in the signal region, and obtained 10713.8 decays within 340–500 cm with the weight described in Section 8.1.2. The decay probability was calculated to be $(2.14 \pm 0.02\%)$ where the error denotes the statistical uncertainty.

Table 8.3: Numbers of events in the invariant-mass regions by the MC and Data.

Sample	On Mass Region $(0.4814 < m < 0.5126$ GeV/$c^2)$	Side band
$K_L^0 \to \pi^0\pi^0$ MC	1494.9 ± 12.4	101 ± 3.2
$K_L^0 \to \pi^0\pi^0\pi^0$ MC	5.1 ± 4.9	75.6 ± 18.8
Total MC	1500 ± 13.3	176 ± 19.1
Data	1500	206

8.1.6 Results

We collected $K_L^0 \to \pi^0\pi^0\pi^0$, $K_L^0 \to \pi^0\pi^0$, $K_L^0 \to \gamma\gamma$ events in the data sample with 6, 4, 2 photon clusters, respectively, and obtained the K_L^0 flux independently from these three modes. Then, we decided to use the value with $K_L^0 \to \pi^0\pi^0$ for the K_L^0 flux because of its similar energy scale of the photons in the CsI calorimeter to $K_L^0 \to \pi^0\pi^0$. Figures 8.9, 8.10, and 8.11 are the distributions with 4 gamma cluster sample of the pairing χ_Z^2, momentum and Z-vertex, respectively. The Z-vertex distribution of the $K_L^0 \to \gamma\gamma$ event is shown in Figure 8.12. The MC distributions were well consistent with the data.

Figure 8.13 shows the invariant mass distribution reconstructed with 4 photon cluster sample of the data and MC. As seen in the figure, in addition to the events from $K_L^0 \to \pi^0\pi^0$, there were events from $K_L^0 \to \pi^0\pi^0\pi^0$ in the low mass region ($m_{4\gamma} \lesssim 0.43$ GeV/c^2) due to the photon inefficiency of two out of six photons in the final state. In the low mass region, there were also the events from $K_L^0 \to \pi^0\pi^0$, due to mis-pairing of the four photons in π^0 reconstruction. The sum of the contributions from $K_L^0 \to \pi^0\pi^0$ and $K_L^0 \to \pi^0\pi^0\pi^0$ MC had good agreement in the low mass tail and the mass peak region with data. The numbers of events in MC are summarized in Table 8.3; we defined the "on-mass region" as $0.4814 < m_{4\gamma} < 0.5126$ GeV/c^2 by $\pm 3\sigma$ of the peak distribution, and the outside as the "side band". We used the event in the on-mass region as the signal for the normalization in 6 and 4 cluster sample. We also required the reconstructed Z-vertex to be within 340–500 cm for all of the normalization modes.

We calculated the acceptance by using two ways: 1) Pure MC plus the accidental loss, 2) Add-BG MC, and obtained the consistent results. We also calculated the acceptance for $K_L^0 \to \pi^0\pi^0\pi^0$ and $K_L^0 \to \gamma\gamma$ decays. The results are summarized in Table 8.4.

Finally, the K_L^0 flux was computed as:

$$N_{decay} = \frac{N_{signal}}{A \times Br} \ , \tag{8.6}$$

where A and Br are the acceptance and the branching fraction for each normalization mode, respectively. The results of the flux for all the normalization modes are listed in Table 8.5. As mentioned before, we took the value obtained from $K_L^0 \to \pi^0\pi^0$ with the Pure MC as the number of K_L^0 decays in the signal region:

$$N_{decay} = (5.13 \pm 0.40) \times 10^9 \tag{8.7}$$

Figure 8.9: Distribution of the pairing χ^2_Z with the 4 clusters events. The dots show the data and the histograms show the contributions of $K^0_L \rightarrow \pi^0\pi^0$, $K^0_L \rightarrow \pi^0\pi^0\pi^0$ MC and their sum.

The discrepancy among the modes was thought to come from the treatment of accidental activities. It affected on the acceptance loss due to photon vetoes.

Note that, in the error for the flux, the uncertainty in the branching fraction ($Br(K^0_L \rightarrow \pi^0\pi^0) = (8.69 \pm 0.04) \times 10^{-4}$) [8] was included; its magnitude was only 0.46% and was negligible.

Table 8.4: Acceptance estimations for the normalization modes. The errors are statistical only.

Mode	Pure Accid. Loss	Pure MC Accept.	Add-BG Accept.
$K^0_L \rightarrow \gamma\gamma$	17.53%	$(6.93 \pm 0.03) \times 10^{-3}$	$(6.95 \pm 0.03) \times 10^{-3}$
$K^0_L \rightarrow \pi^0\pi^0$	17.50%	$(3.35 \pm 0.03) \times 10^{-4}$	$(3.35 \pm 0.03) \times 10^{-4}$
$K^0_L \rightarrow \pi^0\pi^0\pi^0$	17.11%	$(7.13 \pm 0.06) \times 10^{-5}$	$(7.02 \pm 0.06) \times 10^{-5}$

Table 8.5: Flux estimations obtained with three decay modes. The error indicates the total error and is dominated by the systematic uncertainty.

Mode	Pure MC Flux	Add-BG Flux
$K^0_L \rightarrow \gamma\gamma$	$(5.45 \pm 0.38) \times 10^9$	$(5.43 \pm 0.42) \times 10^9$
$K^0_L \rightarrow \pi^0\pi^0$	$(5.13 \pm 0.40) \times 10^9$	$(5.13 \pm 0.43) \times 10^9$
$K^0_L \rightarrow \pi^0\pi^0\pi^0$	$(5.02 \pm 0.35) \times 10^9$	$(5.10 \pm 0.40) \times 10^9$
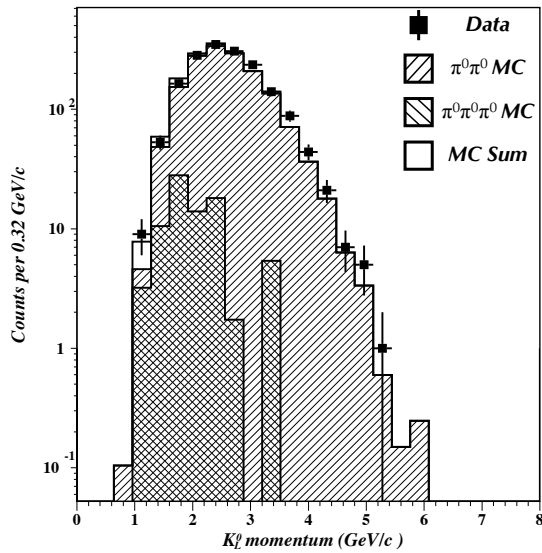
Figure 8.10: Distribution of the K_L^0 momentum with the 4 clusters events. The dots show the data and the histograms show the contributions of $K_L^0 \rightarrow \pi^0\pi^0$, $K_L^0 \rightarrow \pi^0\pi^0\pi^0$ MC and their sum.
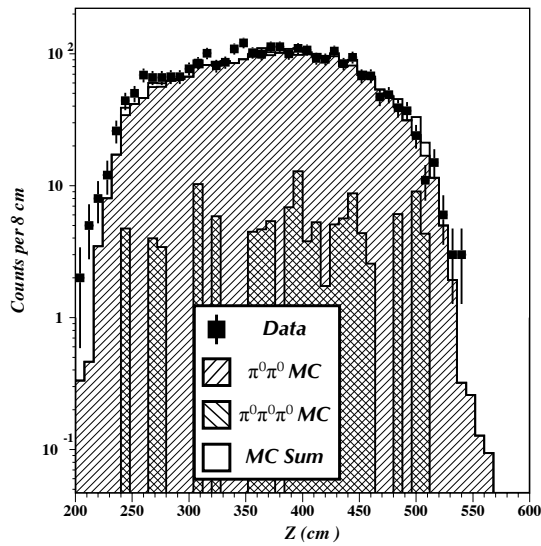
Figure 8.11: Distribution of the Z-vertex with the 4 cluster events. The dots show the data and the histograms show the contributions of $K_L^0 \rightarrow \pi^0\pi^0$, $K_L^0 \rightarrow \pi^0\pi^0\pi^0$ MC and their sum.
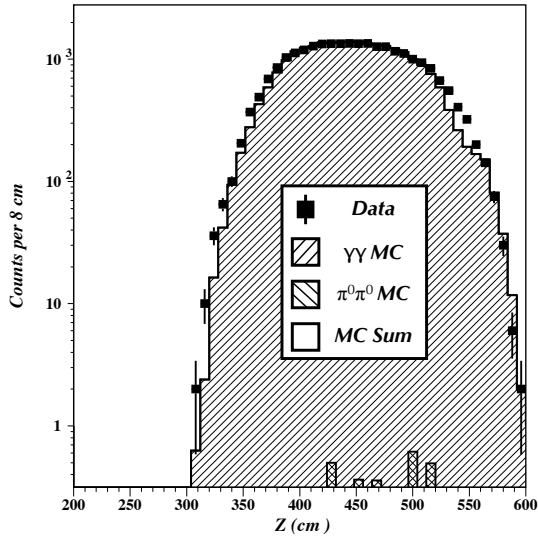
Figure 8.12: Distribution of the Z-vertex with the 2 cluster events for $K_L^0 \rightarrow \gamma\gamma$ assuming the K_L^0 mass. The dots show the data and the histograms show the contributions of $K_L^0 \rightarrow \gamma\gamma$, $K_L^0 \rightarrow \pi^0\pi^0$ MC and their sum.

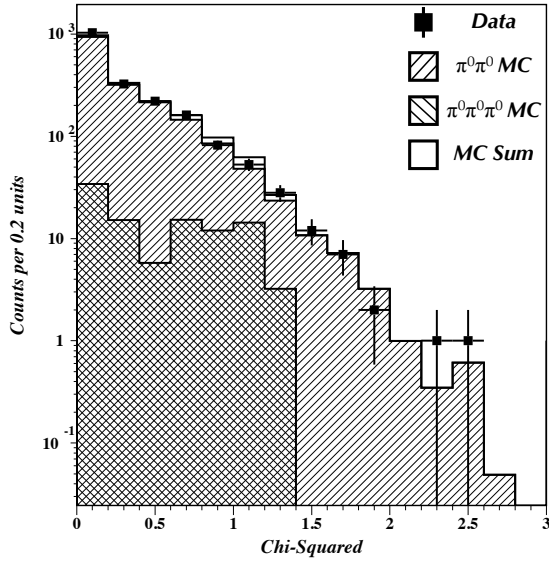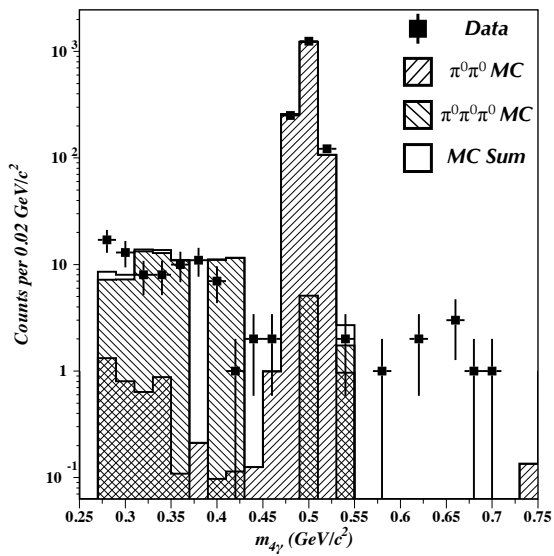**Figure 8.13:** Invariant mass distribution with the 4 cluster events. The dots show the data and the histograms show the contributions of $K_L^0 \rightarrow \pi^0\pi^0$, $K_L^0 \rightarrow \pi^0\pi^0\pi^0$ MC and their sum.

8.2 Acceptance for $K_L^0 \to \pi^0 \nu \bar{\nu}$

After tuning the K_L^0 distributions, as described in Section 8.1.2, we estimated the signal acceptance with the $K_L^0 \to \pi^0 \nu \bar{\nu}$ MC.

8.2.1 Timing Cuts

The signal acceptance was calculated on the basis of the standard selection cuts on the $K_L^0 \to \pi^0 \nu \bar{\nu}$ MC sample. Since the MC did not reproduce the timing distributions, TDI and Time-difference cuts were treated separately. We estimated the signal loss by TDI with the data of the $K_L^0 \to \pi^0 \pi^0 \pi^0$, $K_L^0 \to \pi^0 \pi^0$, and $K_L^0 \to \gamma\gamma$ events. The results are summarized in Table 8.6. We took the acceptance in $K_L^0 \to \pi^0 \pi^0$. The total acceptance by the TDI cut was 0.873, and the acceptance for each photon was calculated as $(0.873)^{1/4} = 0.967$. The TDI acceptance for $K_L^0 \to \pi^0 \nu \bar{\nu}$ was calculated as the square of single photon acceptance, to be 0.935.

The effect of the time difference cut was also estimated by $K_L^0 \to \pi^0 \pi^0$. We took the difference between the timings of the earliest photon and the second earliest one. We obtained 0.974 for the acceptance of this cut.

Table 8.6: Acceptance with the TDI cut. "All photons" means the acceptance by imposing the TDI cut for all the photons 2 for $K_L^0 \to \gamma\gamma$, 4 for $K_L^0 \to \pi^0 \pi^0$, and 6 for $K_L^0 \to \pi^0 \pi^0 \pi^0$. The acceptance for one photon was calculated as the n-th root of the acceptance for all(n) photons, where n denotes the number of photons in the event. The value in the right column shows the ratio of the obtained acceptance for one photon to that from $K_L^0 \to \pi^0 \pi^0$ events.

Mode	Acc. for all photons	Acc. for one photon	Ratio
$K_L^0 \to \gamma\gamma$	0.9598 ± 0.0014	0.9797 ± 0.0007	1.013
$K_L^0 \to \pi^0 \pi^0$	0.873 ± 0.008	0.967 ± 0.002	(1.0)
$K_L^0 \to \pi^0 \pi^0 \pi^0$	0.7717 ± 0.0016	0.9577 ± 0.0003	0.990

8.2.2 Result

We generated $5 \times 10^8 K_L^0$ at C6, forcing them to decay into $K_L^0 \to \pi^0 \nu \bar{\nu}$, and obtained 9.495×10^4 events in the signal region with the weight, without the timing cuts described above. Figure 8.14 shows the remaining events after imposing all the selection cuts. Considering the decay probability of 2.14% and the acceptance degradation due to the accidental loss of 0.8257, and the efficiencies with the timing cuts, the signal acceptance was calculated:

$$A_{signal} = \frac{9.495 \times 10^4}{(5 \times 10^8) \cdot 0.0214} \times 0.8257 \times 0.967^2 \times 0.974$$

$$= (0.670 \pm 0.003_{stat}) \times 10^{-2} . \tag{8.8}$$

The exclusive acceptances of the veto cuts and kinematic cuts were summarized in Table 8.7 and 8.8, respectively.
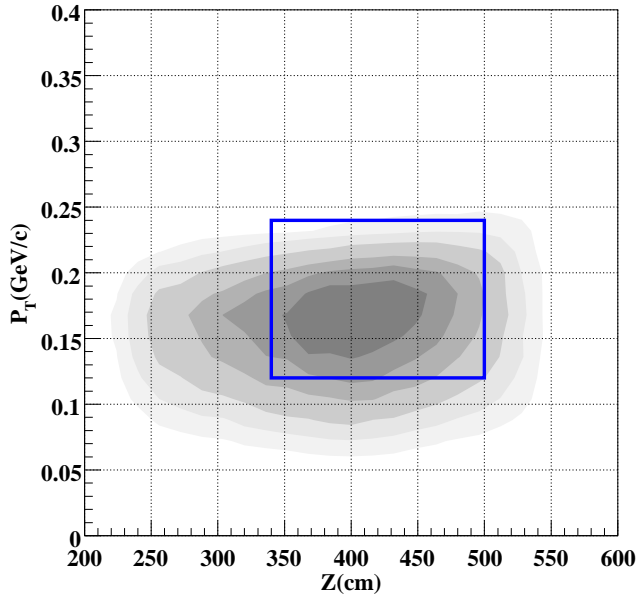
Figure 8.14: P_T vs. Z-vertex distribution with the $K_L^0 \to \pi^0 \nu \bar{\nu}$ signal MC. The blue box shows the signal region.

We simply introduced the same systematic error as computed for the normalization mode ($K_L^0 \to \pi^0 \pi^0$) of 7.3%. Because the systematic error was dominated by the CsI veto and it depended on the number of photons in the event, this was thought to be a conservative estimate.

Thus, the final expression for the acceptance was

$$A_{signal} = (0.670 \pm 0.003_{stat} \pm 0.049_{syst}) \times 10^{-2} \ . \tag{8.9}$$

8.3 Single Event Sensitivity

The single event sensitivity (SES) is the measure of the experimental sensitivity. It corresponds to the branching fraction with which the experiment is expected to observe one event, and is expressed by the equation:

$$\text{SES} = \frac{1}{\text{N}_{\text{decay}} \times \text{A}_{\text{signal}}} \ . \tag{8.10}$$

Substituting $N_{decay} = (5.13 \pm 0.40) \times 10^9$ and $A_{signal} = (0.670 \pm 0.049) \times 10^{-2}$, we obtained SES to be

$$\text{SES} = (2.91 \pm 0.31) \times 10^{-8} \ , \tag{8.11}$$

where the error contains both statistical and systematic uncertainties.

Table 8.7: Acceptance by the veto cuts for $K_L^0 \rightarrow \pi^0 \nu \bar{\nu}$. The acceptances were obtained using the Pure MC. The accidental loss is not included in these values.

Detector	Acceptance
CC00	1.0
FB	0.9962
CC02	1.0
BCV	0.9441
MB	0.8309
CV	0.9538
CC03	0.9973
CsI	0.6306
Sandwich	0.9977
CC04	0.9681
CC05	0.9961
CC06	0.9975
CC07	0.9995
BHCV	1.0
BA	1.0

Table 8.8: Acceptance by the kinematic cuts for $K_L^0 \rightarrow \pi^0 \nu \bar{\nu}$. The acceptances were obtained using the Pure MC.

Cut	Acceptance
Photon Energy	0.9996
Cluster Size 5 MeV	0.9079
Crystal Size 1 MeV	0.9349
Energy Ratio	0.9970
Photon TDI	0.967
Photon RMS	0.5667
Hit Position (square)	0.8823
Hit Position (radial)	0.9996
Distance	1.0
Timing Difference	0.974
Energy Balance	0.9972
π^0 Kinetic Energy	1.0
$\sum \Delta \theta \chi^2$	0.8616
Acoplanarity Angle	0.9763
π^0-Projection	0.8944
Missing Momentum	0.8616

Chapter 9

Background Estimation

This chapter describes the estimation of the background level. Since we employed the blind analysis, it was essential to estimate the background level without seeing events inside the blind region. In addition, comparing theoretical predictions of the $K_L^0 \to \pi^0 \nu \bar{\nu}$ branching fraction and our single event sensitivity, we prepared for the case that no signal events were there, and we chose the event selection to suppress the background level sufficiently low. Thus, we needed the background estimation to the level of $O(10^{-1})$ event.

9.1 Kaon Backgrounds

In order to estimate the backgrounds from the K_L^0 decays, we produced the MC samples for several K_L^0 decay modes which were thought to cause backgrounds. Their statistics are summarized in Table 9.1. $K_L^0 \to \pi^0 \pi^0 \pi^0$ is not included in the table because the background level we roughly estimated was less than 10^{-3} of $K_L^0 \to \pi^0 \pi^0$ due to two more extra photons. In the major charged decay modes, we describe the result of the background estimation only for $K_L^0 \to \pi^- e^+ \nu$ and $K_L^0 \to \pi^+ \pi^- \pi^0$ because the others do not make the photon clusters in the final states, and thus could not be the background source.

The background level estimation was based on the numbers of the remaining events after imposing the cuts.

9.1.1 $K_L^0 \to \pi^0 \pi^0$

In Figure 9.1, we show the P_T vs. Z-vertex plots for the $K_L^0 \to \pi^0 \pi^0$ MC events after imposing the group of veto cuts only and the group of kinematic cuts only, respectively. From those plots, we found the veto cuts were effective to remove the higher P_T component, and the kinematic cuts were effective to remove the lower P_T component. These facts could be understood as follows. In the higher P_T region, the "even" backgrounds were dominant, which were defined as events in which both two photons came from one of the two π^0's. For them, the veto cut set was the only tool to reduce the backgrounds. In the lower P_T region, the "odd" backgrounds dominated, in which two photons came from different π^0's. For them, the kinematic cut set was effective since they were not reconstructed with correct kinematic variables.

Table 9.1: Statistics of the MC sample used for the background estimation. In the generation of each mode, K_L^0's were forced to decay into the specific mode. The equivalent "sample size" indicates the comparison of the effective number of K_L^0 decays in MC with the collected number of K_L^0 decays in the experiment (5.13×10^9).

Mode	K_L^0 at C6	Decays in the Fiducial	Branching Fraction	Sample Size
$K_L^0 \to \gamma\gamma$	5×10^8	10.7×10^6	$(5.48 \pm 0.05) \times 10^{-4}$	$\times 3.8$
$K_L^0 \to \pi^0\pi^0$	2×10^9	42.8×10^6	$(8.69 \pm 0.04) \times 10^{-4}$	$\times 9.6$
$K_L^0 \to \pi^- e^+ \nu$	1×10^9	21.4×10^6	$(20.27 \pm 0.08)\%$	2.1%
$K_L^0 \to \pi^+\pi^-\pi^0$	2×10^9	42.8×10^6	$(12.56 \pm 0.05)\%$	6.6%

With all the cuts imposed, only one event remained in the signal region from the $K_L^0 \to \pi^0\pi^0$ MC with the sample of 9.6 times larger than the data. We obtained the weight factor for the event of 1.16 by the weight function for the MC tuning explained in Section 8.1.2. Thus, we estimated the background level to be:

$$N_{bg}(K_L^0 \to \pi^0\pi^0) = 1/9.6 \times 1.16 = 0.12 \pm 0.12 , \qquad (9.1)$$

where the error was taken based on 1 ± 1 remaining event.

Even though it is difficult to characterize background topologies, we studied the topology of "the" event. It was an "even" event in which two extra photons were missed. One of them, with the energy of 14 MeV, was missed in MB due to the sampling effect. The other photon entered the CsI calorimeter (not a gap between crystals) and punched through without interaction. The radiation length of the CsI crystals were $16X_0$, and the probability of the punch-through effect was estimated to be 1×10^{-7}.

It turned out that the CsI calorimeter and MB were the most responsible components for detecting extra photons and rejecting the $K_L^0 \to \pi^0\pi^0$ backgrounds, as shown in Table 9.2. To verify the detection inefficiency of the detectors in MC, we used the 4 clusters events. in which $K_L^0 \to \pi^0\pi^0\pi^0$ with two missing photons became a contamination to the $K_L^0 \to \pi^0\pi^0$ events . The tail in the lower mass region in the $M_{4\gamma}$ distribution, which were due to the photon inefficiencies, were well-reproduced by MC as shown in Figure 8.13.

Table 9.2: Background levels for $K_L^0 \to \pi^0\pi^0$ exclusive cut sets.

Cut Set	Background Events	Rejection
All Cuts	0.12 ± 0.11	(1)
w/o CsI	0.38 ± 0.20	3.13
w/o MB	0.81 ± 0.29	6.66
w/o RMS	0.16 ± 0.13	1.3
w/o All Kinematic Cuts	0.16 ± 0.13	1.3
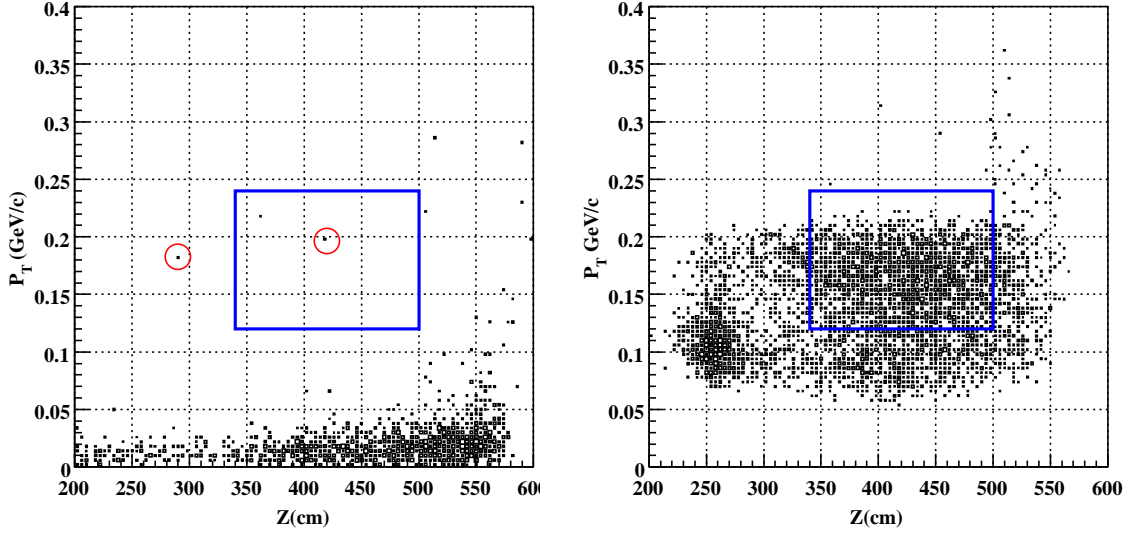
Figure 9.1: P_T vs. Z-vertex distributions of the $K_L^0 \to \pi^0\pi^0$ MC events after imposing the photon veto cuts (left) and the kinematic cuts (right). Red circles in the left figure show the events remaining after imposing all the cuts.

9.1.2 $K_L^0 \to \gamma\gamma$

Figure 7.12 shows the events after imposing the veto cuts on the MC sample of the $K_L^0 \to \gamma\gamma$ decay. No events remained in the signal box with 3.8 times larger statistics than data. In addition, by imposing only the kinematic cuts, all the events were removed not only in the signal box but in all the region. We evaluated the rejection power of the acoplanarity angle cut for $K_L^0 \to \gamma\gamma$ was about 1.6×10^5, and estimated the background level to be less than 3.9×10^{-6} events. We concluded the $K_L^0 \to \gamma\gamma$ background was negligible.

9.1.3   Charged Decay Modes

Since the branching fractions of $K_L^0 \to \pi^- e^+ \nu$ and $K_L^0 \to \pi^+\pi^-\pi^0$ are large, it was difficult to prepare enough MC statistics to be comparable to the number of K_L^0 decays in the data. Thus, we estimated their background level without imposing charged vetoes in the simulation. The inefficiencies of the vetoes were used as event weights when charged particle(s) passed through charged veto counters. We used the values for inefficiencies with conservative estimation to be 10^{-4} for CV, 10^{-3} for BCV, and 10^{-3} for BHCV [53].

Figure 9.3 shows the events by imposing all the cuts except the veto by CV on the MC sample of the $K_L^0 \to \pi^- e^+ \nu$ decay. We obtained 739.9 events in the signal region of the plot with the two charged particles hitting CV. We calculated the background level for $K_L^0 \to \pi^- e^+ \nu$ by including the suppression of CV $(10^{-4})^2$ on the number of the remaining events. After taking the normalization for the MC statistics (2.1%) of data, the background level was estimated to be 3.5×10^{-4} events.

For $K_L^0 \to \pi^+\pi^-\pi^0$, we obtained the background level of 2.5×10^{-5} events with the similar method. We concluded the these backgrounds were negligible.
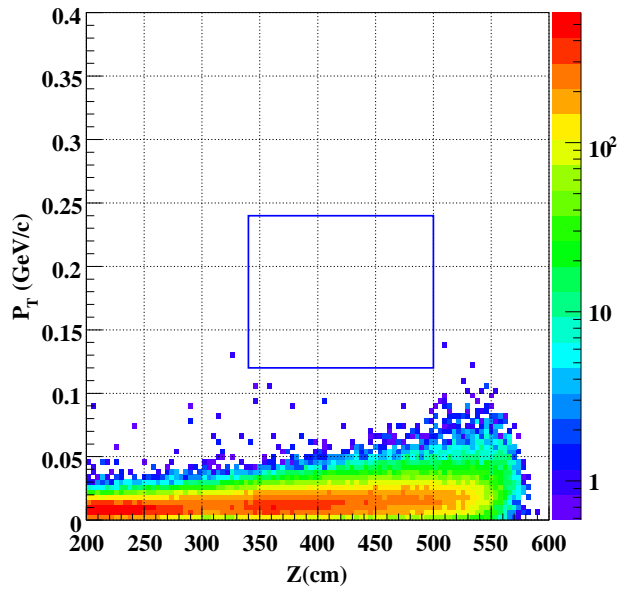
Figure 9.2: P_T vs. Z-vertex distribution of the events in the $K_L^0 \to \gamma\gamma$ MC after imposing only the veto cuts.
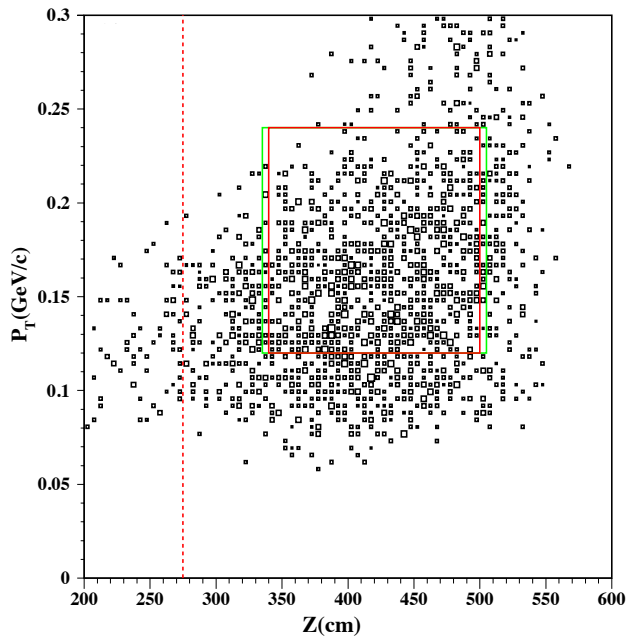
Figure 9.3: P_T vs. Z-vertex distribution in the $K_L^0 \to \pi^- e^+ \nu$ MC after imposing all the cuts except the veto by CV.

9.2   Neutron Backgrounds

9.2.1   CC02 Events

CC02 events came from halo neutron interactions with the CC02 materials which produce π^0's.

   As described in Section 7.1, we used the data taken in the Al plate run to estimate the CC02 background events especially for the tail in the reconstructed Z_{vtx} distribution. The production position of π^0's was different between the physics run and the Al plate run:

1. the position of the object; Z(Al plate) $= Z$ (CC02) $+6.5$ cm,

2. the distribution of the production position; The size in z-direction was 0.5 cm for the Al plate, 30 cm for CC02.

To discuss the Z_{vtx} distribution i nthe physics run, we applied corrections on the Z_{vtx} distribution in the Al plate run. We subtracted the offset of 6.5 cm from the original Z-vertex value in the Al plate run, and applied a smearing function to simulate the Z_{vtx} distribution in CC02 as:

$$Z_{cor} = Z_{orig} - 6.5 - \Delta Z_{smear} , \tag{9.2}$$

where Z_{cor} is the corrected Z-vertex and Z_{orig} is the original position from the data in the Al plate run. ΔZ_{smear} was a random number from an exponential deviate: $\exp[-t/(6.0 \text{ cm})]$, where the slope of 6.0 cm was determined to adjust the width of the Z-vertex distributions. Figure 9.4 shows the result of the event distribution in the Al plate run with the correction.

   We divided the region in the Z direction into (I) $200 < Z < 300$ cm, (II) $300 < Z < 340$ cm, and (III) $340 < Z < 500$ cm, and used (I) for the normalization to the real data. Then, we examined the region (II), as the "control" region, in order to validate the background estimation.

   We also checked the π^0's momentum and P_T distributions by using the events in the region (I) and (II), as shown in Figure 9.5. The distributions in the physics run and in the Al plate run agreed well each other. This demonstrated the validity of our method.

   Figure 9.6 shows the projected Z-vertex distribution, and Table 9.3 summarizes the number of events observed in the physics run and the Al plate run. In the control region, the expected number of events from the data in Al plate run was 1.9 ± 0.2 and it was consistent with the number of the observed events in the physics run of 3. The background estimation of the CC02 events was

$$N_{bg}(\text{CC02}) = 9 \times (120/6824) = 0.16 \pm 0.05 , \tag{9.3}$$

where the error was statistical only.

Table 9.3: Numbers of events in the CC02 background in the physics run and the Al plate run. The background level was estimated by normalizing the events within Z=[200,300]. The errors were calculated by Poisson statistics with the numbers of the events.

Z Region	Physics Run	Al Plate Run	Background
[200,300] cm	120	6824	(120)
[300,340] cm	3	106	1.9 ± 0.2
[340,500] cm	*masked*	9	0.16 ± 0.05
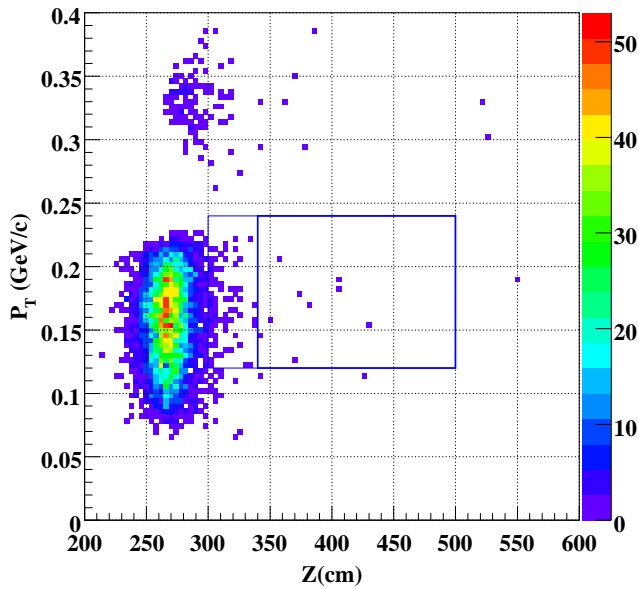
Figure 9.4: Single π^0 events in the Al plate run with all the cuts imposed.
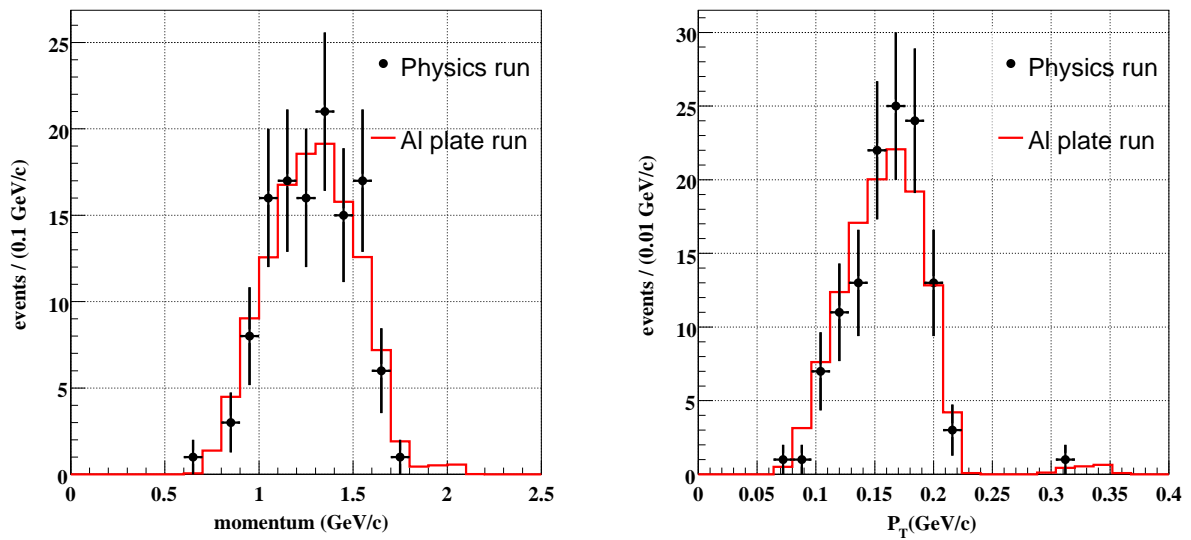
Figure 9.5: Momentum (left) and P_T (right) distributions of the CC02 events. The points show the data in the physics run, and the histogram is the distribution obtained from the Al plate run.
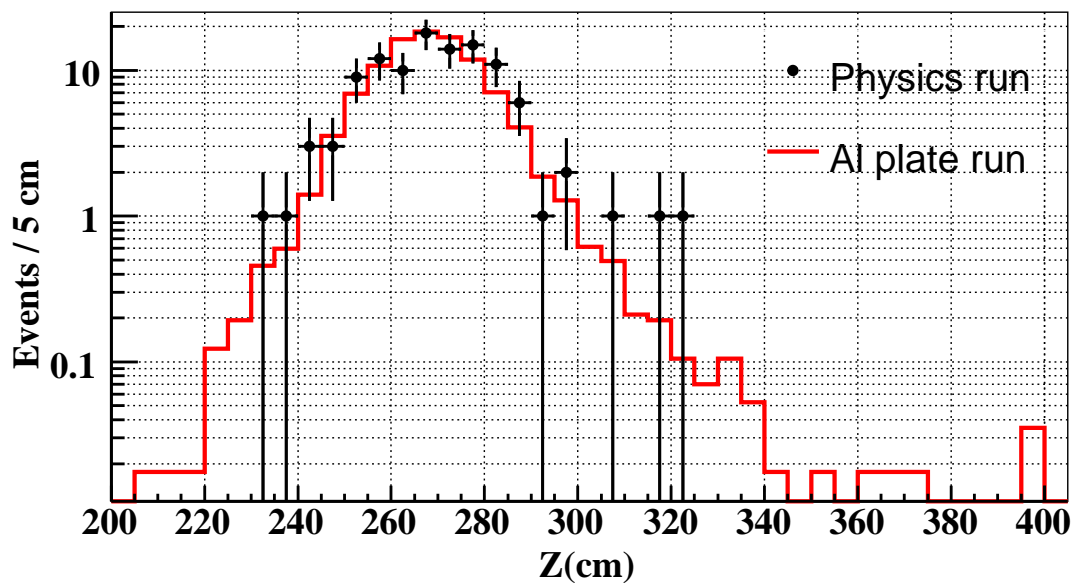
Figure 9.6: Reconstructed Z vertex distribution of the CC02 events with the P_T region as the signal region ($0.12 < P_T < 0.24$ GeV/c). The points show the data in the physics run and the histogram is the distribution from the Al plate run. The region above $Z = 340$ cm was masked for the physics run data.

9.2.2 Charged Veto Events

CV-π^0 Background

CV-π^0 background was defined as the events in which the halo neutrons hit the Charged Veto (CV) and produced π^0's. In order to estimate the background level from the events, we used the MC sample obtained by generating the halo neutrons according to the distribution of the beam line simulation. Since it took long computing time to produce the sample with the full simulation including the hadronic interactions, we produced the MC sample whose equivalent statistics was only $\times 0.506$ of the data in the physics run.

In Figure 9.7, the left plot shows the event distribution of the CV-π^0 events by the halo neutron MC, after imposing only the kinematics cuts. The right plot shows the Z-vertex distribution of the data and CV-π^0 events by MC with all the cuts. In this plot, we obtained 17 events remaining in the data and 18.2 ± 6.1 events in MC, and these numbers were consistent. However, there was no event in the signal box in MC with all the cuts imposed, and we could only set the upper limit of the background of 4.6 events.

In order to solve this problem, we applied a "bifurcation method" to the halo neutron MC. This method was employed in the analysis of E391a Run-I 1week data, and we found it worked well for the π^0 production events in the downstream material around CV [35]. Detailed description of the method is found in the reference [54].

Figure 9.8 illustrates the parameter space of the cuts. $N_{A\overline{B}}$, for example, means the number of events which passed through the cut set A but were rejected by the cut set B. N_{AB} indicates the number of background events after imposing all the cuts.
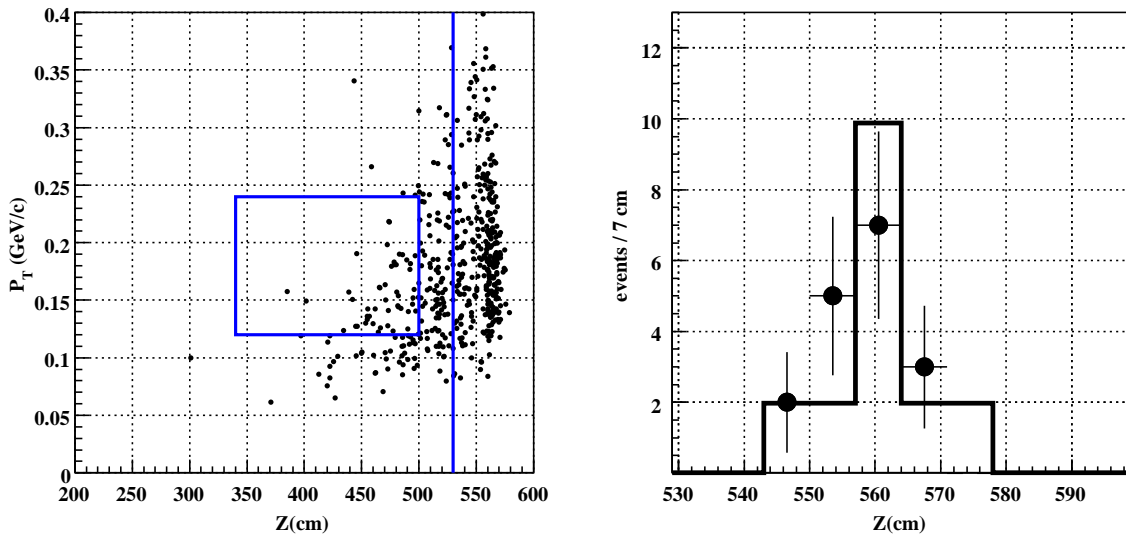
Figure 9.7: (Left) P_T vs. Z-vertex distribution of the events in which at least one π^0 was produced in CV and the kinematic cuts were imposed. (Right) Z-vertex distribution at CV with the halo neutron MC with all the cuts imposed. The dots show the data and the histogram shows the distribution from the halo neutron MC.

Cut B
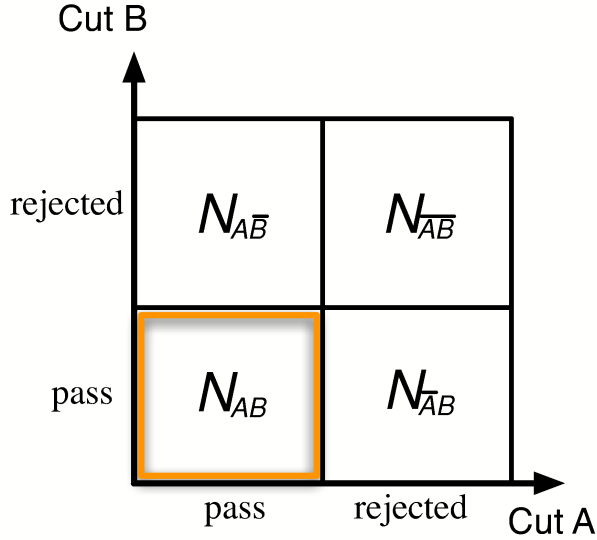
Figure 9.8: Schematic diagram of the background estimation in the bifurcation method.

When the cut A and B are independent, the ratio of $N_{AB}/N_{A\overline{B}}$ and $N_{\overline{A}B}/N_{\overline{A}\overline{B}}$ should be equal. Thus, the background level N_{AB} can be represented as:

$$N_{bg} = N_{AB} = \frac{N_{A\overline{B}} \cdot N_{\overline{A}B}}{N_{\overline{A}\overline{B}}} \ . \tag{9.4}$$

In the estimation of the CV-π^0 background, we selected the groups of the cuts as follows:

- A: veto cuts,

- B: photon quality cuts + two photon cuts,

- setup cuts: π^0 cuts.

Here the "setup cuts" are the cuts should be imposed before applying the bifurcation method.

We obtained $N_{A\overline{B}} = 54$, $N_{\overline{A}\overline{B}} = 4050$, and $N_{\overline{A}B} = 3$ with the halo neutron MC. With the normalization factor F_{norm} of $1/0.506$, we estimated the background level to be

$$N_{bg}(\mathrm{CV}-\pi^0) = \frac{3 \times 54}{4050} \times F_{norm} = 0.08 \pm 0.05 \ . \tag{9.5}$$

where the error was statistical only.

CV-η Background

As described in Section 5.3.1 and 7.1.2, we developed a special MC to estimate the background from η's produced at CV (CV-η events). Since the η production cross section is not implemented in GEANT3, we imported relevant parts of the geometry of the detector, such as CV and CsI, into a GEANT4 framework and ran a special MC.

Once η was produced, we collected the information of all the particles produced in the interaction in order to reproduce the veto effect with those extra particles. We discarded the photons with their energy
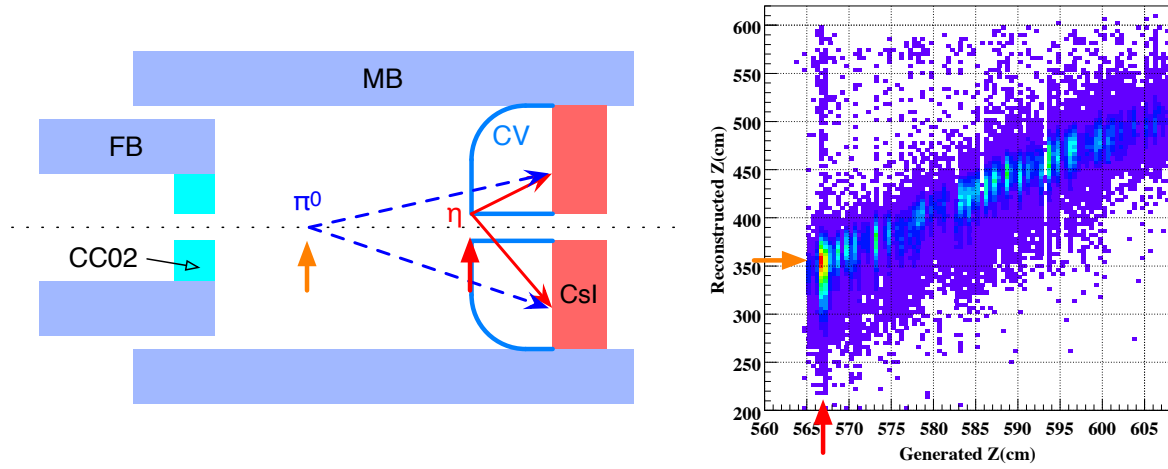
Figure 9.9: Correlation of the η production and the reconstructed positions. In the right plot, the horizontal axis shows the position of the η generation in MC, and the vertical axis shows the Z_{vtx} position of the reconstruction assuming the π^0 mass. No cuts were imposed on the events in the right plot. The arrows in both the figures show the same position.

less than 40 MeV, and protons and neutrons with their momentum less than 0.395 GeV/c in order to avoid the influence from rather slow phenomena such as photon emission from the nuclear excitation and the nucleus evaporation, which were expected to occur out of the event timing window, while they simultaneously occurred in GEANT4.

Figure 9.9 shows the events of η production at CV with this MC method. When η's were reconstructed by assuming that the invariant mass of two photons was m_{π^0}, they could enter the signal region.

In order to validate this MC, we first attempted to reproduce the invariant mass spectrum in the Al plate run. Figure 9.10 shows the result of the comparison of the invariant mass distributions by assuming that the reconstructed particles were generated and decayed at the Z position of the Al plate. We normalized the π^0 and η MC events by using the number of protons hitting the target (POT) from the beam line simulation, and obtained good agreement. In addition, we checked the momentum and P_T distributions with the events in the invariant mass region of $m > 0.52$ GeV/c^2 where η's dominated. They were found to be well-reproduced, as shown in Figure 9.11. Thus, we concluded that the cross section of the η production was reproduced in GEANT4. Note that the momentum distributions of the halo neutrons and the core neutrons were different and the momentum-dependence of the η production cross section in GEANT4 was not checked; however, as can be seen in Figure 5.1, the momentum distributions were similar above 2 GeV/c. Since the η production threshold is 1.8 GeV/c, there expected to be no radical dependence in the simulation.

Developing the new cuts, such as π^0-projection and $\Delta\theta\chi^2$, to reduce the η background to an acceptably low level, we generated η's in CV of 2.79×10^{20} POT equivalent, while the POT of the real data was 1.41×10^{18}. We set the normalization factor F_{norm} with these numbers including the accidental
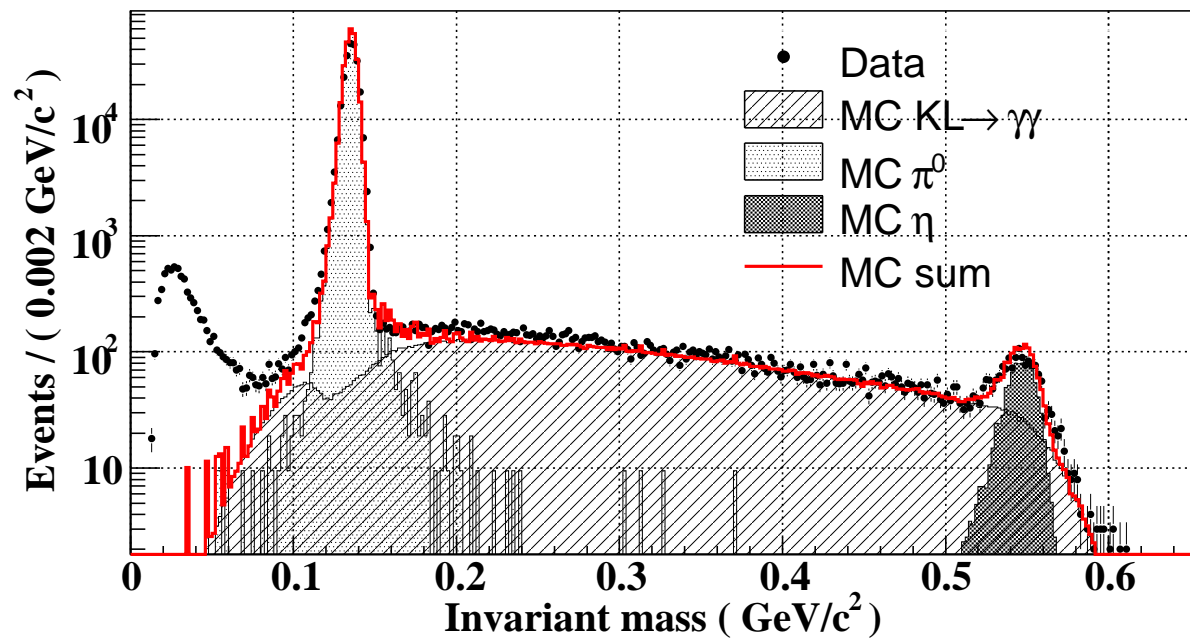
Figure 9.10: Reconstructed invariant mass distribution of the two photon events in the Al plate run. Dots show the data. Histograms indicate the contributions from $K_L^0 \to \gamma\gamma$ decays, π^0 and η production, and their sum, estimated by MC. Events in the low mass region were considered to be due to neutron interactions accompanying neither π^0's nor η's, which were not recorded in MC.
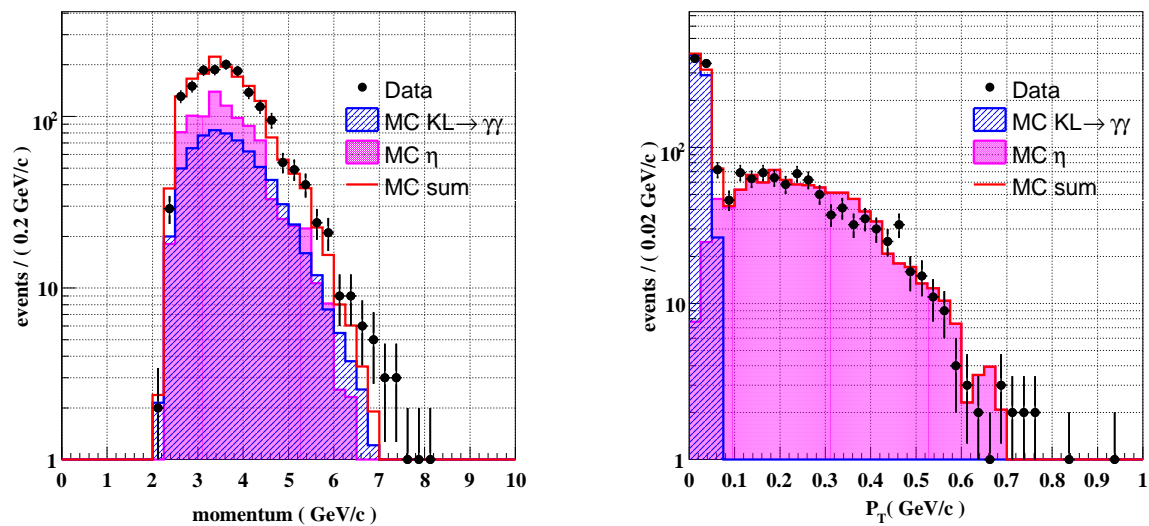
Figure 9.11: Momentum and P_T distributions of the reconstructed particles with the invariant mass above the 0.52 GeV/c^2, assuming that their Z-vertex was located at the Al plate
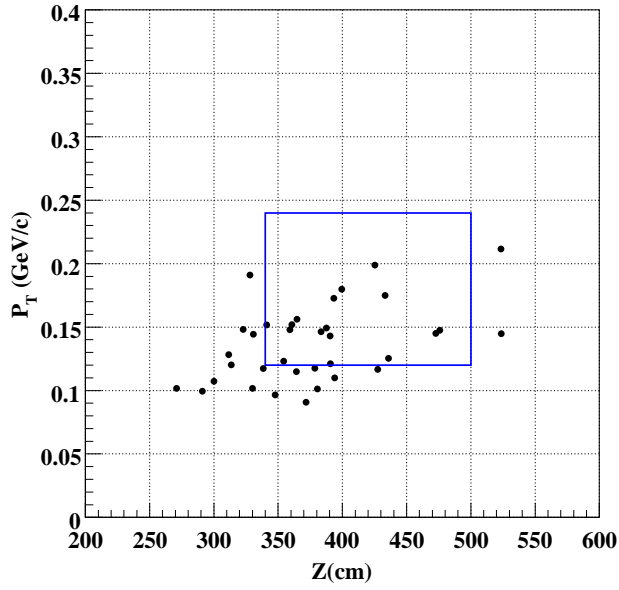
Figure 9.12: P_T vs. Z-vertex distribution with the MC sample of η produced at CV with all the cuts imposed.

loss and the acceptance of TDI cut and the timing difference cut:

$$F_{norm} = (1.41 \times 10^{18})/(2.79 \times 10^{20}) \times 0.8257 \times 0.967^2 \times 0.974$$

$$= 3.8 \times 10^{-3} . \tag{9.6}$$

In Figure 9.12, there were 16 events remaining in the signal region after imposing all the cuts. Thus, we estimated the background level to be

$$N_{bg}(\text{CV}-\eta) = 16 \times F_{norm} = 0.06 \pm 0.02 . \tag{9.7}$$

where the error was statistical only.

9.2.3   Background Rejection

Here we summarize the rejection power of the cuts for the neutron backgrounds. In Figure 9.13, we show the background rejection in the veto cuts, as compared to the exclusive acceptance for the $K_L^0 \to \pi^0 \nu \bar{\nu}$ MC. As in the case of the $K_L^0 \to \pi^0 \pi^0$ background, MB and CsI were effective to veto the extra particles in the hadronic interaction with the neutrons. CV was also effective to CV-π^0 background. There was no rejection of CV for the CV-η background because we checked the energy deposition in CV in the η production in MC, and rejected the events with the energy above the veto threshold beforehand.

Figure 9.14 shows the rejection and the signal acceptance in the kinematic cuts. As we explained in Section 7.3, some cuts were effective for the CV backgrounds. CC02 background was difficult to reject in the kinematic cuts, while the missing momentum cut had relatively large rejection power for the CC02 background.
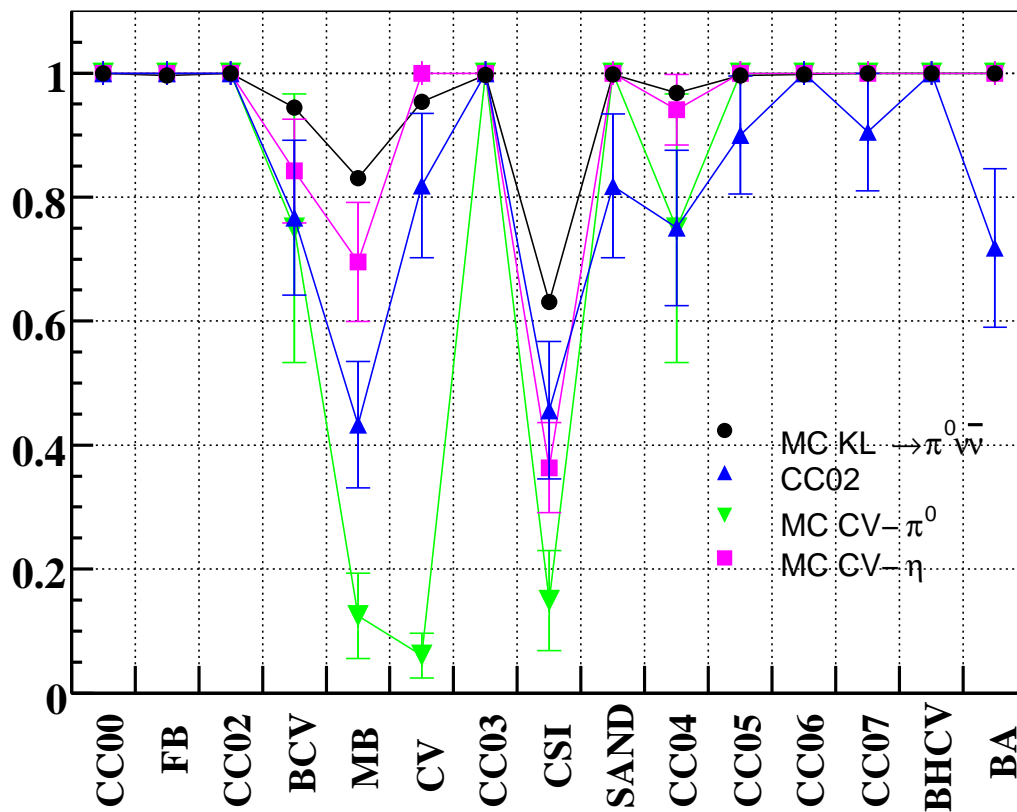
Figure 9.13: Vectors comparing the exclusive acceptance of the $K_L^0 \to \pi^0 \nu \bar{\nu}$ MC to the rejection for the neutron backgrounds in each veto cut. The effect of the accidental loss was not included in the vectors. The errors were statistical only.
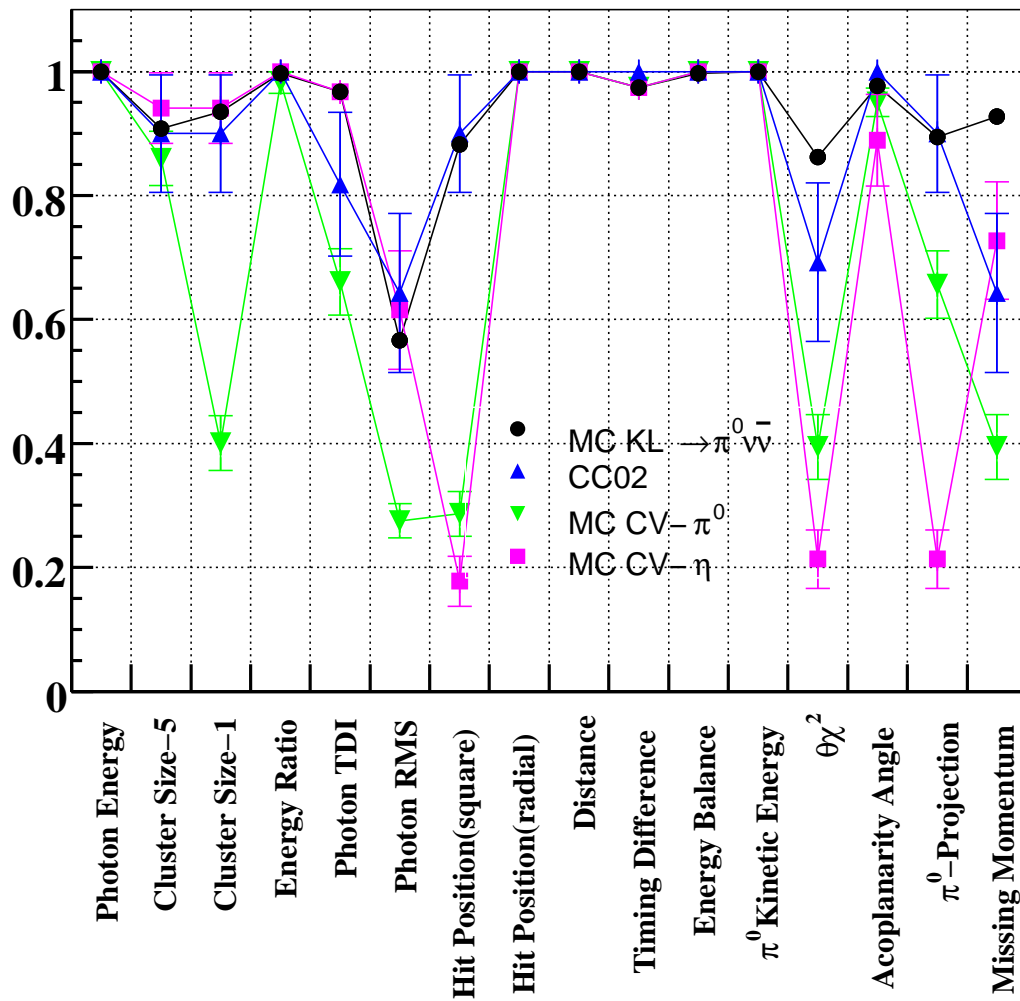
Figure 9.14: Vectors comparing the exclusive acceptance of the $K_L^0 \to \pi^0 \nu \bar{\nu}$ MC to the rejection for the neutron backgrounds in each kinematic cut. The errors were statistical only.

9.3 Summary

Figure 9.15 shows the events in the physics run with all the cuts imposed. Table 9.4 summarizes the background estimations. The errors for the predictions were dominated by the statistical uncertainty due to the low statistics. We defined the indices of the region around the signal region as:

1. $300 < Z < 340$ cm and $0.12 < P_T < 0.24$ GeV/c,

2. $340 < Z < 400$ cm and $0.12 < P_T < 0.24$ GeV/c,

3. $400 < Z < 500$ cm and $0.12 < P_T < 0.24$ GeV/c,

4. $300 < Z < 500$ cm and $P_T < 0.12$ GeV/c,

in order to clarify the Z-vertex-dependence of contributions from the several background sources.

We obtained the background of 0.42 ± 0.14 in total. This corresponds to the probability of null background event observation of 0.657 with Poisson statistics. One or two events appearance would be consistent with the background prediction within two standard deviation as shown in Table 9.5

Table 9.4: Predicted and observed backgrounds in the region around the signal box. The indices of the region are graphically shown in Figure 9.15.

Region	1	**2**	**3**	**2+3**	4
$K_L^0 \to \pi^0\pi^0$				0.12 ± 0.12	
CC02	1.9 ± 0.2	0.11 ± 0.04	0.05 ± 0.03	0.16 ± 0.05	0.26 ± 0.07
CV-π^0	0	0	0.08 ± 0.05	0.08 ± 0.05	0.09 ± 0.04
CV-η	0.02 ± 0.01	0.04 ± 0.02	0.02 ± 0.01	0.06 ± 0.02	0.04 ± 0.01
Total	1.9 ± 0.2			0.42 ± 0.14	0.39 ± 0.08
Observed	3	*masked*			2

Table 9.5: Probability to observe events in the signal region from the background estimation.

Number of Events	Prob.
0	0.657
1	0.276
2	0.058
≥ 3	0.009
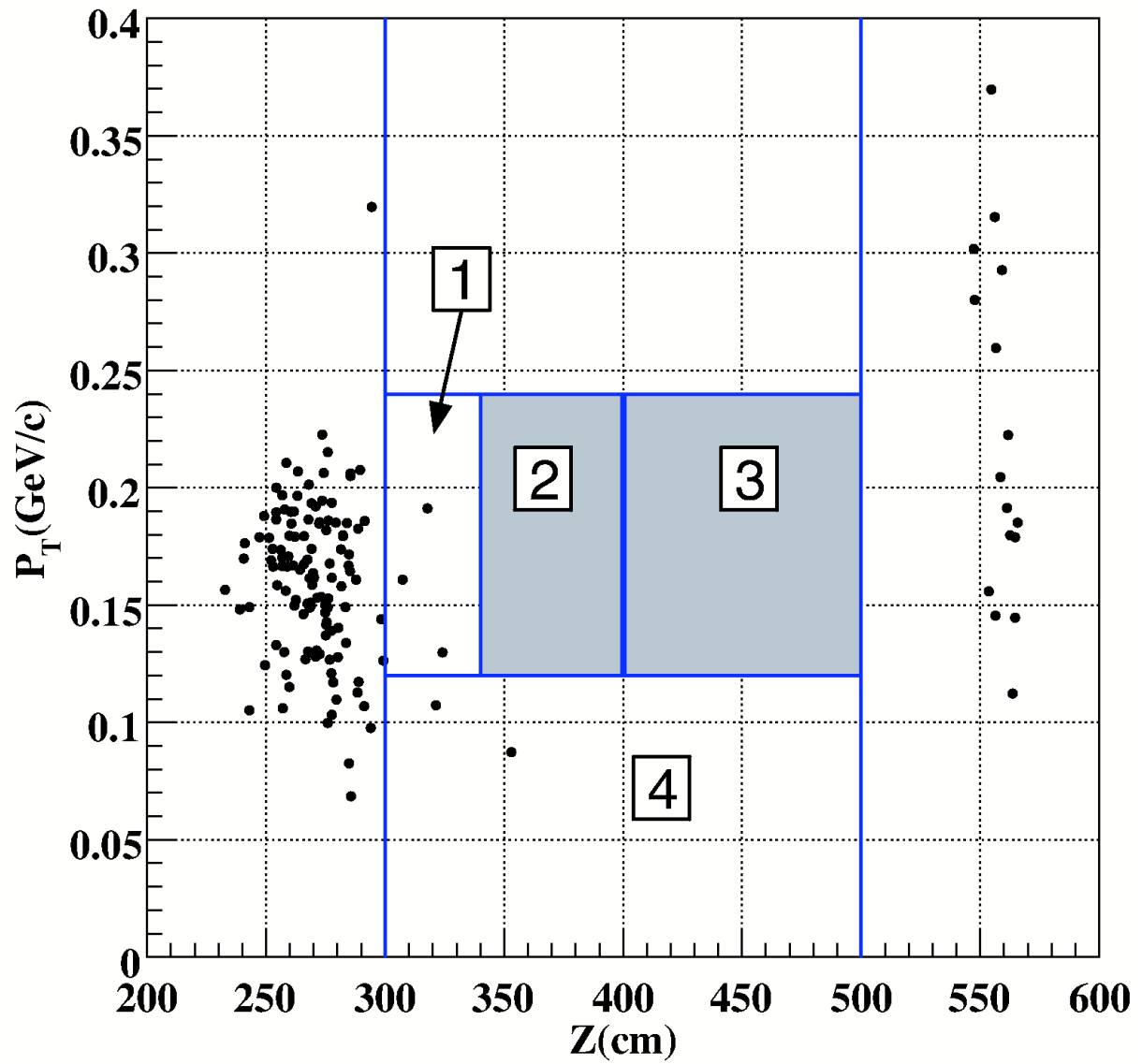
Figure 9.15: P_T vs. Z-vertex distribution in the physics run with the masked signal region.

Chapter 10

Result and Discussion

In this chapter, we present the results of our $K_L^0 \to \pi^0 \nu \bar{\nu}$ search. We have described all the cuts imposed on data, the systematic uncertainty and the estimations of the background level so far, which should be prepared before opening the masked signal region, according to the blind analysis manner.

In Section 10.1, we finally show the event inside the signal box. After opening the box, we give the results on the branching ratio with the number of observed events in the signal region in Section 10.2.

At last, we discuss the prospect of future $K_L^0 \to \pi^0 \nu \bar{\nu}$ experiment in Section 10.3.

10.1 Opening the Signal Box

With the background estimation of 0.42 ± 0.14 events, we finally opened the signal box. Figure 10.1 shows the P_T vs. Z-vertex distribution of the final events with the data by imposing all the cuts.

We observed no events in the signal region. This was the most probable, as indicated in Table 9.5, when no contribution existed other than the estimated background.

10.2 Result

As described in Section 8.3, the single event sensitivity (SES) was obtained to be $(2.91 \pm 0.31) \times 10^{-8}$. With no events observation, we set the upper limit of the branching ratio based on the Poisson statistics[1]. We obtained the upper limit on the branching fraction of $K_L^0 \to \pi^0 \nu \bar{\nu}$ to be:

$$Br(K_L^0 \to \pi^0 \nu \bar{\nu}) < 6.69 \times 10^{-8} \ , \tag{10.1}$$

at the 90% confidence level (C.L.). By this search, we improved the upper limit on the branching ratio from the past limit in E391a Run-I by a factor 3.1.

---

[1]Other statistical models and incorporating the systematic uncertainties are discussed in Appendix C.
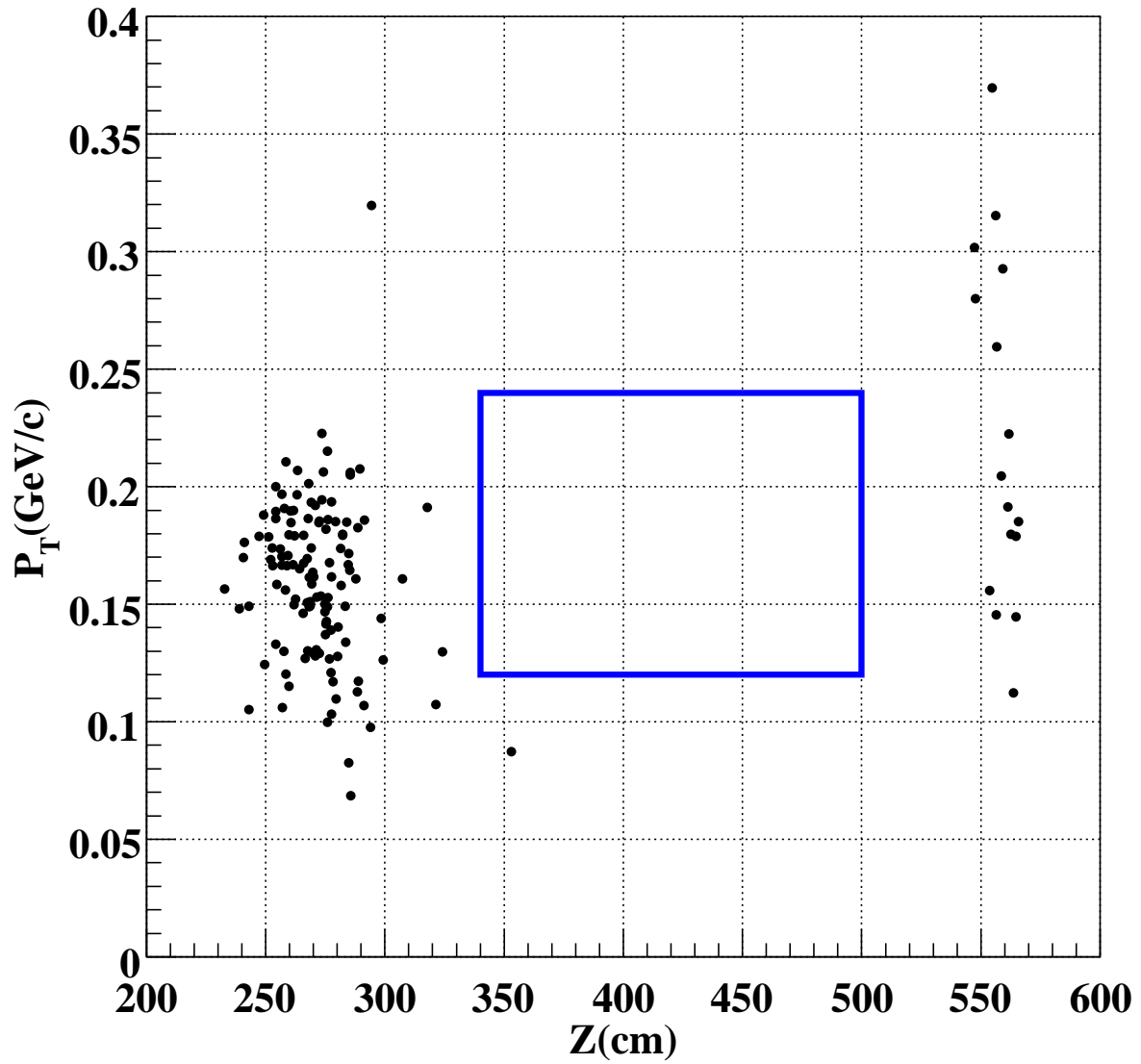
Figure 10.1: Scatter plot of Z_{vtx} vs. P_T with all the event selection cuts imposed.

10.3 Discussions

Null events observation at the SES of $(2.91 \pm 0.31) \times 10^{-8}$ was consistent with the expectation in the Standard Model. The SES was still 20 times higher than the Grossman-Nir limit, which is the model-independent theoretical upper bound as described in Section 1.5. Thus, this result did not give a theoretical impact on physics.

However, there is room for improving the measurement in further analysis and in future experiments. We discuss how the experiments employing our experimental concepts would improve the sensitivity.

10.3.1 Background Sources

The largest background source in the E391a Run-II was the interactions of the halo neutrons with detector materials. There are two ways to improve this. One is to reduce the neutron halo even further, improving the shape of the collimator system. The other way, based on the E391a configuration, is to move the last collar counter prior to the decay volume, CC02 in E391a, to the upstream. This will help recover the acceptance and reduce the background by shifting the Z-vertex away from the signal region, making event separation easier.

10.3.2 Calorimeter

The dimension of the CsI crystals ($7 \times 7 \times 30$ cm^3) caused several limitations to E391a. First, the longitudinal length of 30 cm was found to be too short to fully contain the electromagnetic shower; we observed the long tail of the CC02 events in the reconstructed Z_vtx distribution due to the shower leakage, as described in Section 9.2. In addition, even with the radiation length of $16X_0$, the photon detection inefficiency due to the punch-through effect occurred and it caused the background event in the simulation, as described in Section 9.1.

Second, since the Moliére radius in CsI is about 3.5 cm, the large transverse size of the crystals made "single-crystal hits", unable to be identified as a photon cluster. The single-crystal hits caused large acceptance loss in the CsI Veto.

We are going to use more "KTeV" CsI crystals to construct the calorimeter in the future experiment at J-PARC, mentioned later. The dimensions of the KTeV CsI are $5 \times 5 \times 50$ cm^3 and $2.5 \times 2.5 \times 50$ cm^3 [55]. We expect better Z-vertex resolution and photon discrimination with the KTeV CsI crystals.

10.3.3 Veto Inefficiency

We checked the total photon veto inefficiency with the low mass events in the 4 clusters sample, as described in Section 9.1. However, if we were able to know the photon veto inefficiency for each detector by the measurement, we could calculate the background level more reliably from such as $K_L^0 \to \pi^0 \pi^0$ with the MC.

To achieve this purpose, we attempted to use $K_L^0 \to \pi^0 \pi^0 \pi^0$ with exactly five photons hitting the CsI calorimeter in E391a. We then calculated the expected energy and direction of the remaining photon using the kinematic constraints from the $K_L^0 \to \pi^0 \pi^0 \pi^0$ decay. Finally, we obtained an upper limit of the inefficiency in the Main Barrel at 7.66×10^{-4} at the 90% C.L. [56]. We expect to obtain a value of necessity with more statistics improving the method.

10.3.4 Angle Measurement

We developed the method to measure the polar angle of the incident photons to the CsI calorimeter with the energy spread, as explained in Section 7.3.3. We had no kinematic constraints in reconstruction of the π^0's other than this angle. If we had better resolution for the incident angle, this measurement would be a powerful tool to reject the backgrounds. The finer segmented calorimeter would help us to improve the resolution.

10.3.5 Future Experiment

As described in Section 1.7, the E391a experiment was carried out as a "pilot" experiment of the future experiment. The new experiment is now prepared, using the 30 GeV high intensity proton synchrotron, J-PARC ("Japan Proton Accelerator Research Complex"), being constructed at Tokai. The intensity is expected to two order of magnitude higher than that of KEK-PS. The measurement of $K_L^0 \to \pi^0 \nu \bar{\nu}$, named "K^{O}TO", was proposed in 2006, and is approved as E14. In the first step of this experiment, we will produce K_L^0's with the "common" target shared with other experiments, and the E391a detector will be used for the most parts [55]. As described above, the CsI calorimeter will be replaced by the KTeV crystals, and CC02 will be also replaced with a full-active counter and located more upstream. With other possible modifications based on the studies in E391a, we first aim to reach the sensitivity of the SM prediction.

In the next step, we plan to build a dedicated beam line to the K^{O}TO experiment and a new detector system. Our final goal is to observe 100 SM events for $K_L^0 \to \pi^0 \nu \bar{\nu}$: a sensitivity of $O(10^{-13})$. This gives a 10% measurement of the branching fraction and has a power to explore the physics beyond the Standard Model.

Chapter 11

Conclusion

We searched for the rare decay $K_L^0 \to \pi^0 \nu \bar{\nu}$ with the full data taken in E391a Run-II. With the single event sensitivity of $(2.91 \pm 0.31) \times 10^{-8}$ and the background estimation of 0.42 ± 0.14, we observed no signal events. The upper limit on the branching ratio was set to be

$$Br(K_L^0 \to \pi^0 \nu \bar{\nu}) < 6.7 \times 10^{-8} \, ,$$

at the 90% C.L.. This represents the improvement by a factor of 3.1 over the past limit with the E391a Run-I 10% data, and a factor of 8.8 improvement over the limit by the KTeV experiment.

We required two photons from the $\pi^0 \to \gamma\gamma$ decay and no other particles detected in the final state in our search for the $K_L^0 \to \pi^0 \nu \bar{\nu}$ decay. We constructed the narrow beam line and the detector with the hermetic photon-detection system for the experiment to achieve the experimental concept.

We found that the particles produced by the halo neutrons in the beam line were the dominant background source in this experiment. We understood the mechanism of the backgrounds, and developed the methods to suppress them.

It turned out that the shortage in the longitudinal length of the CsI calorimeter was a problem for the π^0 events produced by the halo neutrons in the upstream. The leakage of the electromagnetic shower from the CsI calorimeter caused the contamination of the upstream events shifted to the signal region. We expect these background studies in the E391a experiment will be great help in the future experiments for $K_L^0 \to \pi^0 \nu \bar{\nu}$.

In conclusion, this analysis achieved the "first" dedicated search for $K_L^0 \to \pi^0 \nu \bar{\nu}$ and provided the essential points in our experimental methods.

Appendix A

K_L^0 Reconstruction

In this appendix, we describe the method of K_L^0 full reconstruction with six and four photon clusters in the CsI calorimeter. We summarize the selection criteria in the K_L^0 reconstruction for $K_L^0 \to \pi^0 \pi^0 \pi^0$, $K_L^0 \to \pi^0 \pi^0$, and $K_L^0 \to \gamma\gamma$ decays.

A.1 K_L^0 Reconstruction with Multi-π^0 Events

When we reconstructed K_L^0 in six(four) photon cluster samples, there were 15(3) possible photon pairings to form three(two) π^0's. For each photon pair (i), we calculated the π^0 decay vertex Z_i, and calculated the weighted mean value of Z_i's:

$$Z(K_L^0) = \frac{\sum_{i=1}^n Z_i/\sigma_i^2}{\sum_{i=1}^n 1/\sigma_i^2} \; , \tag{A.1}$$

where σ_i is the error in the Z_i reconstruction, calculated from the resolutions in the measurement as a function of two photons energies and positions.

In order to evaluate the K_L^0 reconstruction, we calculated the quantity called "pairing χ_Z^2":

$$\chi_Z^2 = \sum_{i=1}^n \frac{(Z_i - Z(K_L^0))^2}{\sigma_i^2} \; . \tag{A.2}$$

For each event, we selected the photon pairing with the smallest χ_Z^2. We then calculate the following quantities.

- K_L^0 energy

$$E(K_L^0) \;=\; \sum_{i=1}^6 E_i(\gamma) \; , \tag{A.3}$$

where $E_i(\gamma)$ is the energy of the i-th photon.

- K_L^0 decay vertex

$$
\begin{pmatrix} X \\ \\ Y \\ \\ Z \end{pmatrix} = \begin{pmatrix} s \times \sum_{i=1}^{6} E_i(\gamma) X_i(\gamma) / E(K_L^0) \\ \\ s \times \sum_{i=1}^{6} E_i(\gamma) Y_i(\gamma) / E(K_L^0) \\ \\ Z(K_L^0) \end{pmatrix} , \qquad (A.4)
$$

  where

$$
s = \frac{Z(K_L^0) - Z_{target}}{Z_{CsI} - Z_{target}} , \qquad (A.5)
$$

  $(X_i(\gamma), Y_i(\gamma))$ is the hit position of the i-th photon on the CsI calorimeter, Z_{target} is the position of the production target (-1180 cm) and Z_{CsI} is the position of the CsI calorimeter (614.8 cm).

- Invariant mass

$$
M(6\gamma) = \sqrt{[E(K_L^0)]^2 - \left[\sum_{i=1}^{6} P_{Xi}(\gamma) \right]^2 - \left[\sum_{i=1}^{6} P_{Yi}(\gamma) \right]^2 - \left[\sum_{i=1}^{6} P_{Zi}(\gamma) \right]^2} , \qquad (A.6)
$$

  where $P_{Xi}(\gamma)$, $P_{Yi}(\gamma)$ and $P_{Zi}(\gamma)$ are the x, y and z components of the momentum vector of the i-th photon calculated with the K_L^0 vertex and the photon's energy and hit position on the CsI calorimeter.

In order to remove mis-reconstructed K_L^0's, we required the χ_Z^2 of the K_L^0 candidate event to be less than 3.0 (best χ_Z^2 cut). As shown in the left plot of Figure 8.3, the distribution of the χ_Z^2 of the K_L^0 candidate events in six-photon sample in data was consistent with that in MC.

Moreover, we required the additional condition in order to make sure that we have selected the correct photon pairing. We took the difference between the best χ_Z^2 and the next smallest χ_Z^2 (second best χ_Z^2 pairing), shown in the right plot of Figure 8.3, and required it to be more than 4.0.

A.2 Kinematic Conditions in the K_L^0 Reconstruction

We implied several mode-dependent conditions for the kinematic cuts in the K_L^0 reconstruction for the $K_L^0 \rightarrow \pi^0 \pi^0 \pi^0$, $K_L^0 \rightarrow \pi^0 \pi^0$, $K_L^0 \rightarrow \gamma\gamma$ samples.

We first imposed the photon energy cut and the hit position cuts. For the $K_L^0 \rightarrow \gamma\gamma$ selection, we imposed the energy ratio cut, and the RMS cut for each photon and the sum of the RMS value of the two photons.

Concerning the cut conditions for the photon distance cut, we required the minimum value for the shortest distance.

We had developed Neural Network (NN) functions for the suppression of the "fused " photon clusters and for the measurement of the polar angle of the incident photons. For robustness and simpleness, we replaced them by the photon RMS cut and the $\Delta\theta\chi^2$ cut in the $K_L^0 \rightarrow \pi^0 \nu\bar{\nu}$ analysis. However,

with historical reasons, they remained in the K_L^0 selection. In the function for the fused cluster, called "fusion NN", the output value close to 1(0) meant the single-photon-like(fused-line) cluster. For the $K_L^0 \to \gamma\gamma$ events selection, we used the NN function to measure the photon incident angle with the energy distribution in the photon cluster, requiring the difference between the reconstructed angle and the output from the NN function to be more than $-20°$.

In addition to the cuts with χ_Z^2, we imposed cuts for the relation among the π^0's. After reconstructing K_L^0, we took the difference between Z_i and $Z(K_L^0)$, and required it to be less than 10(5) cm for the $K_L^0 \to \pi^0\pi^0\pi^0$ ($K_L^0 \to \pi^0\pi^0$) selection. We also re-calculated the invariant mass using the $Z(K_L^0)$ for each π^0 and required its deviation from M_{π^0} (135 MeV/c^2, quoted from PDG2006 [8]) to be less than 5.125(5) MeV/c^2 for $K_L^0 \to \pi^0\pi^0\pi^0$ ($K_L^0 \to \pi^0\pi^0$).

Finally, we required the P_T^2 and the radial position R^2 for the reconstructed K_L^0 to be consistent with the beam divergence. The conditions for the kinematic cuts in the K_L^0 reconstruction are summarized in Table A.1, A.2, and A.3 for $K_L^0 \to \pi^0\pi^0\pi^0$, $K_L^0 \to \pi^0\pi^0$, and $K_L^0 \to \gamma\gamma$, respectively.

Table A.1: Kinematic cuts for the $K_L^0 \to \pi^0\pi^0\pi^0$ reconstruction

Cut		Min.	Max.
Photon Quality Cuts	Energy	150 MeV	
	Hit position(square)	17.5 cm	
	Hit position(radial)		88 cm
	Fusion NN	0.5	
Two Photon Cuts	Distance	17.5 cm	
K_L^0 Cuts	Best χ_Z^2		3.0
	2nd Best $-$ Best χ_Z^2	4.0	
	$\pi^0 Z$ difference		10 cm
	π^0 mass difference		5.125 MeV/c^2
	R^2 at C6		4.5 cm^2
	$Z(K_L^0)$	340 cm	500 cm
	$P_T(K_L^0)^2$		1.25×10^{-4} (GeV/c)^2

Table A.2: Kinematic cuts for the $K_L^0 \to \pi^0\pi^0$ reconstruction

Cut		Min.	Max.
Photon Quality Cuts	Energy	150 MeV	
	Hit position(square)	17.5 cm	
	Hit position(radial)		88 cm
	Fusion NN	0.7	
Two Photon Cuts	Distance	15.0 cm	
K_L^0 Cuts	Best χ_Z^2		3.0
	2nd Best $-$ Best χ_Z^2	4.0	
	$\pi^0 Z$ difference		5 cm
	π^0 mass difference		5.0 MeV/c^2
	R^2 at C6		4.0 cm^2
	$Z(K_L^0)$	340 cm	500 cm
	$P_T^2(K_L^0)$		1.25×10^{-4} (GeV/c)^2

Table A.3: Kinematic cuts for the $K_L^0 \to \gamma\gamma$ reconstruction.

Cut		Min.	Max.
Photon Quality Cuts	Higher Energy	250 MeV	
	Lower Energy	150 MeV	
	Energy Ratio	0.88	
	RMS each		5.2
	RMS sum		9.5
	Hit position(square)	15 cm	
	Hit position(radial)		88 cm
	Fusion NN	0.7	
Two Photon Cuts	Distance	15.0 cm	
K_L^0 Cuts	$\Delta\theta$ NN	-20°	
	Acoplanarity Angle		10°
	$Z(K_L^0)$	340 cm	500 cm
	$P_T^2(K_L^0)$		9×10^{-4} (GeV/c)^2

Appendix B

CsI Calibration

The energy resolution of the CsI calorimeter was crucial in the E391a experiment. In this appendix, we describe the methods to calibrate the energy in the CsI crystals by cosmic-rays and the $K_L^0 \to \pi^0\pi^0\pi^0$ sample.

B.1 Cosmic Ray Calibration

We employed the cosmic-ray trigger requiring a pair of coincident hits of the Main Barrel in the opposite sides in the radial direction. The cosmic-ray data was taken simultaneously during the physics run. In the sample, we selected for the events which contained a muon track that passed through the CsI calorimeter. The cosmic-ray trajectory was reconstructed by fitting the CsI hit pattern by a straight line. We required at least 10 hits in the CsI crystals along the track. Figure B.1 shows a typical event display [42].

The path length across a single crystal was calculated by using the trajectory. The charge output of the crystal was divided by this path length. Figure B.2 shows the distributions of raw charge outputs, track lengths, and normalized charge outputs for three types of crystals. We obtained clear peaks after the normalization. The peak value was determied by fitting the spectrum to a Landau function. The gain factor to convert the charge to the energy deposition was calculated by assuming that the energy deposited by a cosmic-ray muon per unit length in CsI is 5.63 MeV/cm, according to the PDG value. Figure B.3 demonstrates the stability of the gain factor in a certain run period.

B.2 $K_L^0 \to \pi^0\pi^0\pi^0$ Calibration

After the cosmic-ray calibration, we applied a correction to the calibration factors of the CsI calorimeter using the $K_L^0 \to \pi^0\pi^0\pi^0$ decays [57].

B.2.1 Algorithm

First, a $K_L^0 \to \pi^0\pi^0\pi^0$ candidate event was reconstructed with 6 photon clusters. The pairing of the photons was solved by the standard best-χ_Z^2 method, as described in Appendix A. The kinematically
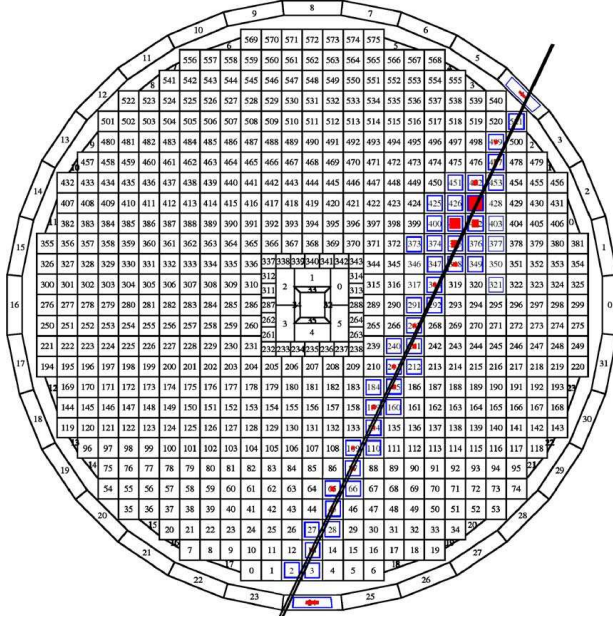
Figure B.1: Cosmic-ray track in the CsI calorimeter. The number indicate the crystal ID. Red boxes show the size of the energy deposition and blue boxes show the timing information.

constrained fits were applied for the K_L^0 candidates. A least square method with Lagrange multipliers was introduced for the root finding. The algorithm was as follows.

Consider an array of parameters including all the measured variables, such as position (x, y) and energy (E) of each photon,

$$\alpha = (x_1, y_1, E_1; x_2, y_2, E_2; ...; x_6, y_6, E_6) \tag{B.1}$$

where α was a vector of 18 variables. The associated 18×18 error matrix was represented by

$$V_\alpha = \begin{pmatrix} \sigma_{x_1}^2 & 0 & 0 & \cdots \\ 0 & \sigma_{y_1}^2 & 0 & \\ 0 & 0 & \sigma_{E_1}^2 & \\ \vdots & & & \ddots \end{pmatrix}. \tag{B.2}$$

The parameters for K_L^0 vertex position were unknown and should be determined by the constraints. Thus, an additional vector with 3 components was prepared

$$v = (v_x, v_y, v_z). \tag{B.3}$$

The following kinematic constraints were introduced in the fit.

- π^0 mass constraints:

$$(E_1 + E_2)^2 - (\vec{P}_1 + \vec{P}_2)^2 = M_{\pi^0}^2 \tag{B.4}$$

$$(E_3 + E_4)^2 - (\vec{P}_3 + \vec{P}_4)^2 = M_{\pi^0}^2 \tag{B.5}$$

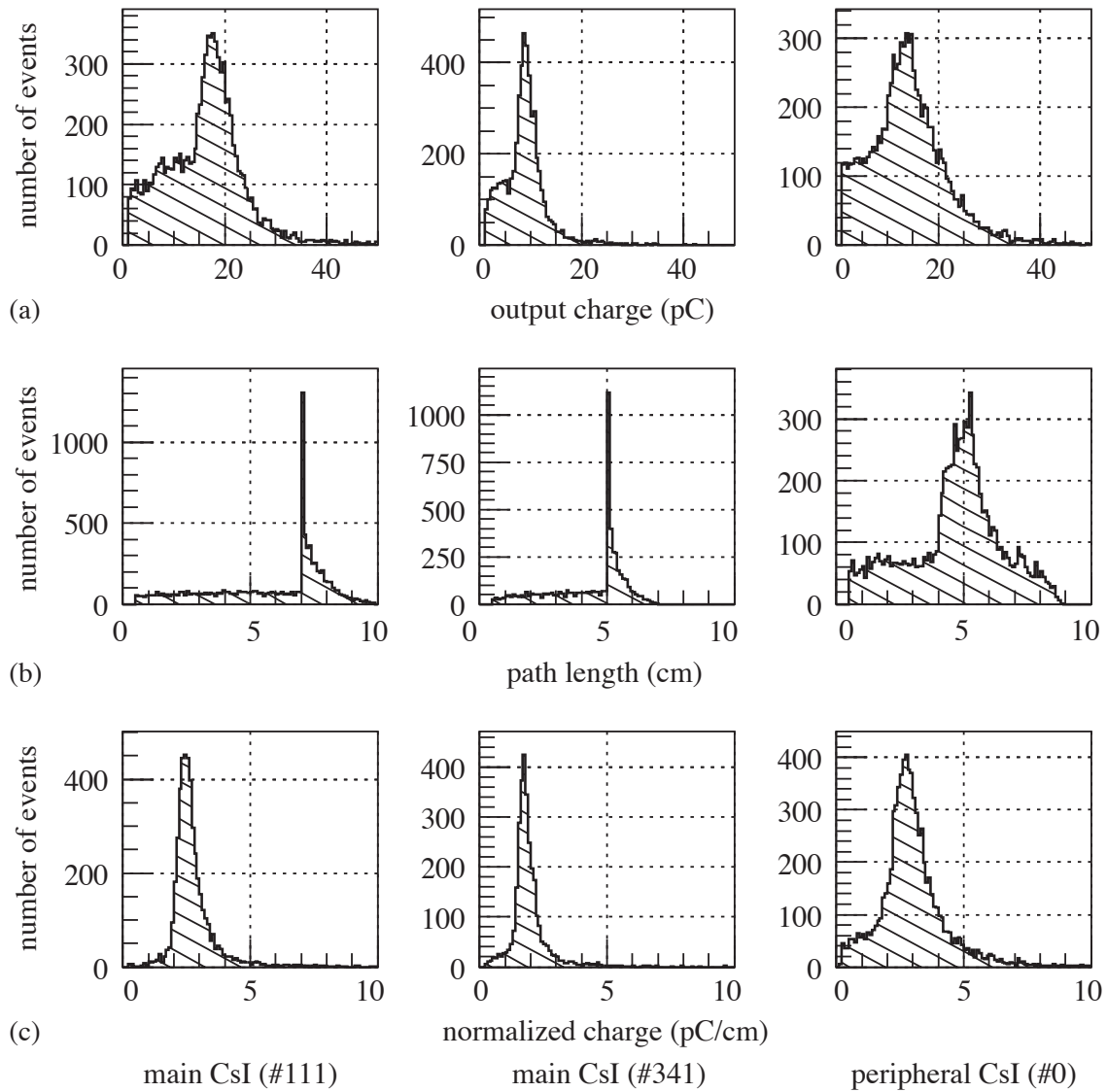$$(E_5 + E_6)^2 - (\vec{P}_5 + \vec{P}_6)^2 = M_{\pi^0}^2 \tag{B.6}$$

Figure B.2: Charge output from each CsI crystal and its correction with the cosmic-ray data (ADC value). The histograms in rows indicate raw charges (top), path-length (middle) and normalized charges (bottom). The column shows a type of the crystal, Normal CsI (left), KTeV CsI (center), and Edge CsI (right).
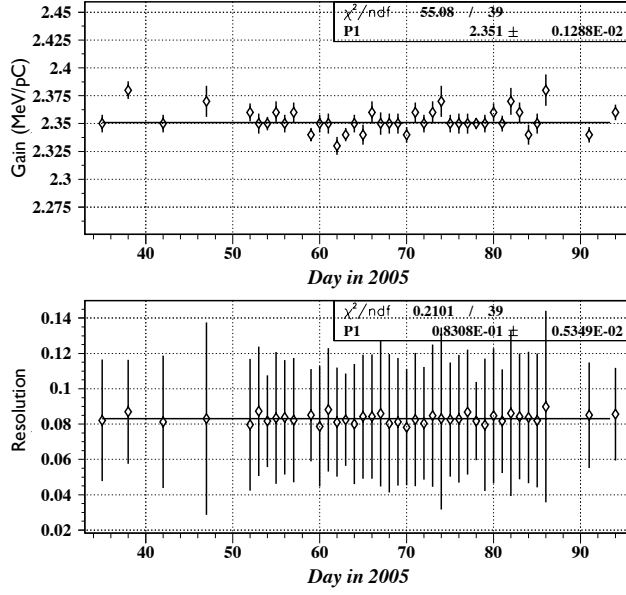
Figure B.3: CsI gain stability as monitored with the cosmic-ray data. Upper and lower figures show the gain factor and the resolution of the MIP peak, respectively.

where $\vec{P}_i$ defined as a vector

$$\vec{P}_i = \frac{E_i}{\sqrt{(x_i - v_x)^2 + (y_i - v_y)^2 + (Z_{CsI} - v_z)^2}}(x_i - v_x, y_i - v_y, Z_{CsI} - v_z) \qquad \text{(B.7)}$$

- K_L^0 mass constraint:

$$\left(\sum E_i\right)^2 - \left(\sum P_i\right)^2 = M_{K_L^0}^2 \qquad \text{(B.8)}$$

- the "center of gravity" requirement:

$$\sum x_i \cdot E_i = v_x \cdot \sum E_i \qquad \text{(B.9)}$$

$$\sum y_i \cdot E_i = v_y \cdot \sum E_i \qquad \text{(B.10)}$$

These requirements formed 6 constrained equations and were labeled as

$$H(\alpha, v) = (H_1, H_2, H_3, ..., H_6) . \qquad \text{(B.11)}$$

The fit consisted of 6 constraints, 3 unknown variables, and 3 degrees of freedom. By expanding H around α_A and v_A, were obtained an equation:

$$H(\alpha_A, v_A) + \left[\frac{\partial H}{\partial \alpha}\right]_{\alpha_A}(\alpha - \alpha_A) + \left[\frac{\partial H}{\partial v}\right]_{v_A}(v - v_A) = 0 , \qquad \text{(B.12)}$$

or in the matrix representation

$$d + D(\alpha - \alpha_A) + E(v - v_A) = 0 , \qquad \text{(B.13)}$$

where d was a vector that contains the values of H; D and E were given by $\left[\frac{\partial H}{\partial \alpha}\right]_{\alpha_A}$ and $\left[\frac{\partial H}{\partial v}\right]_{v_A}$, respectively. The method of Lagrange multipliers was formulated as:

$$V_D = (DV_{\alpha 0}D^T)^{-1} \tag{B.14}$$

$$V_E = (E^T V_D E)^{-1} \tag{B.15}$$

$$\lambda_0 = V_D[D(\alpha_0 - \alpha_A) + d] \tag{B.16}$$

$$\chi^2 = \lambda_0^T[D(\alpha_0 - \alpha_A) + E(v_0 - v_A) + d] \tag{B.17}$$

$$\lambda = \lambda_0 - V_D E V_E E^T \lambda_0 \tag{B.18}$$

$$v = v_A - V_E E^T \lambda_0 \tag{B.19}$$

$$\alpha = \alpha_A - V_{\alpha 0} D^T \lambda \tag{B.20}$$

where $V_{\alpha 0}$ is the measured error matrix, and α_0 is the vector containing the initial measured values. The fitting results were given by α and v. The updated error matrix after the fitting could be extracted by

$$V_\alpha = V_{\alpha 0} - V_{\alpha 0} D^T (V_D - V_D E V_E E^T V_D) D V_{\alpha 0} \,. \tag{B.21}$$

In general, several iterations were needed to converge α and v. In each iteration, the best χ^2 result of v was determined first and then the root of α will be obtained later. The operations was terminated when the best χ^2 was obtained. Figure B.4 and B.5 show the invariant mass distributions of K_L^0 and π^0 before and after the constrained fits, respectively. The distribution of χ^2 is shown in Figure B.6.
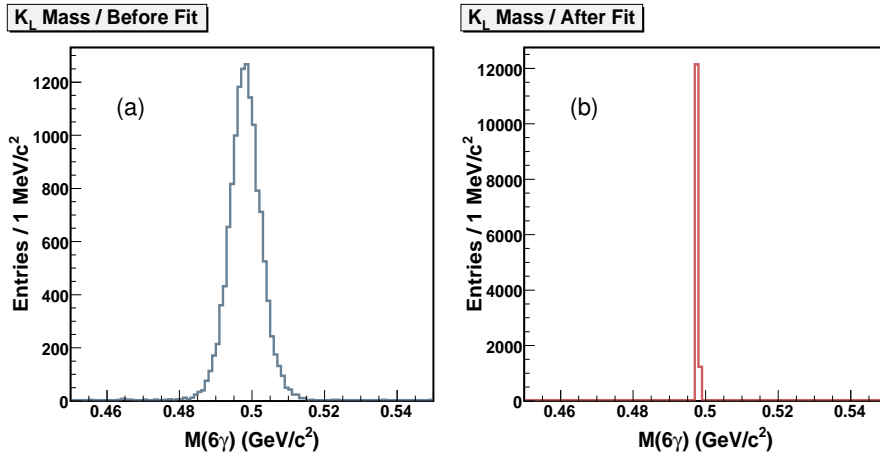

Figure B.4: Invariant mass distributions of $K_L^0 \to \pi^0\pi^0\pi^0$ candidates in MC before (a) and after (b) the constrained fit.
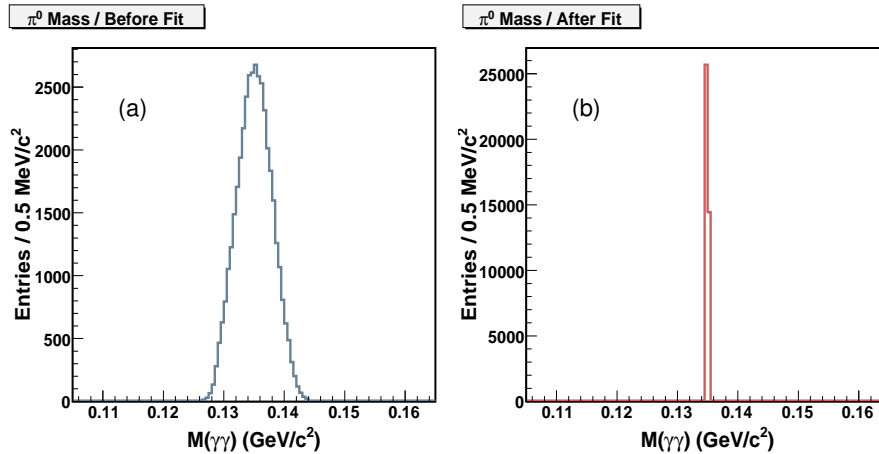
Figure B.5: Invariant mass distributions of $\pi^0 \to \gamma\gamma$ candidates in MC for before (a) and after (b) the constrained fit.
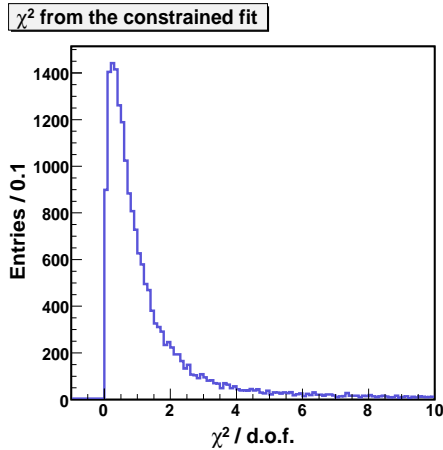

Figure B.6: Distribution for χ^2 per degree of freedom for the MC events with the kinematically constrained fit.

B.2.2 Determination of the Calibration Factors

To obtain the calibration factor of each crystal, we intended to treat the energy of one crystal as variable. The number of measured parameters became 17 instead of 18, while the number of unknown variables was increased to 4. Hence the number of degrees of freedom was reduced to 2. Using the same kinematic constraints and iteration method for each daughter photon, the calibration factor of each crystal was determined.

This correction was applied only on the crystal with the largest energy deposition in each cluster. In order not to diverge the iteration, we did not use the photon cluster in which a crystal with the second largest energy accounted more than 20% of the cluster energy. In order to remove fail-fitted events, the resultant χ^2 per degree of freedom of the kinematic fit was required to be less than 5. The resultant invariant masses of K_L^0 and π^0 should be within ± 5 MeV/c^2 and ± 3 MeV/c^2 of their true values, respectively. The updated Z vertex should agree with the original Z position before the fitting within ± 20 cm. As a matter of fact, these requirements were so loose that they only discarded events with

unphysical solutions.

The calibration factors were determined for each CsI crystal, periodically during the data taking, and, finally the averaged factors were determined. The calibration process required several iterations to reach stable values. For both data and the MC studies, the implementation of the $K_L^0 \to \pi^0\pi^0\pi^0$ calibration needed at least 5 iterations to reach converged results.

B.2.3   Performance of the $K_L^0 \to \pi^0\pi^0\pi^0$ Calibration

The performance of the calibration was checked by the data and $K_L^0 \to \pi^0\pi^0\pi^0$ MC. In order to perform an independent check, only the events with even event-number were included in the calibration, while the events with odd event-number were reserved for the performance checks. The observed number of K_L^0 candidates as a function of number of iterations is shown in Figure B.7. As the iteration was proceeded, the number of observed events increased by 4.9% in real data and slightly decreased (-0.7%) in MC sample. The mass distributions before and after the calibration for the K_L^0 candidates from real data are shown in Figure B.8. The mean and width of the invariant mass for the K_L^0 candidates as functions of number of iterations are shown in Figure B.9, and those of the daughter π^0 candidates are shown in Figure B.10. The width of K_L^0 and π^0 candidates were improved by 4.9% and 3.4%, respectively. However, the intrinsic mean shifts of 0.4 MeV and 0.1 MeV was observed for K_L^0 and π^0 candidates, respectively, even after the calibration processes. The same phenomena were also found in MC events. This was due to the correlation between the reconstructed Z-vertex position and its associated error. Thus, the averaged (or error weighted) vertex was slightly closer to positive Z side, since it had a smaller error. This reflected as a small shift in the invariant mass since the total energy was fixed. We understood the behavior was inevitable and decided not make any correction for it.
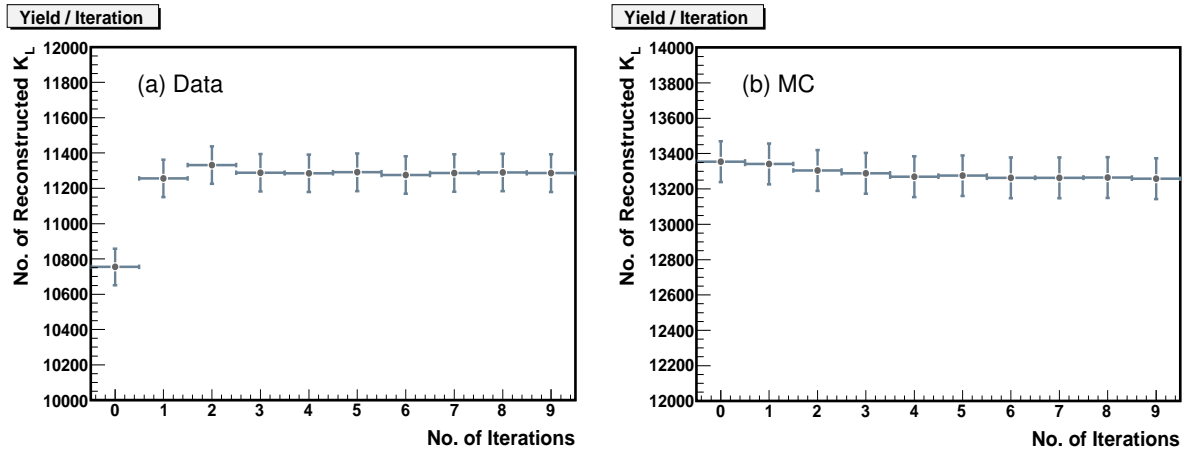

Figure B.7: Observed number of K_L^0 candidates as a function of the number of iterations from (a) the data and (b) MC.
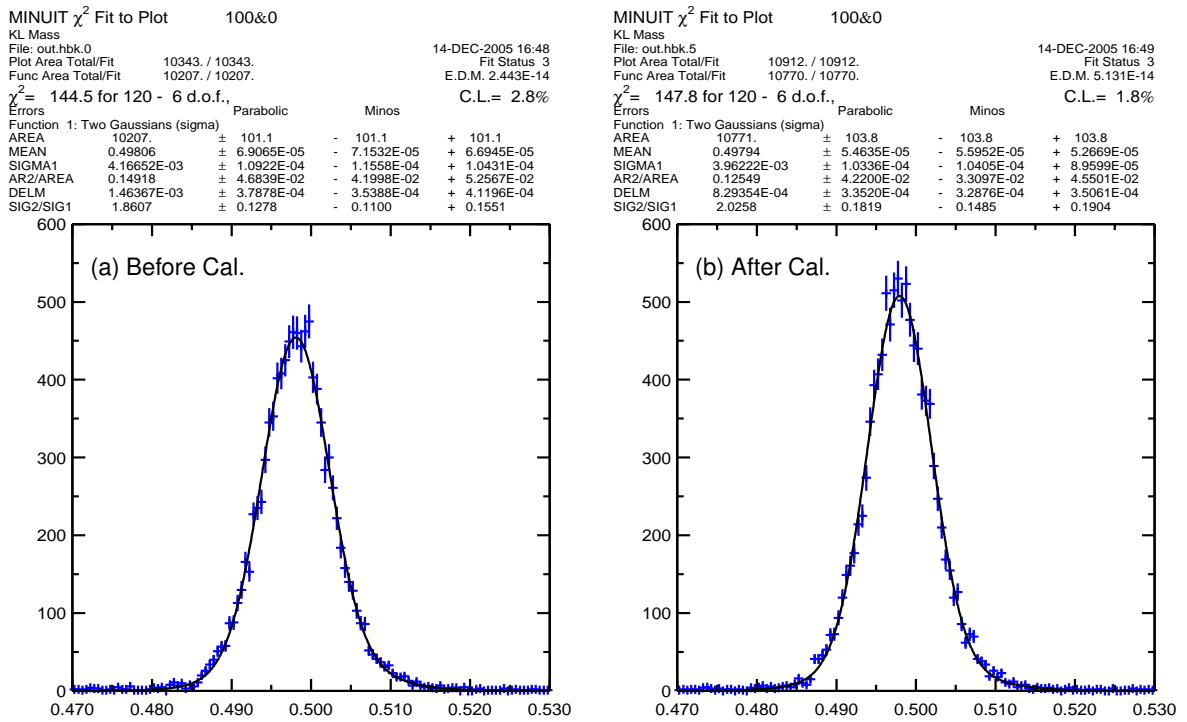
Figure B.8: Invariant mass distributions of the K_L^0 candidates from real data before (a) and after (b) the 5 iterations of the calibration.
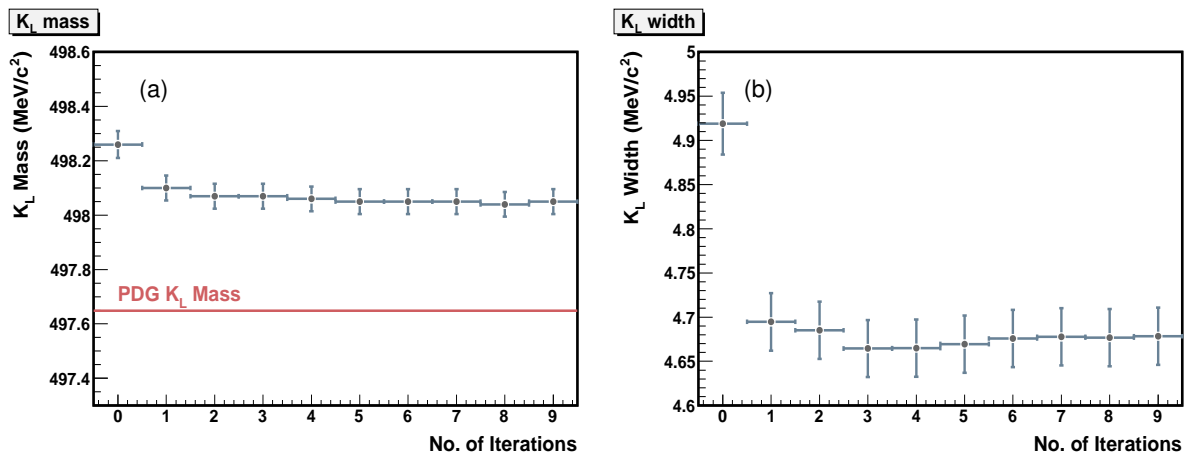

Figure B.9: (a) Mean and (b) of the invariant masses of the six cluster sample versus the iteration steps.
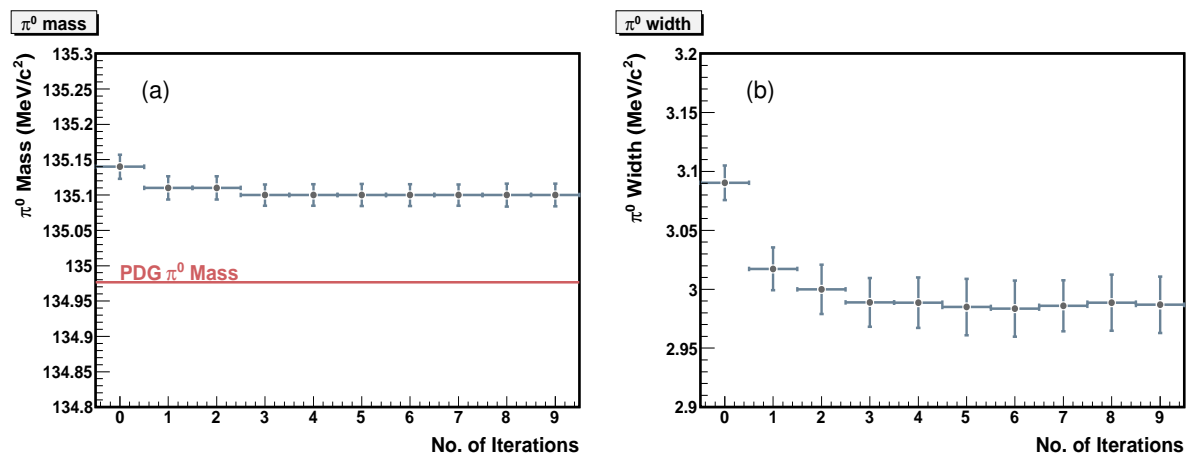
Figure B.10: (a) Mean and (b) width of the invariant masses of the two cluster events versus the iteration steps.

Appendix C

Statistical methods on the Upper Limit

We set the upper limit on $Br(K_L^0 \to \pi^0 \nu \bar{\nu})$ based on Poisson statistics. In this appendix, we briefly discuss other methods on setting our upper limit.

C.1   Incorporating the Systematic Error

The number of observed events, n, distributes following Poisson statistics:

$$P(n|\mu) = \frac{\mu^n \exp(-\mu)}{n!} \, , \tag{C.1}$$

where μ is the expected mean of the number of signal events, $Br(K_L^0 \to \pi^0 \nu \bar{\nu})/\text{SES}$.

Since we observed no events, we calculate the probability of μ to be less than μ_0 as:

$$Q(\mu < \mu_0) = \int_0^{\mu_0} P(0|\mu)d\mu$$

$$= 1 - \exp(-\mu_0) \, . \tag{C.2}$$

Here, μ_0 is called "interval" for the upper limit.

In setting the upper limit, $Q(\mu < \mu_0)$ is called "Confidence Level"(C.L.). μ_0 is calculated by the C.L. from Equation C.2:

$$\mu_0 = -\ln(1 - \text{C.L.}) \, . \tag{C.3}$$

When we set the C.L. of 90%, μ_0 is calculated as:

$$\mu_0 = -\ln(1 - 0.9) \approx 2.30 \, . \tag{C.4}$$

Thus, we set the upper limit on $Br(K_L^0 \to \pi^0 \nu \bar{\nu})$ with the SES of 2.91×10^{-8},

$$Br(K_L^0 \to \pi^0 \nu \bar{\nu}) < 2.30 \times \text{SES} = 6.69 \times 10^{-8} \, , \tag{C.5}$$

If we took the uncertainty on the SES, σ_{SES}, into account, the confidence interval at the 90% C.L. in the null event observation would be altered as:

$$\mu_0' = 2.30(1 + 2.30 \, \sigma_{\text{SES}}^2/2) \, , \tag{C.6}$$

according to the statistical treatment in the reference [58].

Thus, the upper limit changed to be:

$$Br(K_L^0 \to \pi^0 \nu \bar{\nu}) < \mu_0' \times \text{SES}$$

$$= 6.78 \times 10^{-8} ,$$

(C.7)

though the effect was only 1% level.

C.2 Feldman-Cousins Method

We estimated the total background events of 0.42 ± 0.14. If we took the background contribution into account, we could set another upper limit.

With the number of expected background events b, the Poisson distribution is modified as:

$$P(n|\mu, b) = \frac{(\mu + b)^n \exp[-(\mu + b)]}{n!} .$$

(C.8)

The Feldman-Cousins prescription [59] provides an unified confidence intervals. We performed the Feldman-Cousins (FC) method with the same parameterization as in the reference [59].

Since we observed no events, the 90 % confidence level upper limit was calculated to be 2.02 by the FC method, instead of 2.30 by the simple Poisson statistics. Thus, we could improve the upper limit as:

$$Br(K_L^0 \to \pi^0 \nu \bar{\nu}) < 2.02 \times \text{SES}$$

$$= 5.88 \times 10^{-8} \quad (90\%\text{C.L.}).$$

(C.9)

which corresponded to 12% better limit.

References

[1] T. D. Lee and C.-N. Yang, Phys. Rev. **104**, 254 (1956).

[2] C. S. Wu, E. Ambler, R. W. Hayward, D. D. Hoppes, and R. P. Hudson, Phys. Rev. **105**, 1413 (1957).

[3] R. L. Garwin, L. M. Lederman, and M. Weinrich, Phys. Rev. **105**, 1415 (1957).

[4] J. I. Friedman and V. L. Telegdi, Phys. Rev. **105**, 1681 (1957).

[5] J. H. Christenson, J. W. Cronin, V. L. Fitch, and R. Turlay, Phys. Rev. Lett. **13**, 138 (1964).

[6] M. Kobayashi and T. Maskawa, Prog. Theor. Phys. **49**, 652 (1973).

[7] A. D. Sakharov, Pisma Zh. Eksp. Teor. Fiz. **5**, 32 (1967).

[8] Particle Data Group, W. M. Yao *et al.*, J. Phys. **G33**, 1 (2006).

[9] T. T. Wu and C.-N. Yang, Phys. Rev. Lett. **13**, 380 (1964).

[10] L. Bergstrom, E. Masso, and P. Singer, Phys. Lett. **B131**, 229 (1983).

[11] N. Cabibbo, Phys. Rev. Lett. **10**, 531 (1963).

[12] L. Wolfenstein, Phys. Rev. Lett. **51**, 1945 (1983).

[13] C. Jarlskog, Phys. Rev. Lett. **55**, 1039 (1985).

[14] B. Winstein and L. Wolfenstein, Rev. Mod. Phys. **65**, 1113 (1993).

[15] A. J. Buras, (1999), hep-ph/9905437.

[16] CKMfitter Group, J. Charles *et al.*, Eur. Phys. J. **C41**, 1 (2005), hep-ph/0406184.

[17] A. J. Buras, F. Schwab, and S. Uhlig, (2004), hep-ph/0405132.

[18] T. Inami and C. S. Lim, Prog. Theor. Phys. **65**, 297 (1981).

[19] F. Mescia and C. Smith, Phys. Rev. **D76**, 034017 (2007), 0705.2025.

[20] Y. Grossman and Y. Nir, Phys. Lett. **B398**, 163 (1997), hep-ph/9701313.

[21] W. J. Marciano and Z. Parsa, Phys. Rev. **D53**, 1 (1996).

[22] E949, V. V. Anisimovsky *et al.*, Phys. Rev. Lett. **93**, 031801 (2004), hep-ex/0403036.

[23] A. J. Buras, R. Fleischer, S. Recksiegel, and F. Schwab, Nucl. Phys. **B697**, 133 (2004), hep-ph/0402112.

[24] A. J. Buras, R. Fleischer, S. Recksiegel, and F. Schwab, Phys. Rev. Lett. **92**, 101804 (2004), hep-ph/0312259.

[25] M. Artuso *et al.*, (2008), 0801.1833.

[26] U. Haisch, ECONF **C0508141**, ALCPG1919 (2005), hep-ph/0512007.

[27] A. J. Buras, T. Ewerth, S. Jager, and J. Rosiek, Nucl. Phys. **B714**, 103 (2005), hep-ph/0408142.

[28] C. Bobeth *et al.*, Nucl. Phys. **B726**, 252 (2005), hep-ph/0505110.

[29] A. J. Buras, M. Spranger, and A. Weiler, Nucl. Phys. **B660**, 225 (2003), hep-ph/0212143.

[30] S. R. Choudhury, N. Gaur, G. C. Joshi, and B. H. J. McKellar, (2004), hep-ph/0408125.

[31] A. J. Buras, A. Poschenrieder, and S. Uhlig, (2005), hep-ph/0501230.

[32] L. S. Littenberg, Phys. Rev. **D39**, 3322 (1989).

[33] KTeV, J. Adams *et al.*, Phys. Lett. **B447**, 240 (1999), hep-ex/9806007.

[34] The E799-II/KTeV, A. Alavi-Harati *et al.*, Phys. Rev. **D61**, 072006 (2000), hep-ex/9907014.

[35] K. Sakashita, *Search for the decay $K_L^0 \to \pi^0 \nu \bar{\nu}$*, PhD thesis, Osaka University, 2006.

[36] E391a, J. K. Ahn *et al.*, Phys. Rev. **D74**, 051105 (2006), hep-ex/0607016.

[37] T. Inagaki *et al.*, Proposal of an Experiment at the KEK 12-GeV Proton Synchrotron: Measurement of the $K_L \to \pi^0 \nu \bar{\nu}$, KEK Internal, 1996.

[38] S. Ajimura *et al.*, Nucl. Instrum. Meth. **A552**, 263 (2005).

[39] K. Sakashita, , Master's thesis, Osaka University, 2002.

[40] H. Watanabe, *K_L^0 beam line for the study of the $K_L^0 \to \pi^0 \nu \bar{\nu}$ decay*, PhD thesis, Saga University, 2002.

[41] H. Watanabe *et al.*, Nucl. Instrum. Meth. **A545**, 542 (2005).

[42] M. Doroshenko *et al.*, Nucl. Instrum. Meth. **A545**, 278 (2005).

[43] M. Doroshenko, *A Measurement of the branching ratio of the KL -> pi0 nu nubar decay*, PhD thesis, SOKENDAI, 2004.

[44] T. Ikei, Charged Veto Detector for the KL -> pi0 nu nu-bar Experiment, Master's thesis, Osaka University, 2004.

[45] M. Itaya *et al.*, Nucl. Instrum. Meth. **A522**, 477 (2004).

[46] E391a, Y. Tajima *et al.*, Nucl. Instrum. Meth. **A592**, 261 (2008).

[47] C. P. L. L. W. W5013, GEANT - Detector Description and Simulation Tool, 1993.

[48] N. G. Deshpande and G. Eilam, Phys. Rev. Lett. **53**, 2289 (1984).

[49] GEANT4, S. Agostinelli *et al.*, Nucl. Instrum. Meth. **A506**, 250 (2003).

[50] H. S. Lee, *Search for the Rare Decay $K_L^0 \to \pi^0 \nu \bar{\nu}$*, PhD thesis, Pusan National University, 2007.

[51] J. R. Klein and A. Roodman, Ann. Rev. Nucl. Part. Sci. **55**, 141 (2005).

[52] K. F. J. Chen, Angle Measurement with Shower Shapes, Internal Memo, 2006.

[53] J. Ma, Performance of the Outer CV according to beam-line muons, Internal Memo, 2007.

[54] J. D. Nix, *First Search for $K_L \to \pi^0 \pi^0 \nu \bar{\nu}$ and $K_L \to \pi^0 \pi^0 P$*, PhD thesis, The University of Chicago, 2007.

[55] T. Yamanaka *et al.*, Proposal for $K_L^0 \to \pi^0 \nu \bar{\nu}$ at J-PARC, J-PARC Internal Document, 2006.

[56] G. N. Perdue, *Search for the Rare Decay $K_L^0 \to \pi^0 \nu \bar{\nu}$*, PhD thesis, The University of Chicago, 2008.

[57] K. F. J. Chen, CsI Calibration Using $K_L \to 3\pi^0$ Decays, Internal Technote, 2005.

[58] R. D. Cousins and V. L. Highland, Nucl. Instrum. Meth. **A320**, 331 (1992).

[59] G. J. Feldman and R. D. Cousins, Phys. Rev. **D57**, 3873 (1998), physics/9711021.